Energy-Level Alignment at Organic and Hybrid Organic-Inorganic Photovoltaic Interfaces

Keian Noori

St Anne's College
University of Oxford

Thesis submitted for the Degree of
Doctor of Philosophy in Materials

November 21, 2013

Abstract

Energy-Level Alignment at Organic and Hybrid Organic-Inorganic Photovoltaic Interfaces

Keian Noori, St Anne's College, University of Oxford

Thesis submitted for the Degree of Doctor of Philosophy in Materials, Trinity Term 2013

Organic and hybrid organic-inorganic photovoltaic (PV) devices have the potential to provide low-cost, large scale renewable energy. Despite the tremendous progress that has been made in this field, device efficiencies remain low. This low efficiency can be partly attributed to the low open-circuit voltages (V_{OC}) generated by organic and hybrid organic-inorganic PV devices. The V_{OC} is critically determined by the energy-level alignment at the interface between the materials forming the device. In this thesis we use first-principles methods to explore the energy-level alignment at the interfaces between the conjugated polymer poly(3-hexylthiophene) (P3HT) and three electron acceptors, zinc oxide (ZnO), gallium arsenide (GaAs) and graphene. We find that V_{OC} reported in the literature for ZnO/P3HT devices is significantly lower than the theoretical maximum and that the interfacial electrostatic dipole plays an important role in the physics underlying the charge transfer at the heterojunction. We note significant charge transfer from the polymer to the semiconductor at GaAs/P3HT interfaces, and use this result to help interpret experimental data. Our findings support the conclusion that charge transferred from P3HT to GaAs nanowires can passivate the surface defect states of the latter and, as a result, account for the observed decrease in photoluminescence lifetimes. Finally, we explore the energy-level alignment at the graphene/P3HT interface and find that V_{OC} reported for experimental devices is in line with the theoretical maximum. The effect of functionalised graphene is also examined, leading to the suggestion that functionalisation might have important consequences for device optimisation.

Contents

Abstract **i**

Contents **iii**

1 Introduction **1**
1.1 The Role of Photovoltaics in Addressing our Future Energy Needs . . . 1
1.2 Photovoltaic Technologies . . . 3
1.2.1 Inorganic Photovoltaic Devices . . . 3
1.2.2 Organic Photovoltaic Devices . . . 4
1.2.3 Hybrid Organic-Inorganic Photovoltaic Devices . . . 5
1.3 Principles of Organic and Hybrid Organic-Inorganic PV Devices 7
1.3.1 Power Conversion Efficiency . . . 7
1.3.2 The Bulk Heterojunction Concept . . . 9
1.3.3 V_{OC} in Organic and Hybrid Organic-Inorganic PV . . . 9
1.3.4 Charge Carrier Recombination . . . 12
1.4 Motivation for this Thesis . . . 13
1.5 Outline of the Thesis . . . 18

2 First-Principles Electronic Structure Methods for Materials Modelling **21**
2.1 The Many-Body Schrödinger Equation . . . 22
2.2 Approximations to the Many-Body Schrödinger Equation . . . 23
2.2.1 The Born-Oppenheimer Approximation . . . 23
2.2.2 The Independent Electron Approximation . . . 24
2.2.3 The Hartree Approximation . . . 25
2.2.4 The Hartree-Fock Approximation . . . 26
2.3 Density Functional Theory . . . 28
2.3.1 The Hohenberg-Kohn Theorems . . . 29
2.3.2 The Kohn-Sham Equations . . . 32
2.3.3 Exchange-Correlation Functionals . . . 35

2.3.4 Plane Wave Basis Sets 37
2.3.5 Pseudopotentials 39
2.3.6 Excited States 43
2.4 Hybrid Functionals 46

3 Considerations for Practical Calculations 49
3.1 Achieving Self Consistency 49
3.2 Calculating Forces 51
3.3 Pseudopotential Transferability 52
3.4 Hybrid Functionals 53
3.5 Comparing Eigenvalues from Different Calculations 54
3.6 Calculating Interfacial Energy-Level Alignments 55
3.7 Dipole Corrections 58
3.8 Charge Neutrality Level 60
3.9 Overview of Experimental Techniques 63

4 Materials for Organic and Hybrid Organic-Inorganic Photovoltaic Devices 65
4.1 Zinc Oxide 66
4.2 Gallium Arsenide 70
4.3 Graphene 73
4.4 Poly(3-hexylthiophene) 76

5 The Ideal ZnO/P3HT Photovoltaic Interface 85
5.1 Introduction 85
5.2 Atomic Structure 86
5.3 Interfacial Energy-Level Alignment 91
5.3.1 DFT Energy-Level Alignment 91
5.3.2 Application of Hybrid Functionals 92
5.4 Open-Circuit Voltage 101
5.4.1 Calculated V_{OC} 101
5.4.2 Electrostatic Dipole 103
5.4.3 Experimental V_{OC} 108
5.5 Quantum Confinement 110
5.6 Conclusions 111

6 GaAs Nanowires Coated with P3HT 113
6.1 Introduction 113
6.2 Model Interfaces 114
6.3 Charge Transfer 118
6.4 Comparison with Experiment 123

6.5 Conclusions 125

7 The Ideal Graphene/P3HT Photovoltaic Interface 127
7.1 Introduction 127
7.2 Atomic Structure 128
7.3 Interfacial Energy-Level Alignment 132
7.3.1 DFT Energy-Level Alignment 132
7.3.2 Application of Hybrid Functionals 135
7.4 Comparison with Experiment 137
7.4.1 Open-Circuit Voltage 137
7.4.2 Functionalised Graphene 139
7.5 Conclusions 143

8 Conclusions 145
8.1 Summary 145
8.2 Outlook 149

A Computational Details 151
A.1 General Notes on the Computational Details 151
A.2 ZnO 152
A.3 GaAs 153
A.4 Graphene 153
A.5 P3HT 154
A.6 ZnO/P3HT 154
A.7 GaAs/P3HT 155
A.8 Graphene/P3HT 156
A.8.1 Functionalised Graphene 157

References 159

Acknowledgements I

Chapter 1

Introduction

1.1 The Role of Photovoltaics in Addressing our Future Energy Needs

"Climate change has quite frankly slipped to the back burner of policy priorities. But the problem is not going away - quite the opposite." These were the words of the Executive Director of the International Energy Agency (IEA), Maria van der Hoeven, as she launched the agency's World Energy Outlook Special Report earlier this year [1]. The highlights of the report paint a bleak picture for the course of current carbon dioxide (CO_2) emissions from fossil fuels [2]. Specifically, the report notes that that CO_2 emissions in 2012 were 1.4% higher than the preceding year, hitting an all time high of 31.6 gigatonnes. Referring to the agency's *The 2 °C Scenario* (2DS) - a set of prescriptions designed to limit the global average temperature increase to 2 °C - van der Hoeven added: "This report shows that the path we are currently

on is more likely to result in a temperature increase of between 3.6 °C and 5.3 °C but also finds that much more can be done to tackle energy-sector emissions without jeopardising economic growth, an important concern for many governments." As one of four suggestions proffered by the IEA to get CO_2 emissions back in line with the 2DS, the agency recommends an increase in the share of power generation from renewable sources from the current 20% to 27% by the end of the decade. Renewables, therefore, must form an integral part of any discussion on the future of climate change policy and energy technologies.

One of the most promising renewable energy technologies is the solar cell, or photovoltaic (PV) device, in large part due to the vastness of solar energy available, which is theoretically larger than any other renewable resource [3]. By end of 2010 there were 30 GW of PV installed worldwide, representing a nearly 15-fold increase over the last decade [3].

Meanwhile, in its latest energy briefing [4], the UK's Department of Energy and Climate Change notes that while electricity generation from renewable energy sources increased to 9.4% in 2011, less than 1% was generated by solar PV. Moreover, in 2011 the UK imported 36% more of its energy than in 2010, largely as a result of crude oil imports. Given the vastness of the solar energy resource, the low percentage of PV-generated electricity, and the high percentage of imported energy, the UK would do well to invest more in the study and implementation of PV technologies.

At its root, this thesis is focused on photovoltaic technologies and the ongoing effort to improve their efficiencies and lower their costs, with the ultimate aim of making them a viable alternative to fossil fuels for energy

generation. The following section presents an overview of PV technologies.

1.2 Photovoltaic Technologies

1.2.1 Inorganic Photovoltaic Devices

All photovoltaic devices, regardless of the specific technology upon which they are based, perform the task of directly converting light energy into electrical energy. At present, photovoltaic devices are dominated by single-junction devices based on crystalline silicon [5]. Thin-film photovoltaic devices are also common, and include technologies based on amorphous silicon, II-IV semiconductors such as CdS and CdTe, and chalcogenides including $CuInSe_2$ (CIS) and $CuInGaSe_2$ (CIGS) (see Ref. 5 and references therein). All inorganic PVs work under the same principle. When a photon is absorbed by the optically active material, an electron is excited from the ground state leaving behind a positively charged hole. A built-in electric field, set up by the presence of p-n junction (i.e. the interface between p-type and n-type semiconductors), provides the driving force to separate the charges and guide them to opposing electrodes.

Single-junction inorganic PV devices have reached power conversion efficiencies approaching the theoretical maximum calculated by Shockley and Queisser [6], while multi-junction, or tandem, devices have exceeded this limit by stacking two or more single-junction cells one on top of the other. Despite the tremendous progress in the field of inorganic photovoltaics, the cost associated with the manufacture and installation of completed modules [7],

while declining dramatically in recent years, has been a key factor in limiting the widespread adoption of photovoltaic devices.

1.2.2 Organic Photovoltaic Devices

An alternative photovoltaic technology is organic PV, which uses π-conjugated organic semiconductor materials, including small molecules and conjugated polymers [8]. Here π-conjugation refers to the overlap (conjugation) of the C p_z orbitals, resulting in the formation of delocalised π molecular orbitals, which constitute the highest occupied molecular orbital (HOMO) and lowest unoccupied molecular orbital (LUMO) levels of the organic compound [5]. The use of organic semiconductors instead of inorganic ones confers several benefits in the context of PV applications. Organic materials can be deposited using low-cost, low-temperature techniques (e.g. solution or vapour deposition), which reduces the energy used during manufacture, greatly increases the range of substrates onto which they can be deposited vis-à-vis inorganic semiconductors, and permits the use of low-cost, flexible substrates [5, 8, 9]. These properties allow for the use of low-cost, large-area, high-throughput manufacturing techniques, which, when coupled with the generally lower cost of organic materials, conspire to reduce the overall module construction and installation costs [5, 8]. The nature of these organic compounds also enables their chemical tuning and thus allows their properties to be tailored for specific applications [5, 8].

The operating principles of an organic PV cell differ from those of their inorganic counterparts. As with inorganic PV devices, an electron is ex-

cited from the ground state upon absorption of a photon, leaving behind a positively charged hole. The electron-hole pairs in organic PVs, however, are tightly bound excitons - with binding energies typically in the region 0.5 eV (see Ref. [10] and references therein) - and a built-in electric field is not sufficient to dissociate them. The exciton dissociation in organic PVs is accomplished via an electron donor/electron acceptor interface as follows. An incoming photon is absorbed in the donor material, forming an exciton. If the exciton manages to diffuse to the donor/acceptor interface before it recombines, it will dissociate provided the offset of the LUMO levels of the donor and acceptor are larger than the exciton binding energy. This separation leaves the hole on the donor and electron on the acceptor, with both charge carriers free to diffuse to their respective electrodes [5, 11]. This simplified process is shown in Figure 1.1. In practice, the situation is much more complicated and properties such as the exciton diffusion length, charge carrier pathways and charge mobilities must also be considered [5, 11].

1.2.3 Hybrid Organic-Inorganic Photovoltaic Devices

Hybrid organic-inorganic photovoltaics [12] are identical to all-organic devices in their operational principle. The difference between the two is in the choice of the electron acceptor material, which in the case of hybrid PV devices is an inorganic semiconductor. This permits the combination of the benefits of organic semiconductors, highlighted above, with those of inorganic semiconductors, which include high charge mobility and optical absorption tunability via quantum confinement [13, 14]. Moreover, the pres-

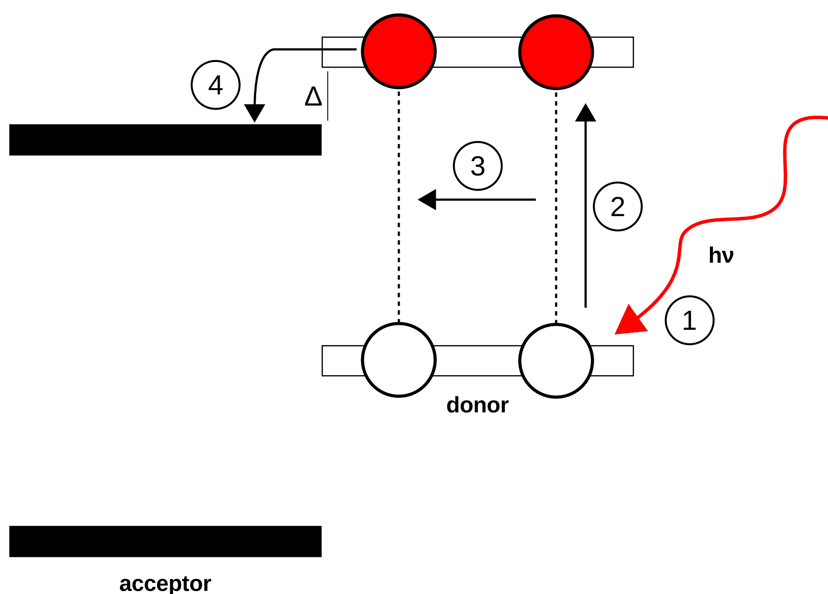

Figure 1.1: Simplified schematic of the operation of an excitonic PV device. (1) An incident photon with energy $h\nu$ excites an electron in the donor material, (2) generating a tightly bound electron-hole pair (i.e. an exciton). (3) The exciton diffuses to the donor/acceptor interface. (4) Provided the offset of the LUMO levels of the donor and acceptor (Δ) is larger than its binding energy, the exciton is dissociated into an electron and a hole, with the electron moving to the acceptor and the hole remaining in the donor.

ence of an inorganic semiconductor facilitates the fabrication of an ordered bulk heterojunction [15] by forming a network into which an organic donor can be infiltrated, which can be optimised to enhance exciton diffusion and dissociation.

1.3 Principles of Organic and Hybrid Organic-Inorganic PV Devices

1.3.1 Power Conversion Efficiency

The photocurrent generated by a PV device is related to the light intensity incident upon it. The photocurrent density at short circuit can be expressed as [16]

$$J_{\mathrm{SC}} = q \int b_s(E) EQE(E) dE, \tag{1.1}$$

where q is the electronic charge and $b_s(E)$ is the photon flux incident on the device. $EQE(E)$ is the external quantum efficiency and is defined as [17]

$$EQE(E) = A(E)\eta_G(E)Q(\mu\tau), \tag{1.2}$$

where $A(E)$ is the absorption spectrum of the PV device, $\eta_G(E)$ is the photogeneration efficiency (i.e. the ratio of the number of charge carriers generated by the device to the number of photons absorbed), and $Q(\mu\tau)$ is the charge collection efficiency, which is a function of the mobility and lifetime of the charge carriers. It is important to note that the dependencies on energy shown in Equation 1.1 and Equation 1.2 can also be related to the wavelength of light via

$$E = \frac{hc}{\lambda}, \tag{1.3}$$

where h is Planck's constant and c is the speed of light in vacuum.

When not under illumination, the PV device will still generate a current, $J_{\mathrm{dark}}(V)$, which is caused by the potential buildup across it and flows in the

direction opposite J_{SC}, such that the total current flowing in the device is

$$J(V) = J_{\mathrm{SC}} - J_{\mathrm{dark}}(V). \tag{1.4}$$

The open circuit voltage (V_{OC}) of the PV device corresponds to operating the device with no net flow of current or, equivalently, when J_{SC} is exactly equal to J_{dark}.

The power generated by the PV device is the product of its current (Equation 1.4) and its operating voltage, V, such that

$$P = JV. \tag{1.5}$$

The maximum power output of the cell is achieved at some maximum current, J_m, and a corresponding operating voltage, V_m. The *fill factor* of the cell is then defined as

$$FF = \frac{J_m V_m}{J_{\mathrm{SC}} V_{\mathrm{OC}}}. \tag{1.6}$$

Given a power density, P_s, of the incident light, the power conversion efficiency of the PV device is expressed as

$$\eta = \frac{J_m V_m}{P_s}. \tag{1.7}$$

In terms of J_{SC}, V_{OC}, and FF this becomes

$$\eta = \frac{J_{\mathrm{SC}} V_{\mathrm{OC}} FF}{P_s}. \tag{1.8}$$

Equation 1.8 indicates that the device efficiency of a photovoltaic device is

critically dependent on its short circuit current, open circuit voltage and fill factor, all of which are properties intrinsic to the device.

1.3.2 The Bulk Heterojunction Concept

The structure illustrated in Figure 1.2(b) and (c), in which two semiconductors with differing energy levels are patterned together, is known as a bulk heterojunction (BHJ) [18], and has been key to the success of organic and hybrid organic-inorganic PV [19]. These BHJ structures are typically made by casting a solution containing the two semiconductors and creating two distinct phases in the blend [15]. By controlling the structure of the phases at the nanoscale, it is possible to limit the distance a generated exciton must travel before it reaches a donor/acceptor interface, thus guaranteeing that it will reach such an interface before it decays. A well controlled BHJ can also limit dead-end pathways for separated charge carriers, reducing the probability of carrier recombination before the charges reach the electrodes. A summary of the BHJ concept is shown schematically in Figure 1.2.

1.3.3 V_{OC} in Organic and Hybrid Organic-Inorganic PV

As shown in Equation 1.8, the open circuit voltage of a PV device is critical in determining its power conversion efficiency. Estimating the maximum V_{OC} for an organic or hybrid organic-inorganic PV device is therefore a crucial step in optimising the performance of these devices.

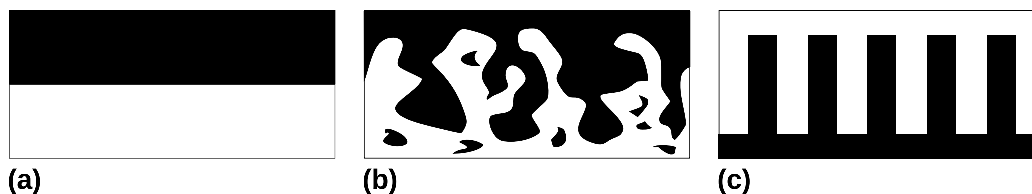

Figure 1.2: (a) A bilayer donor/acceptor junction. If an exciton is generated far from the interface it will recombine before it can diffuse to the heterojunction. (b) A bulk heterojunction donor/acceptor interface. The blending of the two phases increases the donor/acceptor interface surface area and results in shorter distances for excitons to reach an interface. (c) An ideal ordered bulk heterojunction interface. This structure eliminates dead-end pathways for charge carriers and ensures that all donor/acceptor interfaces are within an exciton diffusion length from each other, minimising the chance of exciton recombination.

Metal-Insulator-Metal Model

For thin, single-layered organic PV devices, in which the active layers is composed of a single organic polymer, the current-voltage characteristics are effectively independent of the operating voltage over a wide range of cathode workfunctions. The I-V characteristics instead depend on the strength of the electric field across the device [20], determined by the active layer thickness and the applied bias. This behaviour clearly suggests that charge carrier injection follows a tunnelling model and that the active polymer layer behaves as an insulator. As such, the maximum open circuit voltage for such a device is then the difference between the workfunctions of the two electrodes and the model is referred to as the metal-insulator-metal (MIM) model.

Fermi-Pinning Model

The MIM model does not hold for BHJ devices since mixing the acceptor with the conducting polymer destroys the thin-film nature of the latter. The

determination of the maximum V_{OC} in organic and hybrid organic-inorganic BHJ PV devices is more complicated. Brabec et al. [21] demonstrated that the open circuit voltage of BHJ organic shows a strong, linear relationship with the acceptor strength (i.e. LUMO) and negligible correlation with the workfunction of the negative electrode. This observation indicates that the negligible correlation between V_{OC} and the workfunction of the cathode is due to Fermi level pinning [22]. For metal-semiconductor interfaces, this process involves the pinning of the workfunction of the metal to the workfunction of the semiconductor via surface states. In the case of a metal-organic semiconductor interface, Brabec et al. proposed that the workfunction of the negative electrode is pinned to the LUMO of the organic acceptor. It is important to note that this pinning mechanism is fundamentally at odds with the MIM model.

Building on the work of Brabec et al., Scharber et al. [23] found that the V_{OC} of organic PV devices varied directly with the strength of their oxidation potentials (i.e. HOMO levels) and that, further, no dependence on the positive electrode workfunction was observed. Coupled with the negative electrode pinning described by Brabec et al., Scharber and coworkers showed that the maximum open circuit voltage of an organic PV device can be determined as the difference between the LUMO level of the acceptor and the HOMO level of the donor,

$$V_{\mathrm{OC,max}} = E^{A}_{\mathrm{LUMO}} - E^{D}_{\mathrm{HOMO}}, \tag{1.9}$$

where E^{A}_{LUMO} represents the LUMO energy level of the acceptor and E^{D}_{HOMO}

the HOMO energy level of the acceptor. As this thesis deals with BHJ organic and hybrid organic-inorganic PV systems, Equation 1.9 will be used throughout when estimating the maximum open circuit voltage of a given PV system.

Electron Affinity Rule

The electron affinity (EA) rule [24] is a method to determine the energy-level alignment of two semiconducting materials that form a heterojunction. In practice, the EA rule allows for a quick and simple prediction of the maximum V_{OC} of an organic or hybrid organic-inorganic PV by providing the relative positions of E^{A}_{LUMO} and E^{D}_{HOMO} and the donor/acceptor interface. In the EA procedure, the bulk electron affinity (EA) levels of the two semiconductors are aligned via their offsets with a common vacuum level. The relative positions of the ionisation potential (IP) levels can then be determined using the band gaps of the materials. The procedure works equivalently if only the EA levels of the materials are known so long as their band gaps are available. Since this method relies on the bulk EA (or IP) levels and band gaps, however, it neglects any structural or electronic changes resulting from the interactions of the materials forming the interface. This limitation will be discussed in more detail later in this thesis.

1.3.4 Charge Carrier Recombination

Recombination refers to the process in which the interaction between an electron and a hole causes both carriers to be annihilated [11]. Recombination

occurs when the electrons and holes generated upon dissociation of an exciton at the donor/acceptor interface do not exit the PV device at the electrodes. Two broad types of recombination processes exist, namely radiative and non-radiative. Radiative recombination refers to the process by which the energy and momentum of an annihilated electron-hole pair is carried away by a photon. Non-radiative recombination, by contrast, does not involve emission of a photon. Rather, in this case the energy and momentum generated by the annihilated electron-hole pair is scattered into phonons and is often mediated by surface or defect states. An example would be an excited electron emitting a phonon and relaxing to a mid-band gap state, after which another phonon emission causes it relax back to the ground state. Another type of non-radiative recombination, known as Auger recombination, involves the transfer of the energy and momenta of an annihilated pair to another charge carrier, which is then excited to generate a second electron-hole pair. This second pair can then be annihilated by another the non-radiative phonon scattering process just described.

1.4 Motivation for this Thesis

From Equation 1.8 we see that efficiency of a PV device depends critically on both J_{SC} and V_{OC}. While the former can be quite low in BHJ organic and hybrid organic-inorganic PV, due to a value of $Q(\mu\tau)$ considerably smaller than one [17] (see Equation 1.2), in this thesis we focus exclusively on V_{OC} as it is more readily analysed by first principles. The open-circuit voltage in organic and hybrid organic-inorganic PV remains low and, as a consequence,

represents one of the major limiting factors to high device efficiencies.

As mentioned in Section 1.3.3, we need to know the interfacial energy-level alignment in order to determine the maximum V_{OC} achievable by an organic or hybrid organic-inorganic PV device. A detailed atomic-scale description of these interfaces is therefore a necessity if we are to gain a better understanding of the physics underlying their energy-level alignment. To that end, a first-principles, atomic-scale approach is ideally suited for the study of interfacial physics at organic and hybrid organic-inorganic PV interfaces. This thesis attempts to use this first-principles approach to examine materials that have been under active study over the past decade, namely the inorganic semiconductors zinc oxide (ZnO) and gallium arsenide (GaAs), graphene, and the conjugated polymer poly(3-hexylthiophene) (P3HT). ZnO and GaAs are used as electron acceptors in hybrid organic-inorganic PV, while graphene acts as the acceptor in organic PV. P3HT is used as an electron donor for all three of these acceptors. The motivations for studying the ZnO/P3HT, GaAs/P3HT and graphene/P3HT interfaces are elaborated below.

ZnO/P3HT

In the past six years, hybrid organic-inorganic photovoltaic devices based on ZnO and P3HT have received considerable attention [25], due in large part to the ease of processing ZnO at low temperatures [26] and high hole mobility of P3HT (up to 0.1 $cm^2V^{-1}s^{-1}$ [27]). Between 2006 and 2011 hybrid organic-inorganic ZnO/P3HT photovoltaic devices using a semiconductor/polymer bilayer [28–33], quantum dot/polymer blends [28, 34–38], infil-

trated nanowire arrays [28, 29, 32, 39–43], polymer-coated single nanowires [44], and nanorod/polymer blends [38] were demonstrated.

Despite the progress that has been made, the power conversion efficiencies of these devices has not exceeded 2% due to low short-circuit currents and open circuit voltages in the range of 0.4-0.8 V [45]. In an attempt to explain these shortcomings, the effects of substrate processing [32], doping [30], surface treatment [33], and polymer morphology [42] on the performance of hybrid ZnO/P3HT devices have been examined in detail. To date, however, the atomic-scale physics underlying the open circuit voltage has not been investigated in depth and, therefore, a detailed investigation and understanding of the energy-level alignment at the ZnO/P3HT interface is vital in order to determine its ideal open circuit voltage and to help identify new avenues for optimisation.

GaAs/P3HT

Aside from those using ZnO, a large variety of hybrid organic-inorganic photovoltaic devices have been reported that employ π-conjugated polymers, such as polythiophene or polyphenylenevinylene (PPV) derivatives, in conjunction with inorganic semiconductors including gallium arsenide (GaAs) [46], cadmium selenide (CdSe) [12, 47, 48], indium phosphide (InP) [49], and lead selenide (PbSe) [50]. Semiconductor nanowires (NWs) are attractive for use in hybrid photovoltaics because they facilitate the construction of ordered BHJ structures. These structures offer direct charge pathways to electrodes, large surface areas, high carrier mobilities along the nanowire,

and chemical and physical stability [12, 46, 49, 51–53]. Surface defect states, however, strongly affect the charge transport in these NWs by acting as charge traps [54–56]. In an effort to passivate such traps various methods have been devised, including overgrowing the nanowire surface with a layer of large-band gap semiconductor [54, 57] and treatment with sulfides [58]. These overcoats, however, can also form a barrier to charge generation at the nanowire interface when embedded in a π-conjugated polymer matrix as part of a BHJ hybrid photovoltaic device. An ideal solution, therefore, would be to find a conjugated polymer that not only forms a suitable BHJ interface but also effectively passivates the traps caused by the NW surface defect states. P3HT has been proposed as one of several possible passivating overcoat layers for GaAs NWs [59] and the determination of the interfacial energy-level alignment at this interface is therefore crucial to understanding whether or not such a passivation takes place and the physics that might drive such a process.

Graphene/P3HT

Organic photovoltaic devices based on BHJ blends of fullerenes and conjugated polymers have made remarkable progress in recent years, with power conversion efficienes reaching 6-7% [60–62]. In particular, the solution processability and low-cost manufacturing, in addition to the possibility of deposition onto flexible substrates [63–65], make organic PV devices a promising alternative to inorganic semiconductor-based photovoltaic devices.

The blend of the conjugated polymer poly(3-hexylthiophene) (P3HT)

with fullerenes is amongst the most commonly studied BHJ organic PVs. First-principles calculations [66] have revealed revealed optimal characteristics for this interface, and experimental devices have reached power conversion efficiencies of 5.5-6.5% [67, 68]. There are, however, limitations to using fullerenes, including their weak absorption in the visible range and a low LUMO energy [62], which leads to a small offset with the HOMO of the P3HT and thus a small maximum V_{OC}. Furthermore, the presence of trap states in the blended fullerene/P3HT complex results in dead-end pathways for charge carriers and hinders electron transport [69].

Carbon nanotubes (CNTs) represent an alternative to fullerene and fullerene derived acceptors. CNTs have high charge mobility and can form an interpenetrating network with P3HT [70], allowing in principle for more efficient charge dissociation than fullerenes and their derivatives. In practice, however, CNT-based OPVs suffer from low power conversion efficiencies (<0.5% [70, 71]), which is largely the result of the aggregation and inconsistent lengths and diameters of the tubes, as well as the mixing of both metallic- and semiconducting-type tubes [72]. First-principles calculations [73] have demonstrated that CNT/P3HT blends show photovoltaic characteristics only for semiconducting CNTs.

Instead of using fullerenes or CNTs, a more recent approach has been to use graphene as an electron acceptor [74]. Graphene is well suited to photonic applications [75, 76] and its high mobility and two-dimensional structure render it particularly useful for OPV devices. Graphene can also be rendered solution-processable via functionalisation [74]. Using graphene as the acceptor, OPV devices with a P3HT donor have reached efficiencies as high as

1.1% for BHJ cells made with solution-processable functionalised graphene (SPFGraphene) [77–80] and 1.28% for cells made with graphene quantum dots (GQDs) [81].

In spite of the active study of graphene/P3HT OPVs, there remains a discrepancy in the range of V_{OC} reported for experimental devices [74] and those determined using the electron affinity rule. While several explanations for this discrepancy have been proposed [79], the precise reason for these differences has not yet been determined in the literature, and to date no detailed atomic-scale investigation of the energy-level alignment at the graphene/P3HT interface has been conducted.

1.5 Outline of the Thesis

This thesis attempts to form a coherent description of the theory and application of first-principles techniques to studying the atomic and electronic properties of organic and hybrid organic-inorganic photovoltaic devices. In Chapter 2 we examine the foundations of the theories used to model and study the structural and electronic properties of atomic-scale systems. In Chapter 3 we present practical considerations for the specific model systems presented in this thesis. The goal of Chapter 4 is to study the properties of the individual components that make up the model systems introduced in Section 1.4 and described in detail in Chapters 5-7. The main discussion of this work is left to those chapters. In Chapter 5 we describe the energy-level alignment at the ZnO/P3HT interface from first principles and discuss its implication for the maximum V_{OC} of such hybrid PV devices. In Chapter

6 we discuss the GaAs/P3HT interface and examine the energy-level alignment and charge transfer with a view to clarify experimental results. Finally, in Chapter 7 we investigate the graphene/P3HT interface and consider the effects of the energy-level alignment and graphene functionalisation on the open circuit voltage. Chapter 8 concludes the thesis and summarises its results, while also attempting to provide a future outlook on the first principles study of organic and hybrid organic-inorganic PV.

Chapter 2

First-Principles Electronic Structure Methods for Materials Modelling

Before exploring the organic and hybrid organic-inorganic interfaces described in Chapter 1.4, it is important to understand the underlying theoretical framework. This chapter provides the theoretical background for first-principles calculations involving systems comprising hundreds of atoms. It is by no means intended to provide an exhaustive review of the theory nor of every technique available. Rather, its intent is to present the theoretical tools used in the study of the systems presented in this thesis. For the purposes of clarity and concision, some topics will not be covered in a detailed fashion; in these cases the reader is encouraged to peruse the references provided if more information is desired.

2.1 The Many-Body Schrödinger Equation

In order to study systems composed of many atoms we need a method of describing the interactions between the constituent electrons and nuclei of such systems. In a first-principles approach the starting point for such a description is the Schrödinger equation. In its time-independent and non-relativistic form it is expressed as

$$\hat{H}\Psi = E\Psi. \tag{2.1}$$

In this expression Ψ represents the many-body wavefunction of the system. For a system with N electrons and M nuclei the many-body wavefunction can be expressed as

$$\Psi = \Psi(\{\mathbf{r}_i\}, \{\mathbf{R}_I\}), \tag{2.2}$$

where $i = 1..N$ and $I = 1..M$, and $\mathbf{r}_i$ and $\mathbf{R}_I$ represent the positions of the electrons and nuclei, respectively. From Equation 2.2 it is clear that the many-body wavefunction depends explicitly on the location of all of the particles in the system. The Hamiltonian of the system is given by

$$\begin{aligned}\hat{H} = -\sum_i \frac{\hbar^2}{2m_e}\nabla_i^2 - \sum_I \frac{\hbar^2}{2M_I}\nabla_I^2 - \sum_{i,I} \frac{e^2}{4\pi\epsilon_0}\frac{Z_I}{|\mathbf{r}_i - \mathbf{R}_I|} + \\ \frac{1}{2}\sum_{i\neq j} \frac{e^2}{4\pi\epsilon_0}\frac{1}{|\mathbf{r}_i - \mathbf{r}_j|} + \frac{1}{2}\sum_{I\neq J} \frac{e^2}{4\pi\epsilon_0}\frac{Z_I Z_J}{|\mathbf{R}_I - \mathbf{R}_J|}.\end{aligned} \tag{2.3}$$

The first two terms describe the kinetic energy of the electrons and nuclei with masses m_e and M_I, respectively. The third term represents the Coulomb interaction between the electrons and the nuclei, and the final two terms

describe, respectively, the electron-electron and nucleus-nucleus interactions. We can simplify Equation 2.3 by using Hartree atomic units,

$$\hat{H} = -\sum_i \frac{\nabla_i^2}{2} - \sum_I \frac{\nabla_I^2}{2M_I} - \sum_{i,I} \frac{Z_I}{|\mathbf{r}_i - \mathbf{R}_I|} + \frac{1}{2}\sum_{i \neq j} \frac{1}{|\mathbf{r}_i - \mathbf{r}_j|} + \frac{1}{2}\sum_{I \neq J} \frac{Z_I Z_J}{|\mathbf{R}_I - \mathbf{R}_J|}. \tag{2.4}$$

In practice, the analytical or numerical solution to Equation 2.1 is intractable and adequate approximations must be made in order to render the many-body Schrödinger equation into a soluble form.

2.2 Approximations to the Many-Body Schrödinger Equation

2.2.1 The Born-Oppenheimer Approximation

In an effort to facilitate the solution to Equation 2.1 we note that, in general, $M_I \gg m_e$ and, as a consequence, the nuclei move much slower than the electrons. As a result, we can neglect the kinetic energy of the nuclei and the repulsion between the nuclei becomes a constant. Equation 2.3 reduces to an electronic Hamiltonian

$$\hat{H}_e = -\sum_i \frac{\nabla_i^2}{2} - \sum_{i,I} \frac{Z_I}{|\mathbf{r}_i - \mathbf{R}_I|} + \frac{1}{2}\sum_{i \neq j} \frac{1}{|\mathbf{r}_i - \mathbf{r}_j|} \tag{2.5}$$

and can be solved by

$$\hat{H}_e \Psi_e = E_e \Psi_e. \tag{2.6}$$

Here the wavefunctions Ψ_e represent electronic wavefunctions that depend explicitly on the positions of the electrons $\mathbf{r}_i$, such that

$$\Psi_e = \Psi_e(\{\mathbf{r}_\mathrm{i}\}). \tag{2.7}$$

The positions of the nuclei affect the electronic wavefunctions parametrically via the electronic Hamiltonian.

2.2.2 The Independent Electron Approximation

The major difficulty associated with the solution of the many-body Schrödinger equation is in the long-range Coulombic interaction between the electrons. In order to further simplify the electronic Hamiltonian of Equation 2.5 a first approximation would be to simply neglect the electron-electron interaction. This is known as the independent electrons approximation and allows us to factorise the many-electron wavefunction (Equation 2.7) into a product of one-electron wavefunctions

$$\Psi_e = \prod_i \phi_i(\mathbf{r}_i). \tag{2.8}$$

The many-electron Schrödinger equation of Equation 2.6 can consequently be rewritten as a set a of single-electron equations

$$\hat{H}_i^0 \phi_i(\mathbf{r}_i) = \epsilon_i \phi_i(\mathbf{r}_i), \tag{2.9}$$

where the term $\hat{H}_i^0$ is the independent electron Hamiltonian,

$$\hat{H}_i^0 = -\frac{\nabla_i^2}{2} - \sum_{i,I} \frac{Z_I}{|\mathbf{r}_i - \mathbf{R}_I|}. \tag{2.10}$$

The independent electron approximation renders the Schrödinger equation much easier to solve as the two-particle Coulomb interaction between electrons is removed. However, this approximation leads to unsatisfactory results since the Coulomb interaction of the electrons is significant and on the same order as the other terms in Equation 2.5.

2.2.3 The Hartree Approximation

Ideally we would like to find an approximation to the Schrödinger equation that allows us to use single particle Hamiltonians while also including the effect of the electron-electron interactions. In the Hartree approximation we retain the independent-electron description while accounting for the electron-electron interaction by treating the electrons as a smooth distribution of negative charge with charge density $n(\mathbf{r})$. Since the electronic wavefunctions remain independent (as in Equation 2.8) we can express the density as

$$n(\mathbf{r}) = \sum_i |\phi_i(\mathbf{r})|^2. \tag{2.11}$$

The mean field can then be calculated using Poisson's equation,

$$\nabla^2 V_{\mathrm{H}}(\mathbf{r}) = -4\pi n(\mathbf{r}), \tag{2.12}$$

where V_{H} is the Hartree potential. Solving Equation 2.12 for V_{H} gives

$$V_{\mathrm{H}}(\mathbf{r}) = -\int d\mathbf{r}' \frac{n(\mathbf{r}')}{|\mathbf{r} - \mathbf{r}'|}. \tag{2.13}$$

By adding the Hartree potential to the independent particle Hamiltonian of Equation 2.10 we get the Hartree Hamiltonian,

$$\hat{H}_{\mathrm{H}} = -\frac{\nabla_i^2}{2} - \sum_{i,I} \frac{Z_I}{|\mathbf{r}_i - \mathbf{R}_I|} - \int d\mathbf{r}' \frac{n(\mathbf{r}')}{|\mathbf{r} - \mathbf{r}'|}. \tag{2.14}$$

2.2.4 The Hartree-Fock Approximation

While the Hartree approximation does include the effect of the electron-electron interactions via a mean field, because of the independent nature of Equation 2.8 its wavefunctions are not compatible with the Pauli exclusion principle, which requires the wavefunction to be antisymmetric with respect to the interchange of any two of its arguments (i.e. the sign of the wavefunction must change when any two arguments are exchanged).

We can generalise and improve the Hartree approximation by imposing the Pauli exclusion condition on the one-electron wavefunctions[1]. This is done by using a Slater determinant, which is the linear combination of the all possible products of the one-particle wavefunctions ($\{\phi_i(\mathbf{r}_i)\}$) obtainable by the permutation of their arguments. This antisymmetrised wavefunction can be expressed in a compact form known as the Slater determinant, which

[1]We note that the electron spin is ignored in this and subsequent discussions as only non spin-polarised calculations are performed in this thesis.

for a N-electron systems takes the $N \times N$ determinant form

$$\Psi_e(\{\mathbf{r}_i\}) = \frac{1}{\sqrt{N!}} \begin{vmatrix} \phi_1(\mathbf{r}_1) & \phi_2(\mathbf{r}_1) & \dots & \phi_N(\mathbf{r}_1) \\ \phi_1(\mathbf{r}_2) & \phi_2(\mathbf{r}_2) & \dots & \phi_N(\mathbf{r}_2) \\ \vdots & \vdots & \ddots & \vdots \\ \phi_1(\mathbf{r}_N) & \phi_2(\mathbf{r}_N) & \dots & \phi_N(\mathbf{r}_N) \end{vmatrix}. \tag{2.15}$$

These wavefunctions must be orthonormal such that $\langle \phi_i | \phi_j \rangle = \delta_{ij}$. Using the wavefunction of Equation 2.15 we can minimise the electronic Hamiltonian of Equation 2.6 using the variational principle[2] to obtain a new set of equations. We first take the expectation value of $\hat{H}_e$ with respect to the wavefunctions of Equation 2.15 to get the energy of the system

$$E_e = \langle \Psi_e | \hat{H}_e | \Psi_e \rangle, \tag{2.16}$$

and then minimise this with respect to the variation of the one-particle wavefunctions $\{\phi_i(\mathbf{r}_i)\}$

$$\frac{\delta E_e}{\delta \phi_i^*} = 0. \tag{2.17}$$

Solving Equation 2.17 leads to a new set of equations known as the Hartree-Fock equations

$$\hat{H}_{\mathrm{H}} \phi_i(\mathbf{r}) + \int d\mathbf{r}' \, V_{\mathrm{HF}}(\mathbf{r}, \mathbf{r}') \phi_i(\mathbf{r}') = \epsilon_i \phi_i(\mathbf{r}). \tag{2.18}$$

[2] The variational principle states that given a system with Hamiltonian $\hat{H}$, then for any trial wavefunction Ψ, the expectation value of the Hamiltonian is greater than or equal to the ground state energy of the system E_0 (i.e. $\langle \Psi | \hat{H} | \Psi \rangle \geq E_0$). This principle allows us to find the upper bound on the true ground state energy by minimising the energy with respect to the trial wavefunctions.

These equations are similar to the Hartree equations but feature an additional non-local (two-particle) term know as the exchange term. The potential V_{HF} is the Hartree-Fock potential and is expressed as

$$V_{\mathrm{HF}} = -\sum_i \frac{\phi_i(\mathbf{r})\phi_i^*(\mathbf{r}')}{|\mathbf{r}-\mathbf{r}'|}, \tag{2.19}$$

where the index i runs from $1..N$.

2.3 Density Functional Theory

The Hartree-Fock approximations is a wavefunction-based approach. In contrast, density functional theory (DFT) relies on only the electronic ground state density $n(\mathbf{r})$ as the fundamental variable. In other words, the wavefunction-dependence of Hartree-Fock is replaced by a dependence on a single scalar function of position. At its core, DFT states that any property of a system of N interacting particles is a functional of the ground state density, where

$$n(\mathbf{r}) = N \int d\mathbf{r}_2 \ldots d\mathbf{r}_N \, |\Psi(\mathbf{r}_i)|^2, \tag{2.20}$$

and the number of particles can be computed as

$$N = \int n(\mathbf{r}) d\mathbf{r}. \tag{2.21}$$

The history of DFT begins with the Thomas-Fermi model in 1927. In this approach the kinetic energy of a system of electrons can be written as an explicit functional of the ground state density. Hohenberg and Kohn (1964)

took the idea of the density as a fundamental variable and demonstrated that the density functional could provide an exact description of many-body systems. Building on the work of Hohenberg and Kohn, Kohn and Sham (1965) formulated a set of self-consistent equations that recast the many-body Schrödinger equation into a form that can be solved much more readily and, at least in principle, exactly.

2.3.1 The Hohenberg-Kohn Theorems

The intial work done by Hohenberg-Kohn [82] set out two theorems that underpin DFT. The two theorems state

1. For a system of interacting particles subject to an external potential $v(\mathbf{r})$, this potential is determined uniquely, up to a constant, by the ground state density $n(\mathbf{r})$;

2. We can define a universal functional of the energy $E[n]$ in terms of the density $n(\mathbf{r})$ that is valid for any external potential $v(\mathbf{r})$. For any given $v(\mathbf{r})$, the ground state energy is the global minimum of $E[n]$ and the density that minimises $E[n]$ is the ground state density.

The first theorem can be proven in the following manner. Suppose that there are two different external potentials, $v_1(\mathbf{r})$ and $v_2(\mathbf{r})$, which differ by more than a constant, that lead to the same ground state density $n(\mathbf{r})$. Then the two potentials lead to two different Hamiltonians, $\hat{H}_1$ and $\hat{H}_2$, which have two different ground state wavefunctions, Ψ_1 and Ψ_2. Since Ψ_1 and Ψ_2 are different and since Ψ_2 is the not ground state of $\hat{H}_1$ it follows, by the

variational principle, that

$$E_1 = \langle \Psi_1 | \hat{H}_1 | \Psi_1 \rangle < \langle \Psi_2 | \hat{H}_1 | \Psi_2 \rangle. \tag{2.22}$$

We assume here that the ground states of $\hat{H}_1$ and $\hat{H}_2$ are non-degenerate. We can express the last term in Equation 2.22 as

$$\langle \Psi_2 | \hat{H}_1 | \Psi_2 \rangle = \langle \Psi_2 | \hat{H}_2 | \Psi_2 \rangle + \langle \Psi_2 | \hat{H}_1 - \hat{H}_2 | \Psi_2 \rangle \tag{2.23}$$

$$= E_2 + \int d\mathbf{r}\, n(\mathbf{r}) \left[v_1(\mathbf{r}) - v_2(\mathbf{r}) \right]. \tag{2.24}$$

Inserting Equation 2.24 into 2.22 we have

$$E_1 < E_2 + \int d\mathbf{r}\, n(\mathbf{r}) \left[v_1(\mathbf{r}) - v_2(\mathbf{r}) \right]. \tag{2.25}$$

Similarly, if we repeat this procedure starting with E_2 we obtain

$$E_2 < E_1 + \int d\mathbf{r}\, n(\mathbf{r}) \left[v_2(\mathbf{r}) - v_1(\mathbf{r}) \right]. \tag{2.26}$$

Adding Equations 2.25 and 2.26 leads to the contradictory statement $E_1 + E_2 < E_1 + E_2$. Therefore there cannot be two external potentials, which differ by more than a constant, that lead to the same ground state density and, as a consequence, the ground state density uniquely defines the external potential to within a constant. As the Hamiltonian is fully defined, up to a constant, by the ground state density, so too are the many-body wavefunctions of all the states.

The second theorem can be proven as follows. First we restrict the proof to densities $n(\mathbf{r})$ that are "v-representable", that is they are ground state densities of an electronic Hamiltonian with some external potential $v(\mathbf{r})$. In this case all elements of the Hamiltonian can be written as functionals of the density such that the energy of the system can be expressed as

$$E_{\text{HK}} = T[n(\mathbf{r})] + V_{ee}[n(\mathbf{r})] + \int d\mathbf{r}\, v(\mathbf{r})n(\mathbf{r}) \tag{2.27}$$

$$= F_{\text{HK}} + \int d\mathbf{r}\, v(\mathbf{r})n(\mathbf{r}). \tag{2.28}$$

Here $T[n]$ represents the kinetic energy of the electronic system as a functional of the density, and $V_{ee}[n]$ is the electron-electron interaction functional. These terms define the Hohenberg-Kohn energy functional

$$F_{\text{HK}} \equiv T[n(\mathbf{r})] + V_{ee}[n(\mathbf{r})]. \tag{2.29}$$

Now if we consider a system of electrons with ground state density $n_1(\mathbf{r})$ and corresponding external potential $v_1(\mathbf{r})$, we can write the energy of the system as

$$E_1 = E_{\text{HK}}[n_1(\mathbf{r})] = \langle \Psi_1 | \hat{H}_1 | \Psi_1 \rangle. \tag{2.30}$$

Next we consider another density, $n_2(\mathbf{r})$, which, according to the first theorem, corresponds to a different wavefunction, Ψ_2. This state necessarily has a greater energy than E_1 since

$$E_1 = \langle \Psi_1 | \hat{H}_1 | \Psi_1 \rangle < \langle \Psi_2 | \hat{H}_1 | \Psi_2 \rangle, \tag{2.31}$$

by the first theorem. Thus for any external potential $v(\mathbf{r})$ the ground state energy is the minimum of the energy functional of Equation 2.28. Moreover, the density that minimises this energy is the ground state density. If the Hohenberg-Kohn energy functional $F_{\mathrm{HK}}[n]$ were known, then it follows that the exact ground state energy and density could be found by minimising $E_{\mathrm{HK}}[n]$ with respect to the density $n(\mathbf{r})$. In other words, the energy $E_{\mathrm{HK}}[n]$ of the electronic system is, in principle, sufficient to uniquely determine its ground state energy and density.

Despite their powerful implications, the Hohenberg-Kohn theorems offer no prescription for determining the functional $F_{\mathrm{HK}}[n]$, which is critical for any sort of practical application of the theory.

2.3.2 The Kohn-Sham Equations

The approach taken by Kohn and Sham [83] was to use the foundation of DFT laid by Hohenberg and Kohn and to apply restrictions that allow for the determination of the Hohenberg-Kohn energy functional, $F_{\mathrm{HK}}[n]$, permitting a tractable solution to the many-body Schrödinger equation (Equation 2.6). Their approach relies on an *ansatz* that assumes that the ground state charge density of the interacting many-body system is equal to that of a non-interacting auxiliary system. In such a way the complex many-body interactions can be avoided and the solution to the many-body problem is reduced to solving a set of single-electron equations.

We start by determining the form of $F_{\mathrm{HK}}[n]$ by constraining the number of electrons to N, the number of electrons in the interacting system. Recall

from Equation 2.28 that the Hohenberg-Kohn energy is given in terms of an energy functional F_{HK}. Kohn and Sham used the same approach but modified the functional F_{HK} so that the total energy of the auxiliary system can be described as $E_{\mathrm{KS}} = F_{\mathrm{KS}}$, where

$$F_{\mathrm{KS}} = \int d\mathbf{r}\, v(\mathbf{r})n(\mathbf{r}) + T_s[n(\mathbf{r})] + E_H[n(\mathbf{r})] + E_{xc}[n(\mathbf{r})], \tag{2.32}$$

where T_s is the kinetic energy of a non-interacting system with density $n(\mathbf{r})$, E_{H} is the Hartree energy, and E_{xc} is the *exchange-correlation* energy of the interacting system with density $n(\mathbf{r})$. We can expand Equation 2.32 as

$$\begin{aligned} F_{\mathrm{KS}} = \int d\mathbf{r}\, v(\mathbf{r})n(\mathbf{r}) - \sum_i \int d\mathbf{r}\, \phi_i^*(\mathbf{r}) \frac{\nabla^2}{2} \phi_i(\mathbf{r}) + \\ \frac{1}{2} \int d\mathbf{r} d\mathbf{r}' \, \frac{n(\mathbf{r})n(\mathbf{r}')}{|\mathbf{r} - \mathbf{r}'|} + E_{xc}[n(\mathbf{r})], \end{aligned} \tag{2.33}$$

where the index i runs over N. Because the Kohn-Sham system is non-interacting by definition, the density can be determined from the one-particle wavefunctions ϕ_i as

$$n(\mathbf{r}) = \sum_i |\phi_i(\mathbf{r})|^2, \tag{2.34}$$

and is identical, by construction, to the density of the interacting system. According to the second theorem of Hohenberg and Kohn, Equation 2.33 is minimised at the ground state density. We again use the variational principle and obtain the minimisation condition

$$\frac{\delta F}{\delta n} = 0. \tag{2.35}$$

In a manner analogous to Equation 2.17, we can then apply the chain rule to the functional derivative of $F[n]$ with respect to ϕ_i^* to obtain

$$\frac{\delta F}{\delta \phi_i^*} = \frac{\delta F}{\delta n}\frac{\delta n}{\delta \phi i^*} = \frac{\delta F}{\delta n}\phi_i, \tag{2.36}$$

where the last equality comes from Equation 2.34. Now applying the minimisation condition of Equation 2.35 we obtain

$$\frac{\delta F}{\delta \phi_i^*} = 0, \tag{2.37}$$

which provides the condition that the Kohn-Sham wavefunctions must satisfy. As in the Hartree-Fock approximation, we require the Kohn-Sham wavefunctions to be orthonormal such that $\langle \phi_i | \phi_j \rangle = \delta_{ij}$, which guarantees that the density is normalised to N. Using this constraint, we can minimise $F[n]$ using Lagrange multipliers, and the resulting solutions are known as the Kohn-Sham equations

$$\left[-\frac{1}{2}\nabla^2 + V_{\mathrm{H}}[n(\mathbf{r})] + v(\mathbf{r}) + V_{xc}[n(\mathbf{r})] \right] \phi_i(\mathbf{r}) = \epsilon_i \phi_i(\mathbf{r}). \tag{2.38}$$

The term V_{xc} is the exchange-correlation potential and is defined as

$$V_{xc} \equiv \frac{\delta E_{xc}[n]}{\delta n}. \tag{2.39}$$

It is often convenient to rewrite the Kohn-Sham equations as

$$\hat{H}_{\mathrm{KS}} \phi_i(\mathbf{r}) = \epsilon_i \phi_i(\mathbf{r}), \tag{2.40}$$

where $\hat{H}_{\text{KS}}$ is the Kohn-Sham Hamiltonian

$$\hat{H}_{\text{KS}} = -\frac{\nabla^2}{2} + V_{\text{KS}}. \tag{2.41}$$

The Kohn-Sham potential, V_{KS}, is defined as

$$V_{\text{KS}} = V_{\text{H}}[n(\mathbf{r})] + v(\mathbf{r}) + V_{xc}[n(\mathbf{r})]. \tag{2.42}$$

We note that, in practice, the Kohn-Sham equations (Equation 2.40) must be solved self-consistently, as we will discuss in Chapter 3.1.

2.3.3 Exchange-Correlation Functionals

By comparing the Hohenberg-Kohn and Kohn-Sham energies of Equations 2.28 and 2.32 we can express the exchange-correlation energy as

$$\begin{aligned} E_{xc}[n(\mathbf{r})] &= F_{\text{HK}}[n(\mathbf{r})] - T_s[n(\mathbf{r})] - E_{\text{H}}[n(\mathbf{r})] \\ &= T[n(\mathbf{r})] - T_s[n(\mathbf{r})] + V_{ee}[n(\mathbf{r})] - E_{\text{H}}[n(\mathbf{r})]. \end{aligned} \tag{2.43}$$

It is clear from Equation 2.43 that E_{xc} contains the difference between the interacting and non-interacting kinetic energies as well as the difference between the electron-electron interactions of the two systems. The form of E_{xc} is not known, however if it were possible to determine E_{xc} exactly then the actual ground state energy of the interacting reference system could be determined via Equation 2.40. As it stands, in order to make use of the Kohn-Sham equations we must find an approximation to the E_{xc}.

The Kohn-Sham formalism ensures that the exchange and correlation

energies are separated from the non-interacting kinetic energy and the long-range Hartree energy terms in the energy functional of Equation 2.32. This permits us to approximate E_{xc} with a local or nearly-local functional. Kohn and Sham suggested the form

$$E_{xc}[n(\mathbf{r})] = \int d\mathbf{r}\, n(\mathbf{r})\epsilon_{xc}[n(\mathbf{r})], \tag{2.44}$$

where ϵ_{xc} is the exchange-correlation energy per electron of homogeneous electron gas of density $n(\mathbf{r})$. This approximation is known as the Local Density Approximation (LDA) to DFT, and represents one of the most common forms of the exchange-correlation energy functional in use today. The function ϵ_{xc} can be separated into its constituent exchange and correlation components such that $\epsilon_{xc} = \epsilon_x + \epsilon_c$. The exchange energy per electron for a homogeneous electron gas can be calculated exactly for a charge density n as

$$\epsilon_x = \frac{E_x}{N} = -\frac{3}{4}\left(\frac{3}{\pi}\right)^{1/3} n^{1/3}. \tag{2.45}$$

Accordingly, the LDA exchange energy can be calculated exactly, using Equation 2.21, as

$$E_x^{LDA}[n(\mathbf{r})] = -\frac{3}{4}\left(\frac{3}{\pi}\right)^{1/3} \int d\mathbf{r}\, n(\mathbf{r})^{4/3}, \tag{2.46}$$

where the density n in Equation 2.45 at point $\mathbf{r}$ is set to the local density $n(\mathbf{r})$. The ϵ_c component cannot be determined analytically, however it was calculated to a very high accuracy by Ceperley and Alder [84] using quantum Monte Carlo techniques, and has been subsequently parameterised by Perdew and Zunger [85], amongst others.

Another approximation to E_{xc} is known as the Generalised Gradient Approximation (GGA). The LDA was conceived as an approximation to systems with a slowly varying density $n(\mathbf{r})$. In systems where the density varies rapidly it is not, strictly speaking, a reasonable approximation. The GGA attempts to mitigate this concern by considering the variation of the gradient of the density as well as the local density, and takes the general form

$$E_{xc}^{GGA}[n(\mathbf{r})] = \int d\mathbf{r}\, f\left[n(\mathbf{r}), \nabla n(\mathbf{r})\right]. \tag{2.47}$$

The precise form of the function $f\left[n(\mathbf{r}), \nabla n(\mathbf{r})\right]$ is beyond the scope of this thesis and the interested reader is directed to the many references available on the subject (e.g. the GGA approximation of Perdew, Burke and Ernzerhof [86]).

2.3.4 Plane Wave Basis Sets

Many problems in materials science involve periodic systems in which the external potential can be written

$$v(\mathbf{r} + \mathbf{R}) = v(\mathbf{r}), \tag{2.48}$$

where $\mathbf{R} = n_1\mathbf{a}_1 + n_2\mathbf{a}_2 + n_3\mathbf{a}_3$ is a lattice vector of the unit cell with basis vectors $\mathbf{a}_1$, $\mathbf{a}_2$, and $\mathbf{a}_3$. According to Bloch's theorem, the wavefunctions of the Kohn-Sham Hamiltonian can be represented as the product of a plane wave and a periodic function with the same periodicity as the external potential,

such that

$$\phi_{n\mathbf{k}}(\mathbf{r}) = e^{i\mathbf{k}\cdot\mathbf{r}} u_{n\mathbf{k}}(\mathbf{r}), \tag{2.49}$$

where the Bloch function, $u_{n\mathbf{k}}$, has the same periodicity as the potential such that

$$u_{n\mathbf{k}}(\mathbf{r}+\mathbf{R}) = u_{n\mathbf{k}}(\mathbf{r}). \tag{2.50}$$

The value $\mathbf{k}$ is the wave vector and when multiplied by $\hbar$ gives the crystal momentum of the electron. It is unique only up to a reciprocal lattice vector $\mathbf{G}$. The corresponding eigenvalues of the Kohn-Sham Hamiltonian are therefore periodic to within a reciprocal lattice vector $\mathbf{G}$, so that $\epsilon_n(\mathbf{k}) = \epsilon_n(\mathbf{k}+\mathbf{G})$. For a given $\mathbf{k}$ there will be a number of eigenvalue solutions to the Kohn-Sham Hamiltonian. These solutions, which are indexed by n, vary continuously with $\mathbf{k}$ and form energy bands. Because of their periodicity, only wave vectors inside the first Brillouin zone of the crystal need be considered.

The Bloch function can be expanded in a Fourier sum over the reciprocal lattice vectors $\mathbf{G}$

$$u_{n\mathbf{k}}(\mathbf{r}) = \frac{1}{\sqrt{\Omega}} \sum_{\mathbf{G}} c_{n\mathbf{k},\mathbf{G}} e^{i\mathbf{G}\cdot\mathbf{r}}, \tag{2.51}$$

where Ω is the volume of the unit cell. From Equation 2.49 the wavefunction of the Kohn-Sham Hamiltonian can then be represented using a plane wave expansion by

$$\phi_{n\mathbf{k}}(\mathbf{r}) = \frac{1}{\sqrt{\Omega}} \sum_{\mathbf{G}} c_{n\mathbf{k},\mathbf{G}} e^{i(\mathbf{k}+\mathbf{G})\cdot\mathbf{r}}. \tag{2.52}$$

The sum in Equation 2.52 is an infinite sum over the reciprocal lattice vectors. In practice, the calculation of this sum is impossible so only $\mathbf{G}$ vectors with

energy

$$\frac{1}{2}|\mathbf{k}+\mathbf{G}|^2 \leq E_{\mathrm{cutoff}} \tag{2.53}$$

are used in the expansion of Equation 2.52.

2.3.5 Pseudopotentials

The number of planewaves ($\mathbf{G}$ vectors) in a calculation is dependent on the kinetic energy cutoff imposed via Equation 2.53. One way to lower the number of planewaves, and thus facilitate calculations, is to use pseudopotentials. The core electrons of an atom are generally inert and it is only the chemically active valence electrons that participate in bonding. The pseudopotential approach eliminates the inert core electrons and groups them together with the nuclei to form rigid ions. All of the interactions between these ions and the active valence electrons are accounted for via angular-dependent pseudopotentials, which reproduce the actual potential and valence wavefunctions outside of some specified radius. As a consequence of the pseudisation of the potential, the valence electrons are described by smooth pseudowavefunctions that avoid the strong oscillations in the core region that arise in the non-pseudised (all-electron) atom due to the orthogonality of the core and valence wavefunctions. These smooth pseudo orbitals can be described by fewer planewaves than the all-electron ones and the computational intensity of DFT calculations can consequently be reduced.

We may use the methods of Hamann [87] or Troullier and Martins [88] to construct a screened pseudopotential $V_l^{\mathrm{ps,scr}}$ that acts on the pseudo valence

orbitals

$$\psi_{lm}^{\mathrm{ps}}(\mathbf{r}) = \left[\frac{\phi_l^{\mathrm{ps}}(\epsilon_l^{\mathrm{ps}}, r)}{r}\right] Y_{lm}(\Omega_{\mathbf{r}}). \tag{2.54}$$

In this equation Y_{lm} are the spherical harmonics and ϕ_l^{ps} are the angular-dependent radial orbitals, obtained (for angular momentum l) by finding the lowest eigenfunction of the non-relativistic Schrödinger equation

$$\left[-\frac{1}{2}\frac{d^2}{dr^2} + \frac{l(l+1)}{2r^2} + V_l^{\mathrm{ps,scr}}(r) - \epsilon_l^{\mathrm{ps}}\right] \phi_l^{\mathrm{ps}}(\epsilon_l^{\mathrm{ps}}, r) = 0. \tag{2.55}$$

Using the *norm-conserving* constraints we can construct the radial pseudowavefunctions ϕ_l^{ps} by using the all-electron eigenvalue for angular momentum l, ϵ_{nl} as a reference. The norm-conserving constraints are as follows:

1. The pseudowavefunction and the all electron wavefunction must correspond to the same eigenvalue

$$\epsilon_l^{\mathrm{ps}} \equiv \epsilon_{nl}. \tag{2.56}$$

   Furthermore, their logarithmic derivatives (and thus their potentials) must agree beyond a specified cutoff radius r_l^c

$$\frac{d}{dr}\ln\phi_l^{\mathrm{ps}}(\epsilon_l^{\mathrm{ps}}, r) \rightarrow \frac{d}{dr}\ln\phi_{nl}(\epsilon_{nl}, r) \quad for\ r > r_l^{\mathrm{c}}. \tag{2.57}$$

2. ϕ_l^{ps} must agree with the all electron wavefunction beyond the cutoff radius,

$$\phi_l^{\mathrm{ps}}(\epsilon_l^{ps}, r) \rightarrow \phi_{nl}(\epsilon_{nl}, r) \quad for\ r > r_l^{\mathrm{c}}, \tag{2.58}$$

and must be normalised such that

$$\int_0^\infty |\phi_l^{\rm ps}(\epsilon_l^{\rm ps}, r)|^2 dr = \int_0^\infty |\phi_{nl}(\epsilon_{nl}, r)|^2 dr = 1. \tag{2.59}$$

This leads to the norm conservation constraint,

$$\int_0^{\mathbf{r}'} |\phi_l^{\rm ps}(\epsilon_l^{\rm ps}, r)|^2 dr = \int_0^{\mathbf{r}'} |\phi_{nl}(\epsilon_{nl}, r)|^2 dr \quad for\; r \geq r_l^{\rm c}, \tag{2.60}$$

that forces the total charge densities of the pseudo and all-electron wavefunctions to be identical within the cutoff region.

3. The pseudowavefunction must have no radial nodes and must be doubly differentiable.

Having established the pseudowavefunctions, $\phi_l^{\rm ps}$, using the above norm-conserving constraints, the screened pseudopotentials $V_l^{\rm ps,scr}$ for each angular momentum l can then be determined by inverting Equation 2.55 to get

$$V_l^{\rm ps,scr}(r) = \epsilon_l^{\rm ps} - \frac{l(l+1)}{2r^2} + \frac{1}{2\phi_l^{\rm ps}(r)} \frac{d^2}{dr^2} \phi_l^{\rm ps}(r), \tag{2.61}$$

where, by construction, the pseudopotential and the all-electron potential are identical beyond the cutoff radius. In order to use the pseudopotential in poly-atomic systems, we must "unscreen" it by subtracting the Hartree and exchange-correlation contributions due to the valence electrons. The unscreened pseudopotential is then

$$V_l^{\rm ps}(r) = V_l^{\rm ps,scr}(r) - V_{\rm H}[n^{\rm ps}, r] - V_{xc}[n^{\rm ps}, r], \tag{2.62}$$

where n^{ps} is the valence electron density.

In this thesis we also employ another pseudisation scheme known as ultrasoft pseudopotentials [89], so called because their pseudowavefunctions are "softer" (i.e. smoother) than those of norm-conserving ones and therefore use fewer plane waves to achieve the same level of accuracy. As in the norm-conserving case, the pseudowavefunctions are identical to the all-electron ones outside the core. Inside the core region, however, the norm conservation constraint of Equation 2.60 is relaxed, which permits more flexibility in the construction of the pseudowavefunctions but also results in a deficit of charge. To correct this deficit, an augmentation term, localised in the core region, is added to the charge density such that

$$n(\mathbf{r}) = \sum_n \left[|\phi_n|^2 + \sum_{ij} Q_{ij}(\mathbf{r}) \langle \phi_n | \beta_j \rangle \langle \beta_i | \phi_n \rangle \right], \qquad (2.63)$$

where the Q_{ij} are the core-localised augmentation functions and the β_i are core-localised projector functions that depend on the position of the ions.

The charge augmentation functions represent the difference between the densities obtained by the all-electron and pseudo wavefunctions and are expressed as

$$Q_{ij}(\mathbf{r}) = \psi_i^*(\mathbf{r})\psi_j(\mathbf{r}) - \phi_i^*(\mathbf{r})\phi_j(\mathbf{r}), \qquad (2.64)$$

where the ψ_i are the all-electron wavefunctions and the ϕ_i are the pseudowavefunctions. The latter are constructured without being subject to the norm-conservation constraint $q_{ij}(\mathbf{r}) = 0$, where $q_{ij} = \int d\mathbf{r}\, Q_{ij}(\mathbf{r})$. The pseu-

dowavefunctions, however, are subject to an orthonormality condition

$$\langle\phi_i|S(\{\mathbf{R}_I\})|\phi_j\rangle = \delta_{ij}, \tag{2.65}$$

where S is dependent on the positions of the ions via the projector functions and is expressed as

$$S = 1 + \sum_{ij} q_{ij}|\beta_j\rangle\langle\beta_i|. \tag{2.66}$$

Ultrasoft pseudopotentials can typically result in energy cutoffs half as large as those for norm-conserving pseudopotentials and, in general, reduce the computational intensity of a DFT calculation. Due to the augmentation term, however, their implementation can be difficult and as a result they are not implemented in some DFT software package routines. For example, the hybrid functional implementation in the `Quantum ESPRESSO` software package does not permit the use of ultrasoft pseudopotentials (see Appendix A for further details).

2.3.6 Excited States

In this thesis we discuss the band gaps of materials used in organic and organic-inorganic photovoltaics and, as a consequence, we need to understand the physical meaning of the eigenvalues obtained by the DFT calculations we perform. Since knowledge of the band gap of a material requires knowledge of its conduction states, we necessarily need to involve the excited states of a given material or system. DFT, however, is a theory of ground states, as is evident from its formulation using the Hohenberg-Kohn theorems outlined in

Section 2.3.1. It is therefore not clear that excited-state eigenvalues have any meaning within the framework of DFT. Furthermore, the Kohn-Sham formulation of DFT relies on a (fictitious) auxiliary system whose only connection with the (physical) interacting system is the ground state charge density. The Kohn-Sham eigenvalues, are therefore not necessarily representative of those of the interacting system of interest. In a thesis such as this, where we attempt to relate the electronic structure of DFT model systems with their corresponding physical ones, it is absolutely vital that we first examine the meaning of DFT eigenvalues and determine how they may be connected to the actual ones.

The band gap of a N-electron system is defined as the difference between its ionisation potential (IP) and electron affinity (EA),

$$E_{\mathrm{gap}} = IP - EA, \tag{2.67}$$

where $IP = E_{N-1} - E_N$ is the removal energy of an electron from the system and $EA = E_N - E_{N+1}$ is the addition energy of an electron to the system. The IP and EA represent the HOMO and LUMO energies of the system, respectively. In Hartree-Fock theory we can connect the IP and EA of a system to its (Hartree-Fock) eigenvalues using Koopman's theorem [90]. This theorem states that the ionisation potential for a given system is equal to the negative of its highest occupied (HOMO) level. In other words, the IP is equal to the removal energy of the highest occupied electron level, such that $IP = E_{N-1} - E_N = -\epsilon_N(N)$. Here the notation E_N refers to the ground state energy of a system with N electrons, while $\epsilon_N(N)$ refers to the

eigenvalue of the Nth band of a N electron system. Koopman's theorem is only exact within the restricted Hartree-Fock formulation, which freezes the orbitals so that they do not change upon removal of an electron. Koopman's theorem can be generalised for the electron affinity with the result that the EA can be expressed as the energy of lowest unoccupied (LUMO) level [$EA = E_N - E_{N+1} = \epsilon_{N+1}(N)$].

In DFT, however, Koopman's theorem does not apply, though a similar version does exist. In the DFT-applicable theorem [91] only the HOMO energy of the system has any physical meaning and corresponds to negative of the (vertical) ionisation potential[3], $IP = -\epsilon_N(N)$. Considering this we can express the HOMO-LUMO gap of an interacting system within the DFT framework as

$$E_{\text{gap}} = \epsilon_{N+1}^{\text{DFT}}(N+1) - \epsilon_N^{\text{DFT}}(N), \tag{2.68}$$

where $\epsilon_{N+1}^{\text{DFT}}(N+1)$ is the HOMO energy of the $N+1$ electron system and $\epsilon_N^{\text{DFT}}(N)$ is the HOMO energy of the N electron system. For a non-interacting system we can also use DFT to express the band gap in terms of the Kohn-Sham eigenvalues

$$E_{\text{gap}}^{\text{DFT}} = \epsilon_{N+1}^{\text{DFT}}(N) - \epsilon_N^{\text{DFT}}(N). \tag{2.69}$$

From Equations 2.68 and 2.69 we can express the relation between the

[3]The vertical IP considers the geometric relaxation of a system upon removal of an electron. This is in contrast to the adiabatic IP assumed in Koopman's theorem where the geometry of the ionised system is identical to that of the neutral system

actual (interacting) and DFT (non-interacting) gaps as

$$E_{\text{gap}} = [\epsilon_{N+1}^{\text{DFT}}(N) - \epsilon_{N}^{\text{DFT}}(N)] + [\epsilon_{N+1}^{\text{DFT}}(N+1) - \epsilon_{N+1}^{\text{DFT}}(N)] \tag{2.70}$$

$$= E_{\text{gap}}^{\text{DFT}} + \Delta_{xc}, \tag{2.71}$$

where Δ_{xc} simply represents the difference in LUMO energies between the neutral and ionised DFT systems. The value is a measure of the non-analytic behaviour of the exchange-correlation functional and accounts for the observed difference between actual and DFT band gaps [4]. The reader is directed toward Ref. [92] for a more detailed examination of Δ_{xc} and its implications.

2.4 Hybrid Functionals

In the previous section we showed that the eigenvalues in DFT, with the exception of the HOMO, have no physical meaning and the band gaps of Kohn-Sham systems differ from the interacting ones due to a discontinuity in the exchange-correlation functional, manifested as Δ_{xc} in Equation 2.71. Thus in order to accurately calculate the open-circuit voltages of model PV systems, we need a systematic way to better describe the band gaps within a first-principles framework. The proper way to address excited states is via the *GW* approximation, a Green's function-based approach that explicitly accounts for the screening of a material upon addition or removal of an electron. For an excellent review of the *GW* approximation the reader is encouraged to consult Ref. 93. For the large interface systems considered in

[4] This difference is evident in the discussion presented in Chapter 4.

this thesis, however, calculating the band gaps using the GW approximation proves far too computationally demanding. An alternative approach is to take advantage of the fact that the exchange energy can be calculated exactly and to use hybrid functionals, which mix exact and DFT exchange energies, to arrive at a better approximation of the exchange-correlation functional.

Becke [94] notes that the exchange and correlation components of E_{xc} can be split and that, since the exchange energy dominates the correlation energy and can be calculated exactly, we can approximate the exchange-correlation energy as

$$E_{xc} = E_x^{\text{exact}} + E_c^{\text{DFT}} \tag{2.72}$$

However, as Becke explains in Ref. 94, this formulation is misleading since only treating the exchange and correlation energies together has any physical meaning. Consequently, Becke proposed a better approximation as a linear combination of the exact exchange and DFT exchange-correlation energies

$$E_{xc}^{\text{hyb}} = c_0 E_x^{\text{exact}} + c_1 E_{xc}^{\text{DFT}}. \tag{2.73}$$

The coefficients c_0 and c_1 are typically set to 1/2 (Becke's "half and half" model) or fitted to semi-empirical values. Becke later refined Equation 2.73 to the form most commonly used today (and in this thesis) [95]

$$E_{xc}^{\text{hyb}} = E_{xc}^{\text{DFT}} + \alpha(E_x^{\text{exact}} - E_x^{\text{DFT}}). \tag{2.74}$$

That is, the exchange correlation energy is rewritten as a hybrid of DFT exchange-correlation, and exact and DFT exchange energies. In this formal-

ism a fraction α of DFT exchange is subtracted from the DFT exchange-correlation energy and replaced with an equivalent amount of non-local Hartree-Fock (exact) exchange (i.e. $E_x^{\mathrm{exact}} = E_x^{\mathrm{HF}}$), with the value of α defining the type of hybrid functional used. In principle, the hybrid functional approach allows for a better "semi-empirical" description of the exchange energy of a given system while allowing the correlation energy to remain completely described at the DFT level. This, in turn, allows for a systematic improvement in the description of the band gaps of model systems, as will be demonstrated in later chapters.

Chapter 3

Considerations for Practical Calculations

3.1 Achieving Self Consistency

The Kohn-Sham equations (Equation 2.39) are functionals of the electronic density $n(\mathbf{r})$ and, accordingly, the density must be known before they can be solved. However, in Kohn-Sham DFT the density, given by Equation 2.40, depends on the Kohn-Sham wavefunctions and thus can only be determined after the Kohn-Sham equations have been solved. As a result of this situation the Kohn-Sham equations must be solved self-consistently, with an initial guess for $n_0(\mathbf{r})$ needed to start the procedure. One possible choice for the initial guess is to use the sum of the atomic densities

$$n_0(\mathbf{r}) = \sum_\alpha n_\alpha(\mathbf{r} - \mathbf{R}_\alpha), \tag{3.1}$$

where $\mathbf{R}_\alpha$ represents the position of nucleus α, while n_α is its density, for which a good choice is the pseudo-valence density. Once an initial density has been determined, we can solve Equation 2.36 to obtain the Kohn-Sham potential V_{KS}. This allows us to solve the Kohn-Sham equations (Equation 2.39) and obtain the single-particle wavefunctions ϕ_i. Once we have these wavefunctions the new density of the system, $n'(\mathbf{r})$, can be calculated using Equation 2.40. If the n' equals n_0 or is within a prescribed threshold then the self-consistent loop is complete. If not, then we must recalculate V_{KS} using a new density and repeat the cycle until self-consistency has been achieved. Intuitively we would restart the cycle by feeding n' into Equation 2.36 to obtain a new Kohn-Sham potential. In practice, however, this leads to unstable solutions so some form of linear mixing of the output density is typically used. In the simplest linear mixing scheme, a fraction of the current density, n', is mixed with the density of the previous iteration, n_i,

$$n_{i+1} = \beta n' + (1-\beta)n_i, \quad 0 \leq \beta \leq 1, \tag{3.2}$$

where n_{n+1} is the density for the proceeding step and β is the mixing parameter (typically in the range of 0.3-0.7). The calculations performed in this thesis use a modification of the linear mixing scheme known as Broyden mixing [96], which converges significantly faster.

3.2 Calculating Forces

The single-electron wavefunctions of the Kohn-Sham Hamiltonian are of course dependent on the positions of the ions of the system being examined. As such, the optimisation of the atomic structure of a system is vitally important for any sort of accurate and meaningful DFT electronic structure analysis. We typically start with an arrangement of ions and then structurally relax the system until the forces on the ions are below a specified threshold. In this thesis ions are relaxed using the Broyden-Fletcher-Goldfarb-Shanno (BFGS) algorithm, which is an iterative optimisation routine based on Newton's method. This scheme will not be discussed in any depth here and the reader is instead encouraged to consult references on numerical optimisation (e.g. Ref. 97) for further details. Intricacies of the BFGS routine aside, it is critical that we be able to calculate the forces on the ions in order to be able to properly relax a given system. Forces can be calculated in DFT via the Hellman-Feynman theorem, which states that the force on ion I, given a set of ionic coordinates $\{\mathbf{R}_I\}$, is

$$\mathbf{F}_I = -\frac{\partial E_{\mathrm{tot}}(\{\mathbf{R}_I\})}{\partial \mathbf{R}_I}. \tag{3.3}$$

Since the Kohn-Sham formulation of DFT builds upon the Born-Oppenheimer approximations (Chapter 2.2.1), the total energy E_e from a DFT calculation will not include the energy of the ions. However, because the ions are assumed fixed for a given electronic configuration, the energy of the ions can be added to that of the electrons and the total energy expression

becomes

$$E_{\text{tot}} = E_e + \frac{1}{2}\sum_{I \neq J} \frac{Z_I Z_J}{|\mathbf{R}_I - \mathbf{R}_J|}. \tag{3.4}$$

The force on ion I can then be calculated by substituting Equation 3.4 into Equation 3.3.

3.3 Pseudopotential Transferability

When generating pseudopotentials, as discussed in Chapter 2.3.5, we need to ensure that they perform well in a wide variety of systems and chemical environments. The transferability of pseudopotentials is normally assessed by comparing the lattice parameters and electronic structures of test systems with those of experiments or trusted simulations. Before these tests, however, several checks should be performed during the generation process to ensure that the transferability of a pseudopotential is good.

The scattering properties of an atom are important in determining the electronic interactions in a system. We can test how well the ionic pseudopotentials reproduce the scattering properties by examining the logarithmic derivatives of their radial wavefunctions u_l^{ps}. For a given reference energy ϵ_l^{ps} these derivatives should agree with the corresponding all-electron radial wavefunctions up until some prescribed distance outside the core radius. Ideally, the derivatives should agree over a wider range of energies, e.g. $\pm$ 1 Ha from the valence eigenvalues [98].

We must also verify that the pseudopotential reproduces the all-electron excitation or ionisation energies. To do this we take the difference between

the ground state energy and that of an excited or ionised configuration. This difference should be consistent, to within a chosen threshold, between the pseudopotential and all-electron potentials. The pseudopotentials generated for this thesis use a threshold of 1.5 mHa.

Norm-conserving pseudopotentials are "semilocal" in that they are dependent on the angular momentum l. A more computationally efficient separable form of these pseudopotentials was developed by Kleinman and Bylander [99]. The Kleinman-Bylander (KB) form separates the semilocal pseudopotential into a long-range local term and short-range fully non-local term. The conversion procedure, however, can introduce so-called ghost states, which are unphysical states at or below the valence states. The details of these ghost states will not be explored here, however they can generally be avoided by changing the local channel, l, or by increasing the core cutoff radius during pseudopotential generation.

3.4 Hybrid Functionals

In a periodic plane wave code the exact exchange E_x^{exact} in Equation 2.74 is implemented in the Hartree-Fock formalism and can be expressed as

$$E_x^{\text{HF}} = -\frac{1}{2} \sum_{\mathbf{k}n,\mathbf{k}'n'} \int d\mathbf{r} d\mathbf{r}' \frac{\phi_{\mathbf{k}n}^*(\mathbf{r})\phi_{\mathbf{k}'n'}(\mathbf{r})\phi_{\mathbf{k}'n'}^*(\mathbf{r}')\phi_{\mathbf{k}n}(\mathbf{r}')}{|\mathbf{r}-\mathbf{r}'|}, \tag{3.5}$$

where n represents the energy band index. Because the Hartree-Fock energy is a two-particle operator (i.e. the integral is over $\mathbf{r}$ and $\mathbf{r}'$), the calculation of Equation 3.5 proves to be very demanding. The computational cost can

be reduced by using an auxiliary grid of $\mathbf{q}$-points centred at the Γ-point of the Brillouin zone. The sum over $\mathbf{k}'$ in Equation 3.5 can then be limited to the subset $\mathbf{k}' = \mathbf{k} + \mathbf{q}$.

3.5 Comparing Eigenvalues from Different Calculations

In order to determine energy-level alignments it is often necessary to compare the eigenvalues of calculations performed in different computational cells. This can only be accomplished by obtaining a common reference level (i.e. potential) between the cells since the eigenvalues are only determined up to an arbitrary constant. This problem can be illustrated by examining the Hartree potential of Equation 2.12. In planewave DFT codes, the Hartree potential is expediently calculated in Fourier (reciprocal) space and is given by

$$V_{\mathrm{H}}(\mathbf{G}) = \frac{4\pi n(\mathbf{G})}{|\mathbf{G}|^2}, \tag{3.6}$$

where the $\mathbf{G}$ is a reciprocal lattice vector. This potential diverges at $\mathbf{G} = 0$ (i.e. the average of the Hartree potential). In a neutral system this divergence is not an issue since it is cancelled by divergences in the ion-ion and electron-ion interactions. To avoid this divergence the $\mathbf{G} = 0$ component of the Hartree potential is set to zero such that $V_{\mathrm{H}}(\mathbf{G} = 0) = 0$. The consequence of this choice is that, even for neutral systems, the eigenvalues are determined only up to an arbitrary constant, which will vary based on the location of the ions and the geometry of the cell (as these affect the Hartree

potential). In order to avoid this ambiguity, in supercell calculations we refer the eigenvalues to the vacuum level of the electrostatic potential (the sum of the Hartree potential and external ion potential) or, equivalently, the vacuum level of the total potential (sum of the electrostatic and exchange-correlation potentials).

3.6 Calculating Interfacial Energy-Level Alignments

The open-circuit voltage of an organic or hybrid organic-inorganic photovoltaic interface depends on its energy-level alignment. One possible way of determining this alignment would be to calculate the band structures of the separate bulk materials and align them via a common reference, for example the vacuum level of the total potential, as explained in the previous section. This approach, however, is not always suitable because it neglects the charge redistribution at the interface. We will revisit this subject in Chapter 5.

A better way of determining the interfacial energy-level alignment was proposed by Van de Walle and Martin [100] in 1987. Their method was developed for semiconductor interfaces and relies on determining the band offsets of the two materials at the interface by calculating their DFT total potentials. The first step is to perform a self-consistent DFT calculation on the interface between the two materials, after which the total potential of the system, $V(\mathbf{r})$, is calculated and then averaged along the direction normal to the interface. This is shown schematically in Figure 3.1, where, for clarity,

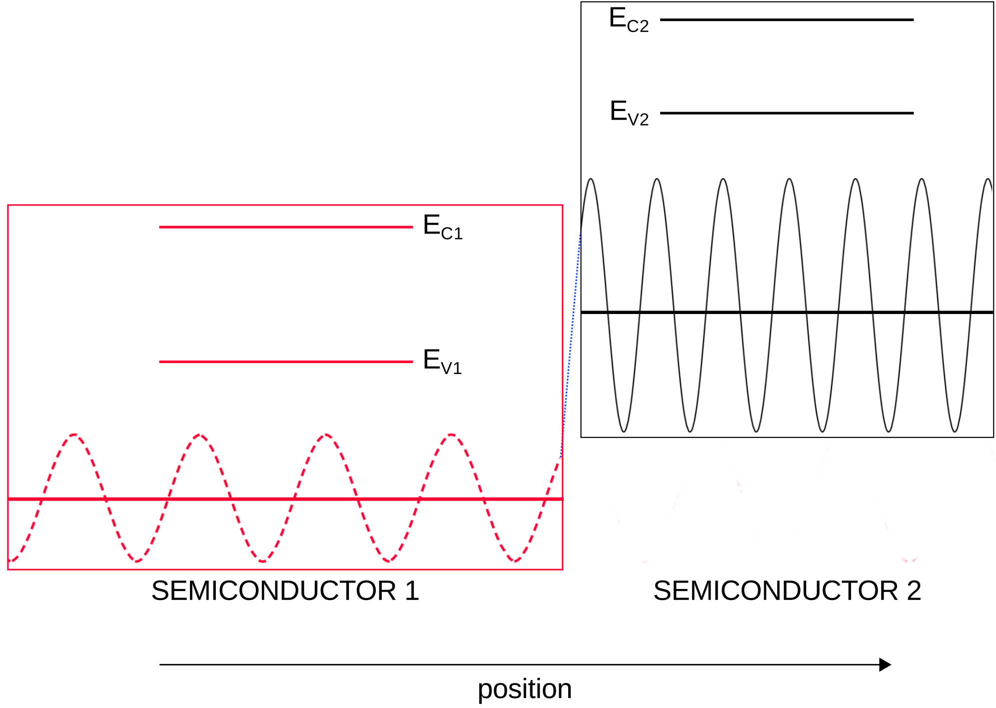

Figure 3.1: A schematic depiction of the planar averaged total potential for an interface of two semiconductors. For the sake of clarity, the portion of the potential belonging to the first material is shown by the red (dashed) curve and that of the second material is represented by the black (solid) curve. The local averages of the potential for each material are depicted by the solid horizontal lines through the curves. The bulk eigenvalues of the valence band top (E_{V}) and conduction band bottom (E_{C}) for each material are also shown and are aligned at the interface via the calculated band offset (see text).

the local values of the planar-averaged potential are shown in red (dashed) and black (solid) for the first and second semiconductor, respectively. If we take the normal direction to be z then we can express the planar-averaged total potential as

$$\bar{V}(z) = \frac{1}{\Omega} \int dxdy\, V(\mathbf{r}), \tag{3.7}$$

where Ω is the volume of the computational cell. After determining $\bar{V}(z)$, we

can take its local averages for each of the two materials, $\bar{\bar{V}}(z)$, as indicated in Figure 3.1 by the solid lines through the potential curves. The difference between these two values of $\bar{\bar{V}}(z)$ gives the potential offset at the heterojunction, which includes all of interfacial the effects, such as charge transfer (c.f. Section 3.8).

The next step is to perform self-consistent DFT calculations on each of the bulk materials separately and, for each one, determine its planar-averaged total potential $\bar{V}_{\text{bulk}}(z)$ and the corresponding $\bar{\bar{V}}_{\text{bulk}}(z)$. The eigenvalues of the band extrema - that is the top of the valence band (E_{V}) and bottom of the conduction band (E_{C}) - for each semiconductor can then be referenced to $\bar{\bar{V}}_{\text{bulk}}(z)$. Because the potential of each material at the interface returns to its bulk form after only a few layers, $\bar{V}_{\text{bulk}}(z)$ and the matching local value of $\bar{V}(z)$ are effectively identical. The bulk band structures can therefore simply be aligned via the potential offset determined at the interface, which results in the interfacial energy-level alignment (shown schematically in Figure 3.1).

We note that because DFT fails to accurately predict band gaps (c.f. Chapter 2.3.6), the alignment scheme proposed by Van de Walle and Martin will not necessarily result in interfacial band structures in agreement with experiment. This problem was addressed by Shaltaf et al. [101] using the *GW* approximation and Alkauskas et al. [102], who used hybrid functionals to correct the single-particle eigenvalues of the bulk materials. In the latter, the bulk band gaps were matched to experiment by varying the fraction α of Hartree-Fock exchange until the experimental gaps were reproduced. Once the correct bulk band structures were obtained and referenced to their respective $\bar{\bar{V}}_{\text{bulk}}(z)$ values, the interfacial energy-level alignment was calculated

by applying the interfacial band offset determined by the Van de Walle and Martin procedure described above.

The technique described in this section represents an elegant and powerful method to determine interfacial energy-level alignments via DFT calculations on the interface and hybrid-functional calculations on the bulk materials. It is used throughout this thesis and its application to the PV systems studied in this thesis is developed further in Chapter 5.

3.7 Dipole Corrections

In DFT codes that use planewave basis sets, calculations are performed in computational cells that are periodic in all three directions. When studying PV interfaces we deal with systems with a slab composed of two materials that is periodic only in the plane parallel to the surface. To avoid interactions with periodic replicas normal to the interface we must allow for empty space (vacuum) in the unit cell such that the repeating slabs are sufficiently separated from one another.

Since the PV slabs examined in this thesis are composed of two materials they are necessarily asymmetric with respect to their top and bottom surfaces. The electrostatic potentials at the top and bottom of the computational cell are therefore unequal. Planewave DFT codes, however, impose periodic potential restrictions on the unit cell so an additional, artificial electric field arises in order to avoid the discontinuity of the potential at the cell boundaries. The additional electric field poses a problem in this study because it artificially slopes the potential profile of a system and complicates

the accurate determination of a reference vacuum level.

Bengtsson [103] introduced a ramp-shaped dipole correction that can be incorporated in a standard DFT code and that cancels the artificial electric field. The corresponding potential associated with the dipole correction is expressed as

$$V_{dip}(z) = 4\pi m \left(\frac{z}{z_m} - \frac{1}{2} \right), \tag{3.8}$$

where z_m is the height of the computational cell (normal to the interface) and m is the surface dipole density of the slab

$$m = \int_{-\infty}^{\infty} dz' \, \bar{n}(z') z'. \tag{3.9}$$

In Equation 3.9 $\bar{n}$ represents the planar-averaged charge density in the direction perpendicular to the interface. In practice the ramp-shape correction is constructed so that the step in the potential occurs in the vacuum region of the cell and does not affect the potential across the slab.

An example of the Bengtsson correction scheme is shown in Figure 3.2 for a computational cell involving graphene functionalised with epoxide (-C-O-C-) groups, which are discussed in more detail in Chapter 7. Figure 3.2 clearly shows that the dipole correction removes the slope in the averaged potential that is introduced by the artificial electric field. The dipole step is added in the middle of the vacuum region of the cell. Application of the Bengtsson dipole correction removes the slope in the potential and creates two well-defined vacuum levels on either side of the potential step.

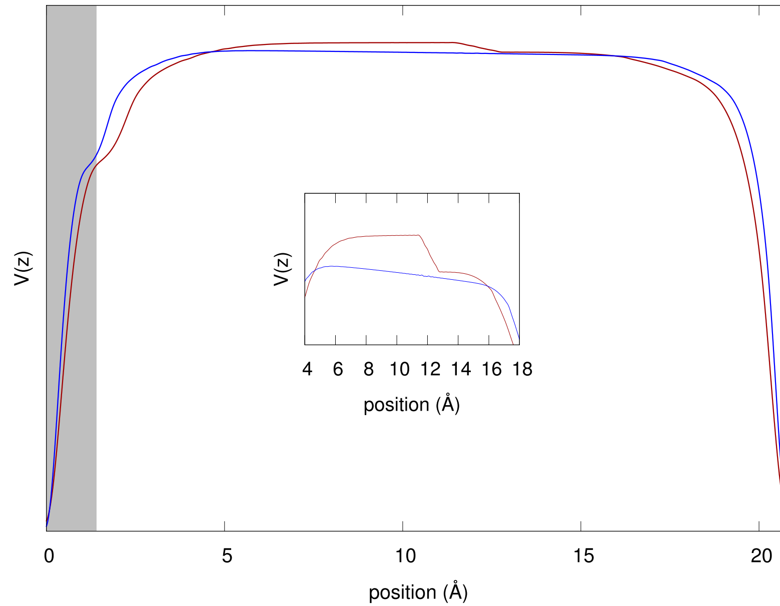

Figure 3.2: A Bengtsson-style dipole correction applied to functionalised graphene. The blue curve shows the uncorrected planar-averaged total potential of the unit cell along the interface. The red curve shows the dipole-corrected potential, with the potential step introduced in the vacuum region of the cell. Examination of the red (corrected) potential shows that the slope in the blue (uncorrected) curve due to the asymmetric slab dipole is removed and two well-defined vacuum regions are recovered on either side of the potential step. The shaded regions of the plot correspond to the position of the functionalised graphene layer. The inset shows a magnified view of the vacuum region in order to better illustrate the slope of the uncorrected curve and the potential step of the corrected curve.

3.8 Charge Neutrality Level

We mentioned in Section 3.6 that the formation of the interface between two semiconductors can lead to charge transfer from one material to the other. This process can affect the interfacial energy-level alignment and is completely neglected when determining the band lineup via the electron affinity rule (Chapter 1.3.2), where bulk band structures are aligned via their vacuum levels. When attempting to determine the open-circuit voltage of an interface

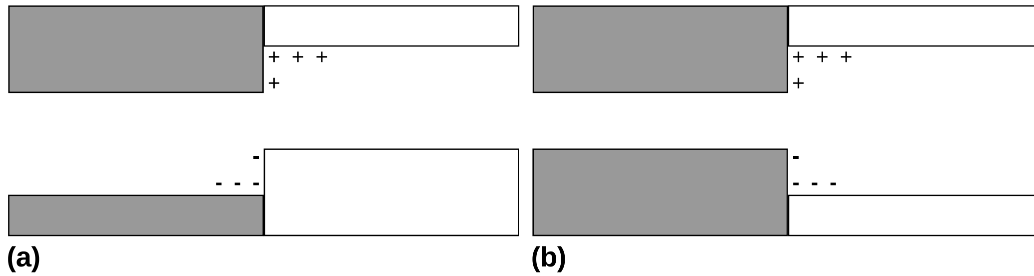

Figure 3.3: Schematic diagrams depicting the interfacial dipole at a (a) Type II and (b) Type I interface. In (a) we see the net accumulation ("+") and deficit ("-") of charge brought about by the presence of mid-gap states in semiconductors. In order to reduce the dipole, charge is transferred from the valence band manifold of the white semiconductor to the gap states in the grey semiconductor, driving the CNLs of the semiconductors together. The situation in (b) is similar and the interface dipole is reduced as charge transfers from the valence manifold of the black semiconductor to the gap states of the white semiconductor. After Ref. 104.

it is important to understand how the charge transfer affects the energy-level alignment between the two materials forming the heterojunction. In 1984 Tersoff [104] proposed a theory describing the alignment of the energy bands at the interface of two semiconducting materials. Central to his idea is the generation of an interfacial dipole that is associated with the semiconductor gap states induced by band offsets at the heterojunction. This concept is depicted schematically in Figure 3.3. The dipole depends on the band offset at the interface and acts to drive the band alignment to a value that would give no dipole, also known as the charge neutrality level (CNL).

Tersoff contends that the interface induces states in the band gaps of one or both of the semiconductors. The presence of these induced states, analogous to the metal-induced gap states (MIGS) introduced by Heine [105] and Tersoff [106], generates an interfacial dipole due to the resulting charge imbalance across the heterojunction.

The charge neutrality level (CNL) of a semiconductor is the position of the Fermi level that leaves the surface without a net charge. In other words, charge neutrality occurs when the valence band is completely filled. The interface-induced gap states have a character that varies from valence-like (near the valence band top) to conduction-like (near the conduction band bottom). The point at which the sign of the character flips is known as the "branch point". If the valence-like gap states are not filled then there is a local deficit of charge, which generates a dipole across the interface. To counteract the generated dipole, charge is transferred across the interface in such a way as to fill the valence-like gap states and bring the CNLs of the two semiconductors together (see Figure 3.3). The band structures of real semiconductors are complicated so, in practice, determining the zero-dipole lineup condition is both difficult and dependent on the materials involved. A reasonable estimate of the energy band lineup that leads to charge neutrality is to align the branch points of the two materials. The branch point can be determined analytically using Green's functions methods but is not explored in any further detail in this report. The interested reader is encouraged to read Ref. 104 for additional information.

The concept of the interfacial dipole and the charge neutrality level are critical to the understanding of energy-level alignments at photovoltaic interfaces. In Chapters 5, 6, and 7 we will see how the presence of a dipole can dramatically affect the open-circuit voltage and band alignment of a PV interface and why, as a result, the EA rule can be insufficient for describing the energy-level alignment of organic and hybrid organic-inorganic photovoltaic interfaces.

3.9 Overview of Experimental Techniques

This section provides a brief overview of some of the experimental techniques that are mentioned or referenced in this thesis. Since the detailed physics underpinning each of these techniques is not crucial for this thesis, our intention here is only to familiarise the reader with the fundamental concepts of each technique.

The *scanning electron microscope* (SEM) [107] is an electron microscope that employs a focused beam of electrons to scan a sample and form an image. The electron beam interacts with the sample in a way that can be detected and interpreted to provide topographic and compositional information. The resolution of SEM images can be upwards of 1 nm. *Transmission electron microscopy* (TEM) [108] is a technique in which a beam of electron is transmitted through a very thin sample. An image is produced by the interaction and interference of the electron beam with the sample, and is captured, magnified and focused onto a screen, film or electronic sensor. Both SEM and TEM are used for the imaging of PV interfaces and represent a critical experimental tool for understanding the nanoscale structure of organic and hybrid organic-inorganic interfaces.

Photoluminescence (PL) spectroscopy [109] is the measure of light emission from a sample upon absorption of a photon. In PL experiments, a sample will be excited by a photon and the intensity of the emission spectrum is measured over time. In semiconductors we expect to observe a high PL intensity as excited electrons relax to the ground state and emit photons. Any deviation from this PL behaviour indicates the presence of a

non-radiative pathway for charge, such as trap states or charge transfer to another materials.

Chapter 4

Materials for Organic and Hybrid Organic-Inorganic Photovoltaic Devices

Before exploring the physics of the ZnO/P3HT, GaAs/P3HT and graphene/P3HT PV interfaces, it is important to first examine the constituent materials in their bulk or crystalline forms. In this chapter we examine both the atomic and electronic structures for each of bulk ZnO, GaAs, graphene, and P3HT at the DFT level. Unless otherwise noted, all structural relaxations were performed using the LDA, while electronic structure calculations were performed using the GGA. To preserve the clarity of the discussion, most of the computational details are left to Appendix A.

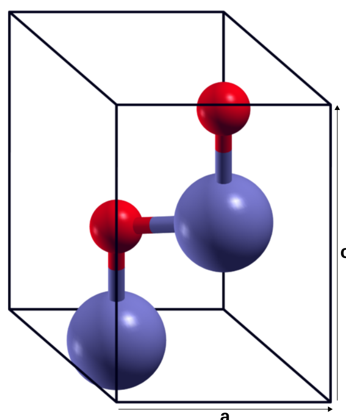

Figure 4.1: The unit cell of bulk ZnO features two Zn (blue) and two O (red) atoms.

4.1 Zinc Oxide

At ambient conditions, bulk zinc oxide (ZnO) crystallises in the wurtzite structure. Starting from an ideal wurtzite structure we relaxed the bulk unit cell of ZnO and obtained the optimised DFT lattice parameters shown in Table 4.1. The calculated parameters are in excellent agreement with other first-principles studies and experimental measurements. The optimised unit cell of bulk wurtzite ZnO is shown in Figure 4.1.

The electronic band structure of bulk wurtzite ZnO is shown in Figure

	a [Å]	c [Å]	c/a
LDA (this work)	3.186	5.154	1.618
LDA [110]	3.193	5.163	1.617
LDA [111]	3.23	5.168	1.60
LDA [112]	3.159	5.062	1.6024
LDA [113]	3.1959	5.1585	1.6141
Expt [111]	3.247-3.253	5.201-5.220	1.5988-1.6076*

Table 4.1: Lattice parameters of bulk ZnO (* estimated from data presented in paper).

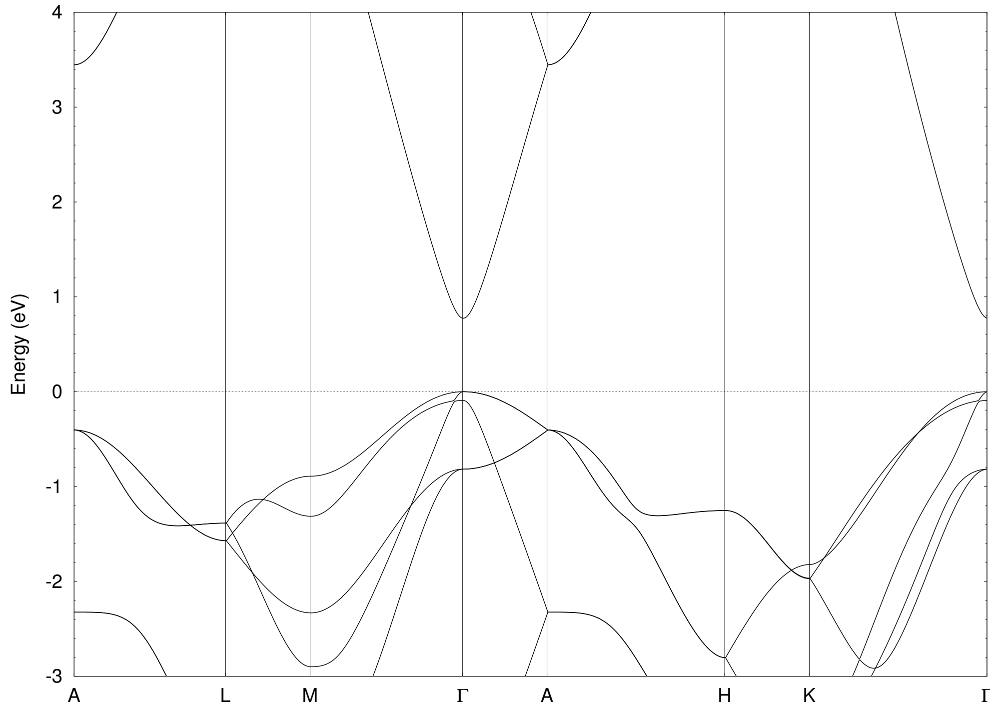

Figure 4.2: DFT band structure of bulk wurtzite ZnO. The Kohn-Sham band gap of 0.84 eV is direct and is located at Γ.

4.2 and displays a direct band gap at the Γ point of the Brillouin zone. The DFT band gap of bulk ZnO is 0.84 eV and is in good agreement with other first-principles studies [111, 112]. This band gap significantly underestimates the experimental band gap (3.4 eV [114]), as expected based on the discussion presented in Chapter 2.3.6. A recent *GW* study has claimed a band gap of ∼3.6 eV for bulk ZnO [115], however this result may be due to unconverged calculations and may depend strongly on the choice of *GW* implementation used to perform the calculations [116]. In our calculations the ZnO conduction band exhibits Zn 4s and O 2p character.

In calculations involving interfaces, the bulk crystal must be terminated along a certain direction in order create a surface. Here we use the non-polar

	$\Delta_{\mathrm{Zn-O}}$ [Å]	θ [°]	C_B [%]
LDA (this work)	0.3262	10.3	-6.5
LDA [110]	0.338*	10.7	-6.7
LDA [113]	0.28	~8.8*	-7.6
expt [118]	0.4 (±0.20)	12±5	-3±6

Table 4.2: Surface reconstruction of the $(10\bar{1}0)$ ZnO surface when compared to the bulk. Data include the difference in the vertical (y-direction) positions of the Zn and O surface atoms (Δ_{Zn-O}), the tilt of the Zn–O surface dimer from the horizontal (θ) and the bond-length contraction of the Zn–O surface dimer (C_B) (* estimated from data presented in paper).

$(10\bar{1}0)$ surface termination as it is the most energetically favourable [117] and is commonly found in ZnO/P3HT hexagonal nanowire devices (as will be discussed in Chapter 5).

Due to the periodic boundary conditions, a finite ZnO slab (in the direction normal to the interface) is used in the calculations presented in Chapter 5. This slab is composed of $5 \times 3 \times 4$ bulk unit cells along the $[1\bar{2}10]$, [0001], and $[1\bar{0}10]$ directions, respectively. The reasons for the choice of these dimensions is described further in Chapter 5.

The final structure of the slab is shown in Figure 4.3. The $(10\bar{1}0)$ surface reconstruction of the slab matches well with other first-principles and experimental results. As shown in Table 4.2, the bond lengths and angles of the surface Zn-O dimers are in good agreement with the data available in the literature. This agreement demonstrates the ability of DFT (in the LDA) to adequately describe the non-polar wurtzite $(10\bar{1}0)$ surface for ZnO. The relaxation of the surface dimers give a direct indication of the covalency or ionicity of the Zn-O bonds and, in the present case, indicate that the chemical bonds in ZnO are highly ionic but with significant covalent contributions

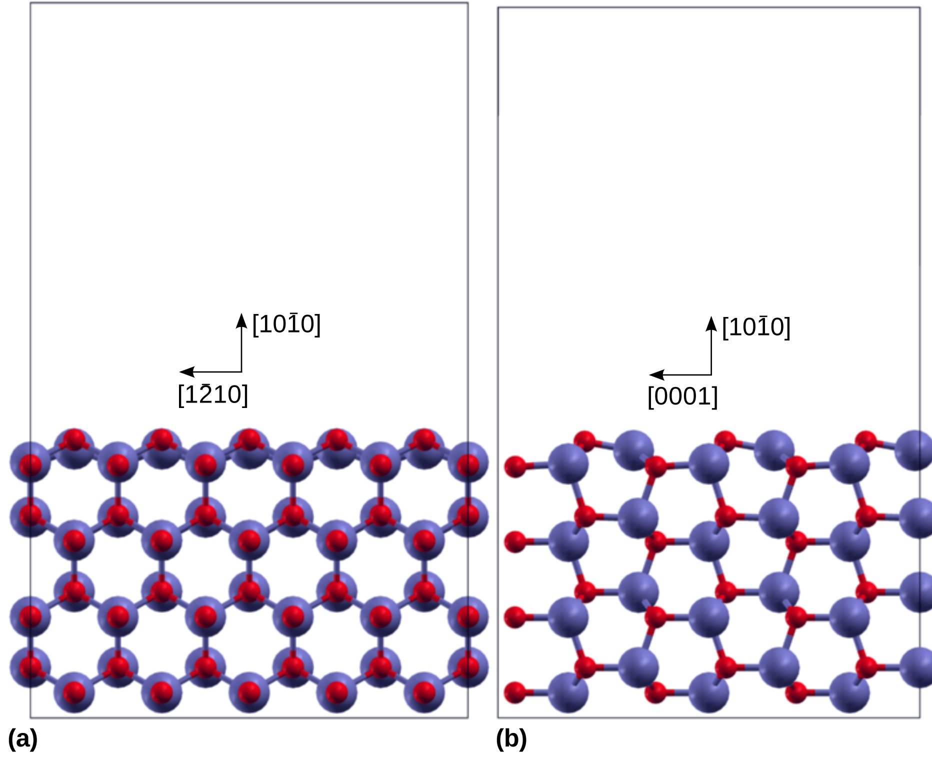

Figure 4.3: The rectangular ZnO slab model made of 5 × 3 × 4 unit cells in the [1$\bar{2}$10], [0001], and [1$\bar{0}$10] directions, respectively. The model is periodic along the [1$\bar{2}$10] and [0001] directions and is separated by over 10 Å from its periodic images in the [1$\bar{0}$10] direction. The slab includes 240 atoms in total and has a transverse area of 15.93 × 15.46 Å^2.

[110]. This observation is important because it helps to describe the nature of the reconstruction of the (10$\bar{1}$0) surface and its non-polarity. At the surface the coordination of each Zn and O atoms is reduced from four-fold to three-fold, which results in an unoccupied dangling bond for Zn and an occupied dangling bond for O. The covalent nature of the bonding results in a rehybridisation of the surface Zn atom from sp^3 to sp^2, causing a strong shift downward toward the O atoms of the underlying layer [see Figure 4.3(b)] and a tilt in the surface dimer. The ionic nature of the bonding results in the Zn and O surface atoms moving closer to the bulk, in order to achieve stronger

screening, and a reduction of the surface dimer bond lengths with respect to the bulk values.

4.2 Gallium Arsenide

In this thesis gallium arsenide (GaAs) is examined in its wurtzite form and when dealing with slabs, as in Chapter 6, we consider exclusively the $(10\bar{1}0)$ surface termination. Despite crystallising only in the zinc blende polymorph in bulk and thin film forms [119], GaAs has been shown to exist in the wurtzite phase (in conjunction with zinc blende) when grown as nanowires [120]. The use of GaAs in the wurtzite form in this thesis is rationalised by noting that the GaAs/P3HT PV devices considered in this thesis are based on GaAs nanowires, and by recognising that the work already performed in the study of wurtzite ZnO can be directly applied to the examination of GaAs if the wurtzite phase is assumed.

The optimised bulk crystal of wurtzite GaAs is shown in Figure 4.4. The bulk lattice parameters shown in Table 4.3 are in very good agreement with experimental results, indicating that the LDA is adequate for structural calculations involving GaAs.

Hybrid functionals are not used in the calculations involving GaAs/P3HT interfaces in Chapter 6 since we do not attempt to determine the interfacial

	a [Å]	c [Å]	c/a
LDA (this work)	3.991	6.580	1.649
expt [120]	3.98	6.56	1.65

Table 4.3: Lattice parameters of bulk wurtzite GaAs.

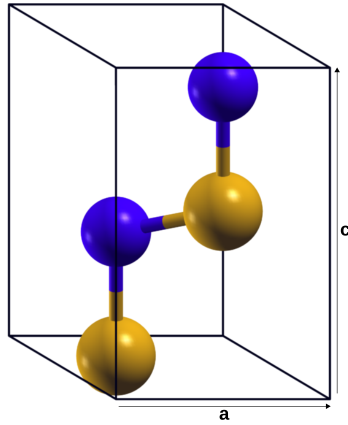

Figure 4.4: Unit cell of the bulk GaAs model. Atomic color code: Ga (gold), As (violet).

energy-level alignment. As a result, in this chapter we use ultrasoft LDA pseudopotentials for the electronic structure calculations involving GaAs. We find a DFT band gap of 0.30 eV, which is lower than the experimental gap of 1.46 eV [121] but in good agreement with other first-principles calculations [122]. The band structure of bulk wurtzite GaAs is shown in Figure 4.5 and matches well with the first-principles band structure presented in Ref. 122. The band structure of Figure 4.5 shows a direct band gap located at the Γ point of the Brillouin zone.

In Chapter 6 we explore GaAs/P3HT interfaces using both pristine (unoxidised) and oxidised GaAs slabs. These slabs terminate on the $(10\bar{1}0)$ surface and have a transverse area of 15.96×13.16 Å in the $[1\bar{2}10]$ and [0001] directions, respectively. The optimised pristine slab is shown in Figure 4.6, while the optimised oxidised slab is shown in Figure 4.7. Oxidation of the GaAs surface by a single layer of oxygen as been shown for the zinc blende (110) surface of GaAs [123, 124]. In our oxidised interface model we construct an O-monolayer following Refs. 123 and 124 on the surface of the wurtzite $(10\bar{1}0)$

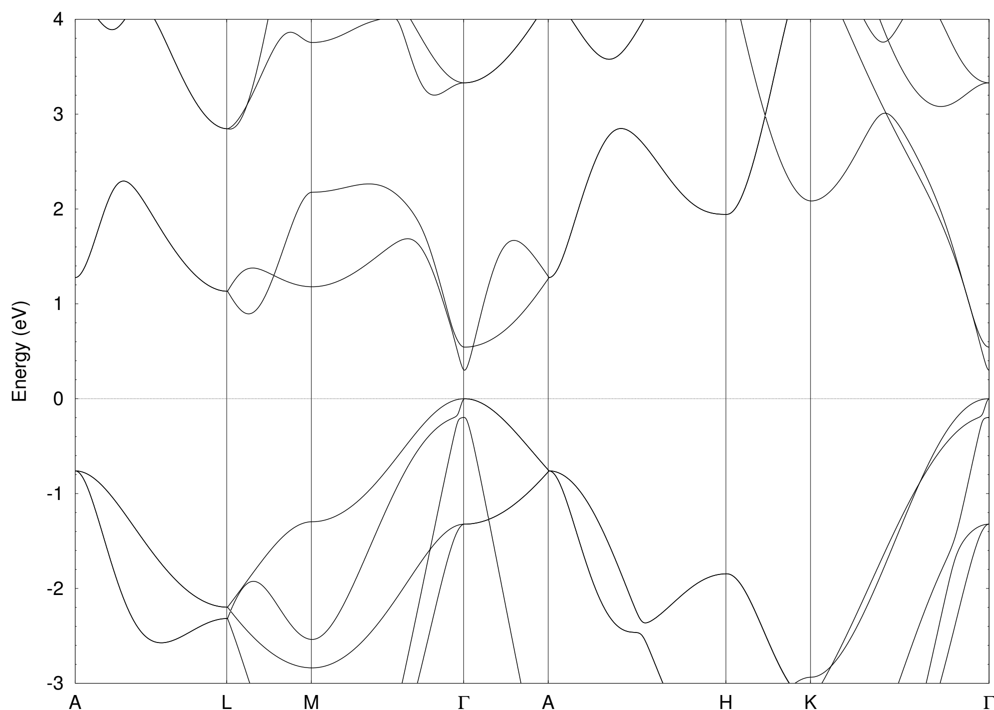

Figure 4.5: The band structure of bulk wurtzite GaAs. A direct band gap of 0.30 eV is found at the Γ point of the Brillouin zone.

GaAs slab. This approach can be justified since the surface reconstructions of pristine zinc blende (110) GaAs and pristine wurtzite $(10\bar{1}0)$ GaAs are very similar. Furthermore, the reconstruction of the oxidised surface in Figure 4.7 demonstrates a configuration very similar to the oxidised zinc blende (110) GaAs surfaces of Refs. 123 and 124. In this reconstruction the O atoms form a bridge between the Ga and As atoms of adjacent surface dimers along the [0001] direction, resulting in a trench directly beneath the location of the surface dimers in the pristine slab. Given the similarities of the unreconstructed zinc blende (110) and wurtzite $(10\bar{1}0)$ surfaces of GaAs, and the similarities of their reconstructed surfaces after oxidation, we can conclude that it is reasonable to tentatively use a zinc blende-type oxidation scheme for the

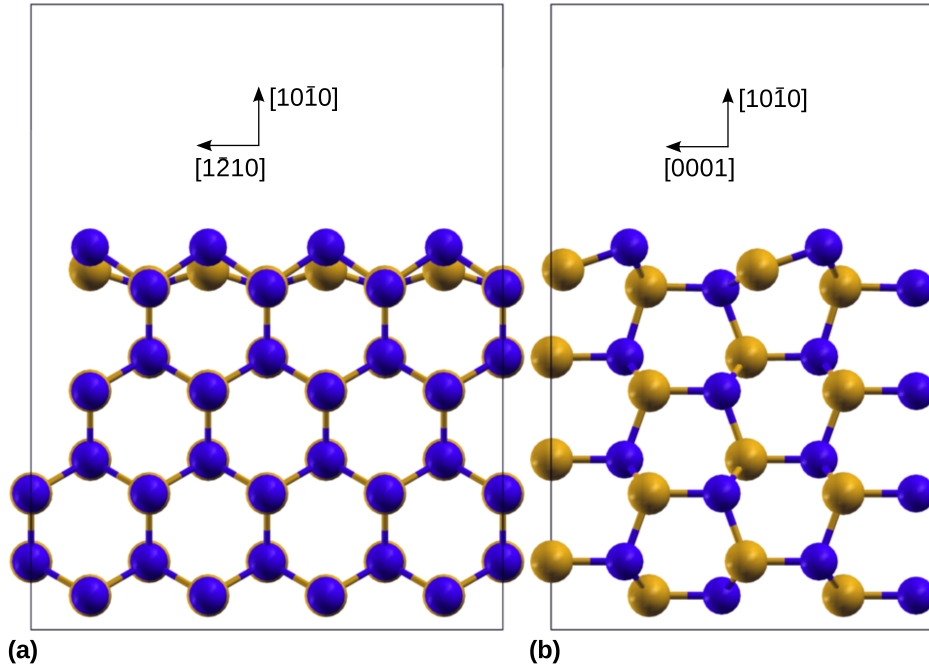

Figure 4.6: Unit cell of the pristine GaAs slab model. Atomic colour code: Ga (gold), As (violet).

wurtzite surface, and that the LDA is suitable for accurately determining the reconstructed surface of oxidised and pristine GaAs slabs. It is important to note that the oxidation model chosen for our oxidised interface is only one of several plausible choices. However, because we are primarily interested in the qualitative comparison between the pristine and oxidised GaAs/P3HT interfaces in Chapter 6, we feel that our choice of model is suitable for the purposes of this thesis.

4.3 Graphene

Graphene is a two-dimensional monolayer of C atoms arranged in a hexagonal honeycomb lattice [125], and can be thought of as the building block

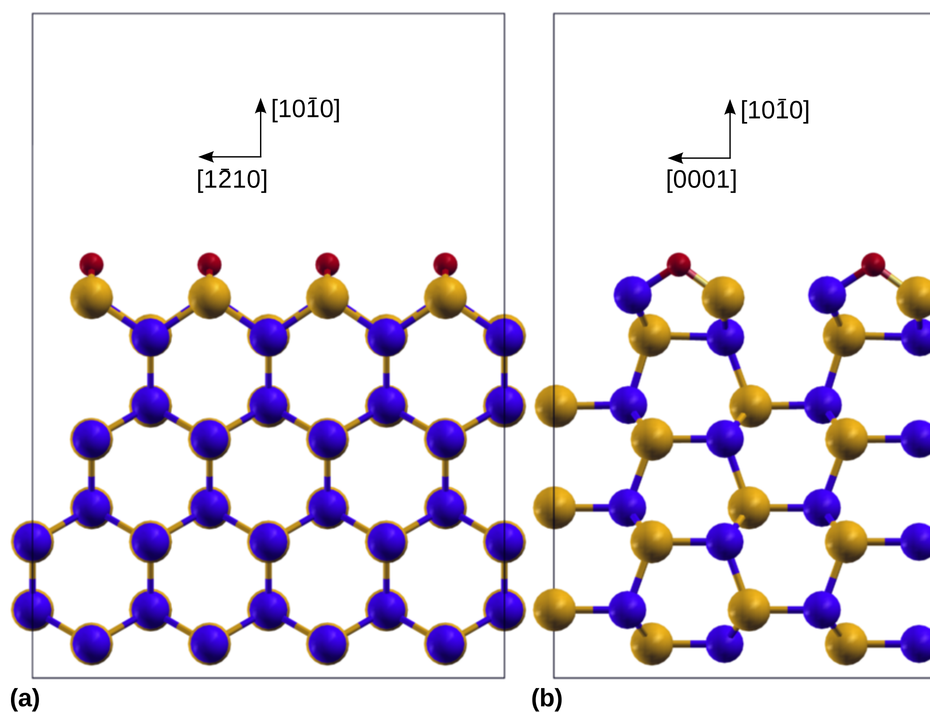

Figure 4.7: Unit cell of the oxidised GaAs slab model. Atomic color code: Ga (gold), As (violet), O (red).

of graphite. Each C atom in graphene is sp^2 hybridised to allow for bonding with its three neighbours. Graphene has seen a tremendous rise in its popularity in recent years largely due to its extremely high electron mobility [125, 126].

Graphene is studied in Chapter 7 in conjunction with P3HT as an acceptor material for organic PV. Here we examine the suitability of DFT to describe the electronic structure of ideal graphene, shown in Figure 4.8. Because we are only interested in the electronic structure, we do not perform an atomic structure relaxation and instead use the ideal two-atom hexagonal unit cell for graphene, with a C-C bond length of 1.42 Å [127]. Since hybrid functionals are used to describe the electronic structure of the

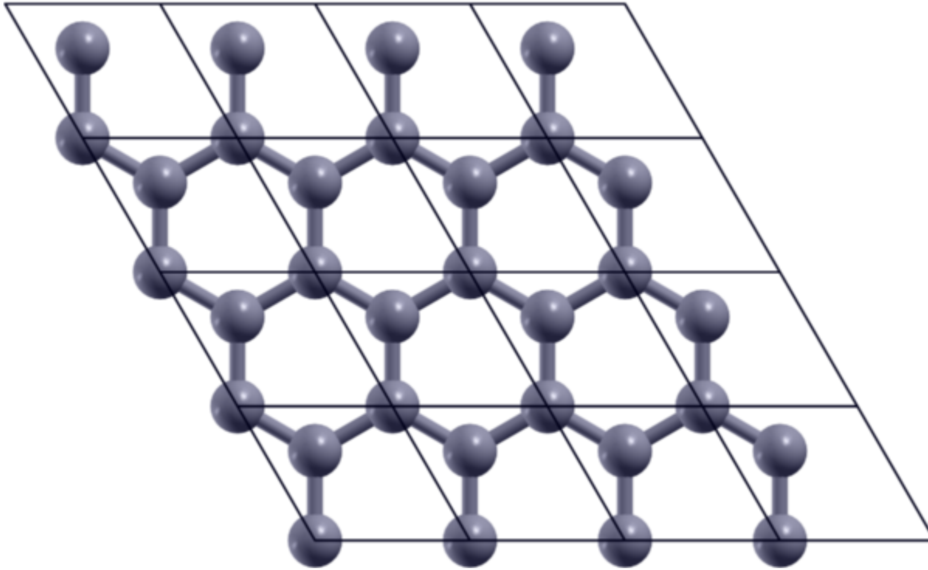

Figure 4.8: Multiple unit cells of a single sheet of ideal graphene with the crystallographic axes parallel to the page.

graphene/P3HT interface, here we use GGA (within the PBE formulation) to examine the electronic structure of graphene. The band structure is shown in Figure 4.9 and demonstrates the correct behaviour at the K (Dirac) point of the Brillouin zone. This indicates that our GGA C pseudopotentials are capable of properly describing the electronic structure properties of graphene. Further verification is obtained by examining the density of states (DOS) for ideal graphene around the Fermi level. The DOS is shown in Figure 4.10 and we note the zero density of states at the Fermi level (Dirac point), as expected.

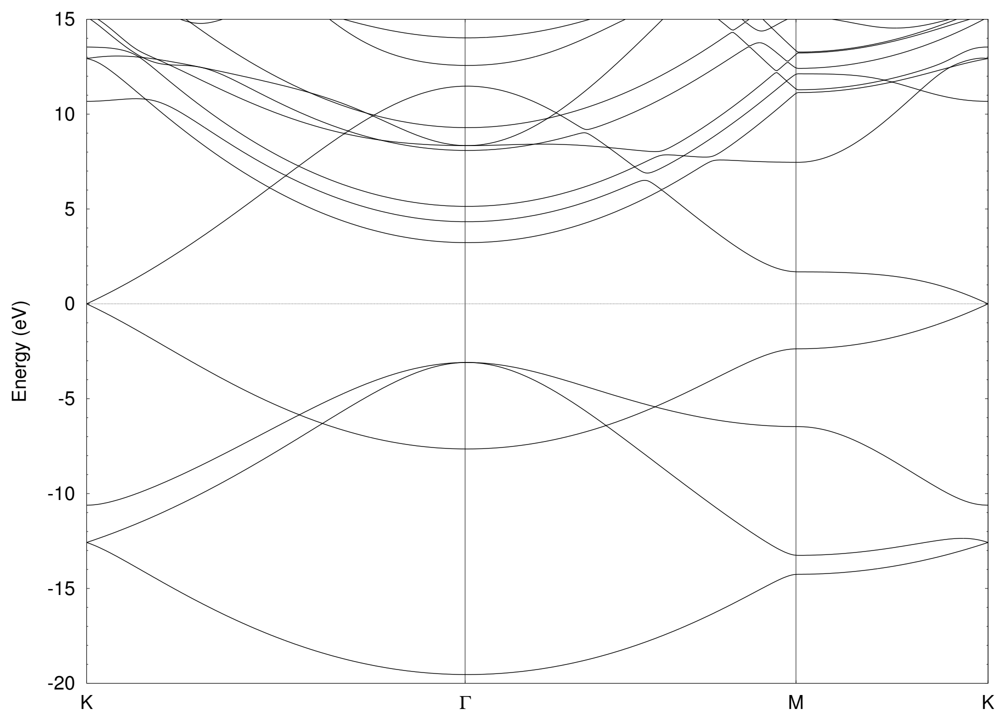

Figure 4.9: Band structure of ideal graphene.

4.4 Poly(3-hexylthiophene)

Poly(3-hexylthiophene) (P3HT) is a thiophene-derived conjugated polymer with chemical structure shown in Figure 4.11(a). The alkyl side-chains have chemical formula C_6H_{13} and are attached alternately at the 3 and 3′ positions of the thiophene monomers. The thiophene monomers are connected to their neighbours at either the 2- or 5-positions, the choice of which defines three possible couplings between adjacent rings: head-to-tail (HT) at 2,5′, head-to-head (HH) at 2,2′, and tail-to-tail at 5,5′. In this thesis we exclusively examine HT coupling with parallel P3HT sheets (along the **b**-axis) stacked in an A-A manner. This choice is driven by the conformation of the polymer at the various interfaces described in Chapters 5, 6, 7. The justifications for

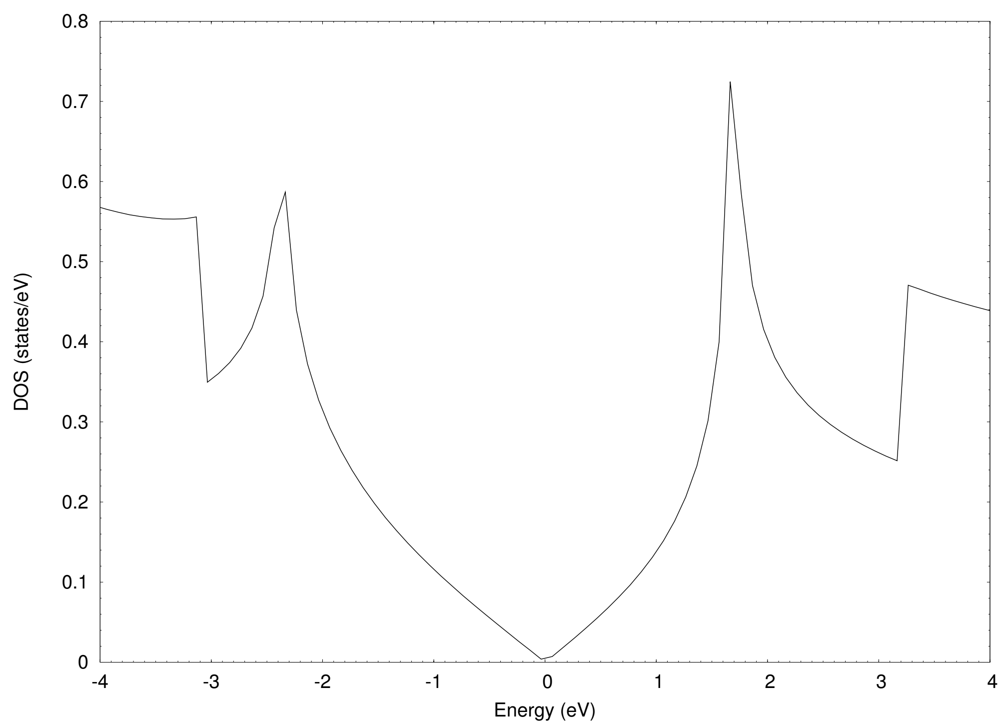

Figure 4.10: Density of states for ideal graphene. The Dirac point, which coincides with the Fermi level, is set to the zero of the energy axis.

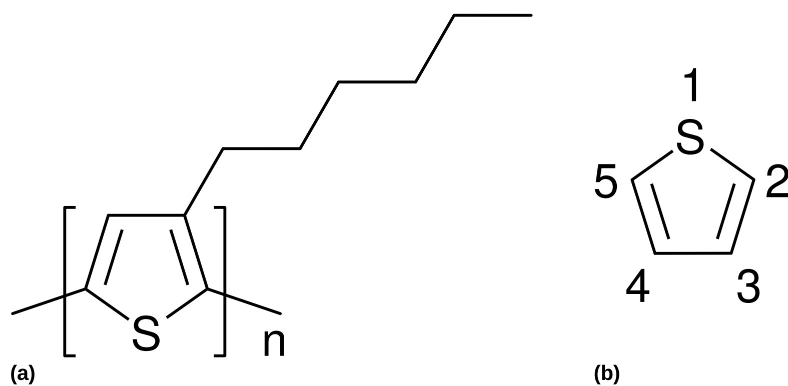

Figure 4.11: The chemical structure of P3HT (a), consisting of a polythiophene backbone (alternating thiophene rings) with alkyl side-chains attached at the 3 position of the thiophene rings. The chemical structure of a thiophene ring, with the atom numbers labelled, is shown in (b).

the chosen P3HT morphologies at each of these interfaces are left to their respective chapters.

The optimised structure of P3HT at the DFT level depends heavily on the initial configuration used for the structural relaxation. This is a direct result of the existence of many local energy minima in the morphological energy landscape of the polymer. In order to explore this energy landscape, P3HT was structurally optimised using three initial packing configurations along the alkyl chain axis. The degree of side chain packing varied the amount of side chain interdigitation from none (Configuration I), to half (Configuration II), to full (Configuration III). These three configurations were then structurally relaxed, leading to the configurations shown in Figures 4.12, 4.13, and 4.14. We note that in all three configurations the polythiophene backbone runs along the **c**-axis while the alkyl side-chains run along the **d**-axis. The stacking direction is along the **b**-axis, which is the direction of $\pi-\pi$ interaction amongst the P3HT sheets. The choice to use only three initial configurations was made in order to mimimise the computational effort while allowing a representative range of optimised structures to develop.

The optimised lattice parameters of the three configurations are listed in Table 4.4, along with results from other first-principles and experimental studies. We see from the results presented in Table 4.4 that our calculated lattice parameters are well within the range of values obtained experimentally, and also agree well with other DFT values.

Further verification of the DFT-level structural optimisations can be obtained by comparing the bond lengths and angles of the thiophene rings with the experimental values. This comparison is shown in Table 4.5 between Con-

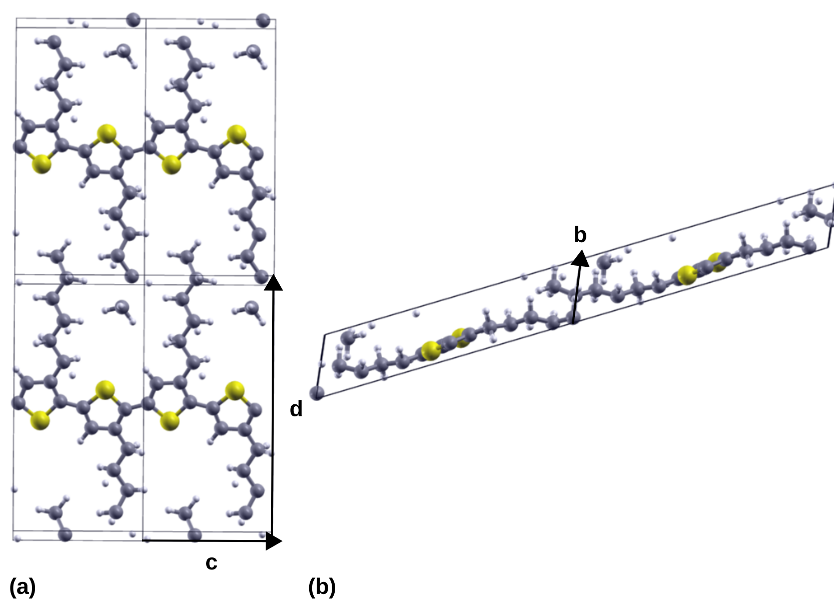

Figure 4.12: The optimised configuration of Configuration I, as viewed from (a) the **cd** and (b) **bd** planes. The unit cell is made up of two thiophene monomers and contains 50 atoms.

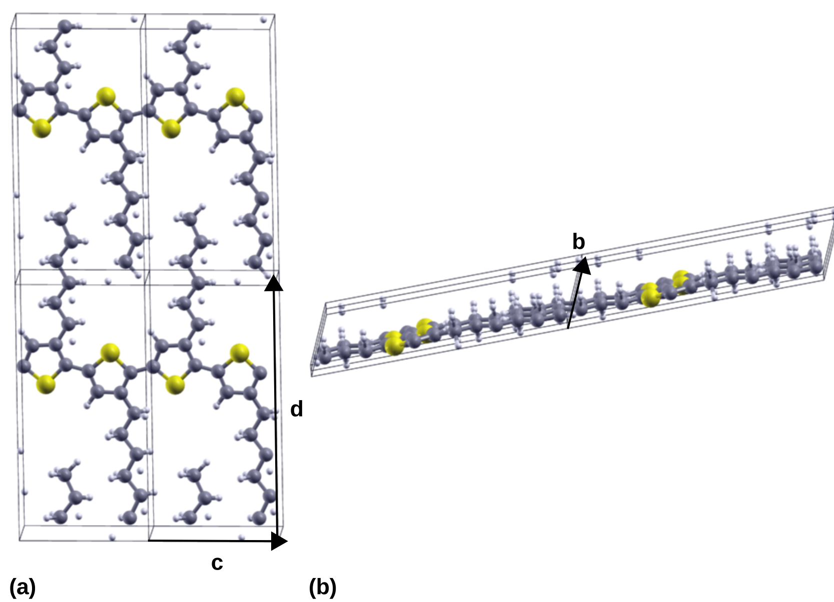

Figure 4.13: The optimised configuration of Configuration II, as viewed from (a) the **cd** and (b) **bd** planes. The unit cell is made up of two thiophene monomers and contains 50 atoms.

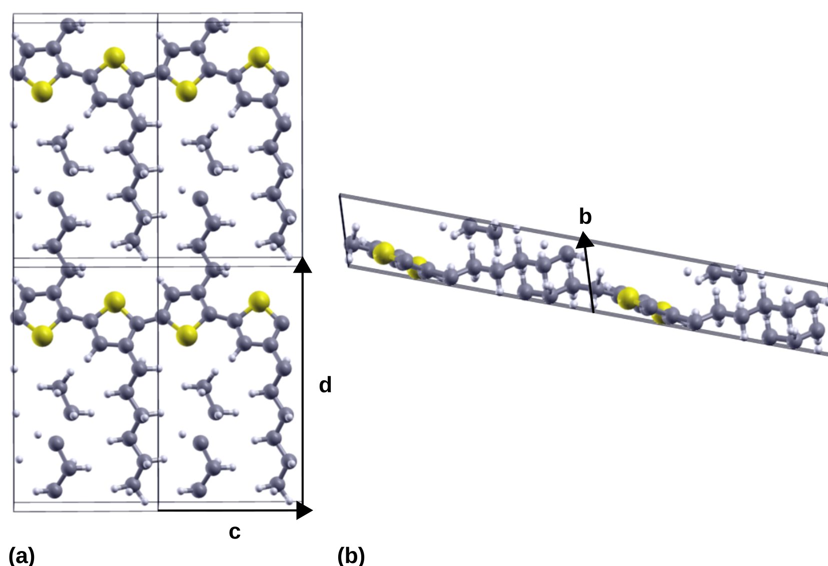

Figure 4.14: The optimised configuration of Configuration III, as viewed from (a) the **cd** and (b) **bd** planes. The unit cell is made up of two thiophene monomers and contains 50 atoms.

figuration I and other first-principles and experimental values. The chemical structure and atom numbers of a thiophene ring are shown in Figure 4.4(b). All values are within a reasonable range of the calculated and experimental data, further demonstrating the suitability of the LDA for structural optimisations involving P3HT.

The electronic structure of P3HT was examined via band structure plots for Configs. I, II, and III, as shown in Figure 4.15. The band structure plots go through the paths along the **c**-, **b**-, and **d**-axes. The high symmetry points include Γ (0,0,0), Z($\frac{\pi}{c}$,0,0), Y(0,$\frac{\pi}{b}$,0), and B(0,0,$\frac{\pi}{d}$) We observe a very similar band structure for all three configurations, with an indirect band gap with the top of the valence band at Γ and the bottom of the conduction band at Y. With respect to the valence band top and conduction band bottom, there is little dispersion along the alkyl side chains (Γ-B) and approximately 0.5 eV

	c [Å]	b [Å]	d [Å]	α [°]	β [°]	γ [°]
Config. I	7.709	3.852	15.8908	114.816	89.983	89.888
Config. II	7.742	3.828	15.605	114.165	90.635	96.995
Config. III	7.724	3.815	13.303	72.197	89.998	90.095
LDA [112]	7.7	3.8	15.9	-	-	-
LDA [128]	7.83	3.42	15.82	90.0	90.0	90.0
LDA [129]	7.6	3.8	-	90.0	90.0	90.0
expt [130, 131]	7.70	3.83	16.80	90.0	90.0	90.0
expt [132]	7.8	3.9	16.0	90.0	90.0	93.5
expt [133]	-	3.8	16	-	-	-
expt [134]	7.77	3.88	16.63	90.0	90.0	90.0
expt [135]	-	3.81±0.02	16.0±0.2	-	-	-
expt [136]	-	-	13-14	-	-	-

Table 4.4: Unit cell parameters for various P3HT configurations. The value c represents the length of the P3HT monomer (two thiophene rings) along the polythiophene backbone (**c**-axis). The value of b is the distance between adjacent lamellae (layers) in the $\pi - \pi$-stacking (**b** direction). The value of d represents the chain-to-chain distance within a lamella (along the **d** direction). The angles α, β, and γ are the angles between the **bd**-, **cd**-, and **cb**-planes, respectively. We note that we have not enforced orthorhombic constraints on the unit cells of our three P3HT configurations, hence we observe angles different to 90° in our models.

of dispersion along the $\pi - \pi$ stacking direction (Γ-Y) The dispersion along the polythiophene backbone (Γ-Z) is much more significant, in the region of 1.6 eV, or about three times as large as the dispersion along the $\pi - \pi$ direction. These observations are quantified in Table 4.6 and are consistent with other first principles studies on crystalline P3HT [128, 129]. The band dispersions indicate that the alkyl side-chains play little role in the electronic structure of the polymer. The narrow dispersion along the $\pi - \pi$ stacking direction suggests relatively weak interactions between the P3HT sheets. The wide dispersion along the polythiophene backbone, meanwhile, implies strong electronic interactions along that direction. It is also interesting to note that,

coordinate	Config. I	LDA [137]	LDA [138]	expt [137]	expt [138]
S_1—C_2 [Å]	1.727	1.715	1.696	1.714	1.714
C_2—C_3	1.393	1.368	1.367	1.369	1.370
C_3—C_4	1.403	1.415	1.409	1.423	1.423
C_4—C_5	1.384	1.368	1.367	1.369	1.370
C_5—S_1	1.730	1.715	1.696	1.714	1.714
$S_1C_2C_3$ [°]	110.3	111.3	111.3	111.5	111.5
$C_2C_3C_4$	112.3	112.6	112.4	112.5	112.5
$C_3C_4C_5$	114.9	111.3	111.3	111.5	111.5
$C_4C_5S_1$	109.1	112.6	112.4	112.5	112.5
$C_5S_1C_2$	93.3	91.1	92.6	92.1	92.2

Table 4.5: Comparison of the bond lengths and bond angles of the thiophene rings in optimised P3HT versus theoretical and experimental thiophene values. The thiophene chemical structure and atom numbers are shown in Figure 4.11(b). For clarity only the parameters of Configuration I are shown. The average value is presented in cases where the value of a parameter differs between the two thiophene monomers.

		HOMO		LUMO	
	Band gap	Γ-Z	Γ-Y	Γ-Z	Γ-Y
Config. I	0.79	-1.75	0.36	1.19	-0.19
Config. II	0.84	-1.66	0.33	1.25	-0.08
Config. III	0.82	-1.75	0.43	1.05	-0.16
LDA [129]	0.52	-1.88	-0.61	1.33	-0.41
LDA [128]	0.82	-1.92	-0.04	1.59	0.09

Table 4.6: Band gaps and band widths of various P3HT configurations (values in eV)

despite the changes in morphology along **d** between Configs. I, II, and III, the band gaps remain within 0.05 of each other. This provides further evidence that side chains do not contribute significantly to the electronic structure of P3HT and further supports the notion that the band gap is determined primarily by the conformation of the polythiophene backbone and by the

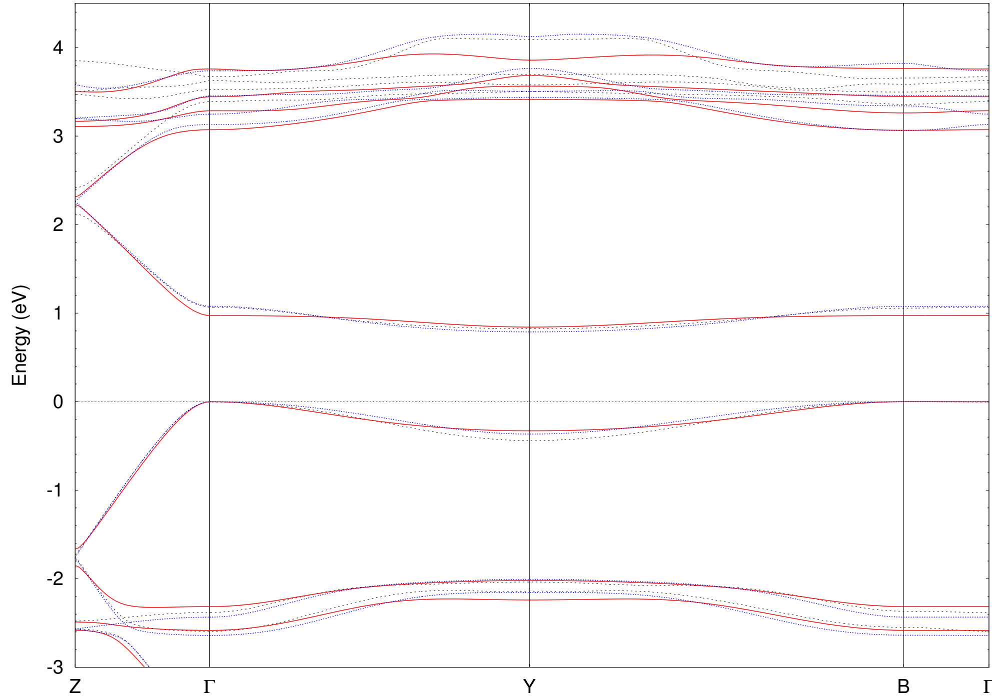

Figure 4.15: The band structures of P3HT in Configurations I (dotted blue), II (solid red), and III (dashed black). Each band structure is aligned such that the valence band top is at zero energy. The high symmetry points of the Brillouin zone are Γ(0,0,0,), Z($\frac{\pi}{c}$,0,0), Y(0,$\frac{\pi}{b}$,0), and B(0,0,$\frac{\pi}{d}$). The band gap for each Configuration is indirect, with the valence band top located at the Γ point of the Brillouin zone (or equivalently at the B point) and the conduction band bottom at the Y point.

distance separating the P3HT sheets along the $\pi - \pi$ axis. Finally, the total energy of the three configurations is within 0.22 eV per thiophene monomer (i.e. $\sim$9 meV/atom). This suggests that differences in the morphology - at least to the extent found in the three configurations examined here - do not significantly affect the overall stability of the polymer and that, most likely, processing conditions will play a large role in determining which conformation crystalline P3HT ultimately assumes.

Chapter 5

The Ideal ZnO/P3HT Photovoltaic Interface

5.1 Introduction

In this chapter we analyse the atomic structure and electronic energy-level alignment of the ZnO/P3HT interface from first principles. As explained in Chapter 1.4, knowledge of the energy-level alignment at the ZnO/P3HT interface is critical in order to estimate the maximum open circuit voltage of the system. We first determine a reliable atomistic model of the interface and then calculate the DFT energy-level alignment. The DFT alignment is improved using a hybrid functional approach in order to obtain an accurate value of V_{OC}. We note a discrepancy in our calculated V_{OC} compared with the one estimated by the electron affinity rule (Chapter 1.3.3) and examine the effect of the interfacial electrostatic dipole. We conclude with a comparison of our results to the experimental literature and discuss the implications

of our findings. All structural relaxations were performed at the LDA level, while all electronic structure calculations were carried out using the GGA. For the sake of clarity, the details of the computational calculations are discussed in Appendix A. Many of the results presented in this chapter were previously published in Ref. 139.

5.2 Atomic Structure

Our interface models consist of P3HT layers sitting atop a slab of ZnO in order to simulate the ZnO/P3HT interface of bilayer [28–33] and ZnO/P3HT core-shell nanowire [44] devices. This configuration also can be viewed as a cross-sectional representation of the interface of infiltrated nanowire array-based devices [28, 29, 32, 39–43]. We chose to adopt models where the P3HT lamellae lie flat on the ZnO surface based on the analysis of Ref. 44. In that work, TEM images of ZnO/P3HT core-shell nanowires show multiple layers of the polymer stacked on top of the semiconductor surface. Because the interlayer separation of the P3HT in the TEM images is consistent with the interlayer stacking parameter we calculated in Chapter 4.4 (b=3.82-3.85 Å), it is reasonable to assume that the polymer lays with the backbone (c-axis) parallel to the ZnO surface. The chosen P3HT morphology has been observed experimentally [27] on SiO_2/Si substrates using XRD and has also been assumed in another first-principles calculation of the ZnO/P3HT interface [112]. We chose not to simulate P3HT end-functionalised with phosphonic esters [44] as the inclusion of the functional groups dramatically increases the complexity of relaxing the structure of the interface model.

We will discuss the impact of this decision later in this chapter. Our P3HT layers are constructed with the same head-to-tail (HT) orientation as the bulk configurations described in Capter 4.4. The choice of using HT coupling was made exclusively in order to simulate highly regioregular P3HT (i.e. with a high fraction of HT-coupled thiophene monomers), which has higher mobility compared with films made with low regioregularity [27]. Furthermore, HT coupling has been demonstrated on SiO_2/Si [27] and highly ordered pyrolitic graphite (HOPG) [136] substrates.

We first constructed a four-layer ZnO slab terminating at the nonpolar $(10\bar{1}0)$ surface. As described in Chapter 4.1, this surface termination is the most energetically favourable one for ZnO [117]. Additionally, the $(10\bar{1}0)$ termination is exposed on the surface of highly oriented ZnO nanorods/nanotubes [140], making it the ideal orientation to choose when constructing ZnO/P3HT interface models designed to simulate nanowire-based devices. In the subsequent structural relaxations the bottom two layers of the ZnO slab were kept fixed in order to simulate the bulk, following the approach taken in Ref. 112. The transverse area of the ZnO slab (15.93×15.46 Å^2) was chosen to minimize the lattice mismatch between the ZnO and the P3HT that is caused by the periodic nature of the computational cell. In this configuration the P3HT backbone is compressed by <3.3% compared to the bulk values calculated in Chapter 4.4. Such a stretch on the c-axis of bulk P3HT affects its band gap by <0.01 eV, indicating that the strain induced at the interface is reasonably small.

In order to explore the energy landscape of the possible polymer configurations on the ZnO surface, we created four model interfaces, each with a

single layer of P3HT, sitting atop the semiconductor surface, oriented in a different way. Two of the configurations had the polythiophene backbone oriented along the $[1\bar{2}10]$ direction, while in the other two the backbone was oriented along the [0001] direction. Within each of these two orientations, one configuration had the C atoms at the 2,5 sites of thiophene rings placed on top of the Zn-O surface dimer rows, while the other had these reference atoms sitting in the trenches between the dimers. Each of these four configurations was relaxed and for each the binding energy of P3HT was calculated. The binding energy is calculated as $E_{\mathrm{b}} = E_{\mathrm{tot}} - E_{\mathrm{ZnO}} - E_{\mathrm{P3HT}}$, where E_{tot} is the total energy of the interface, and E_{ZnO} and E_{P3HT} are the total energies of the isolated ZnO slab and P3HT monolayer, respectively. It was found that the configuration with the polythiophene backbone oriented along the $[1\bar{2}10]$ direction and the references atom in the trenches between the surface dimers was the most stable, in agreement with Ref. 112, with a binding energy 30-120 meV per P3HT monomer lower than the other configurations. It should be noted, however, that the relatively small difference in total energies between the configurations suggests that other P3HT binding geometries on ZnO are at least likely at room temperature. The most stable configuration, shown in Figure 5.1, has a P3HT interdigitation length of 15.46 Å which is consistent with the d-values for the partly interdigitated P3HT structures (Configurations I and II) presented in Chapter 4.4. We also note that the P3HT layer lies 2.4 Å above the ZnO surface, as measured from the nearest S atom, and develops small ripples along the alkyl side chains (<0.5 Å in the direction perpendicular to the interface) in order to adapt to the underlying ZnO surface.

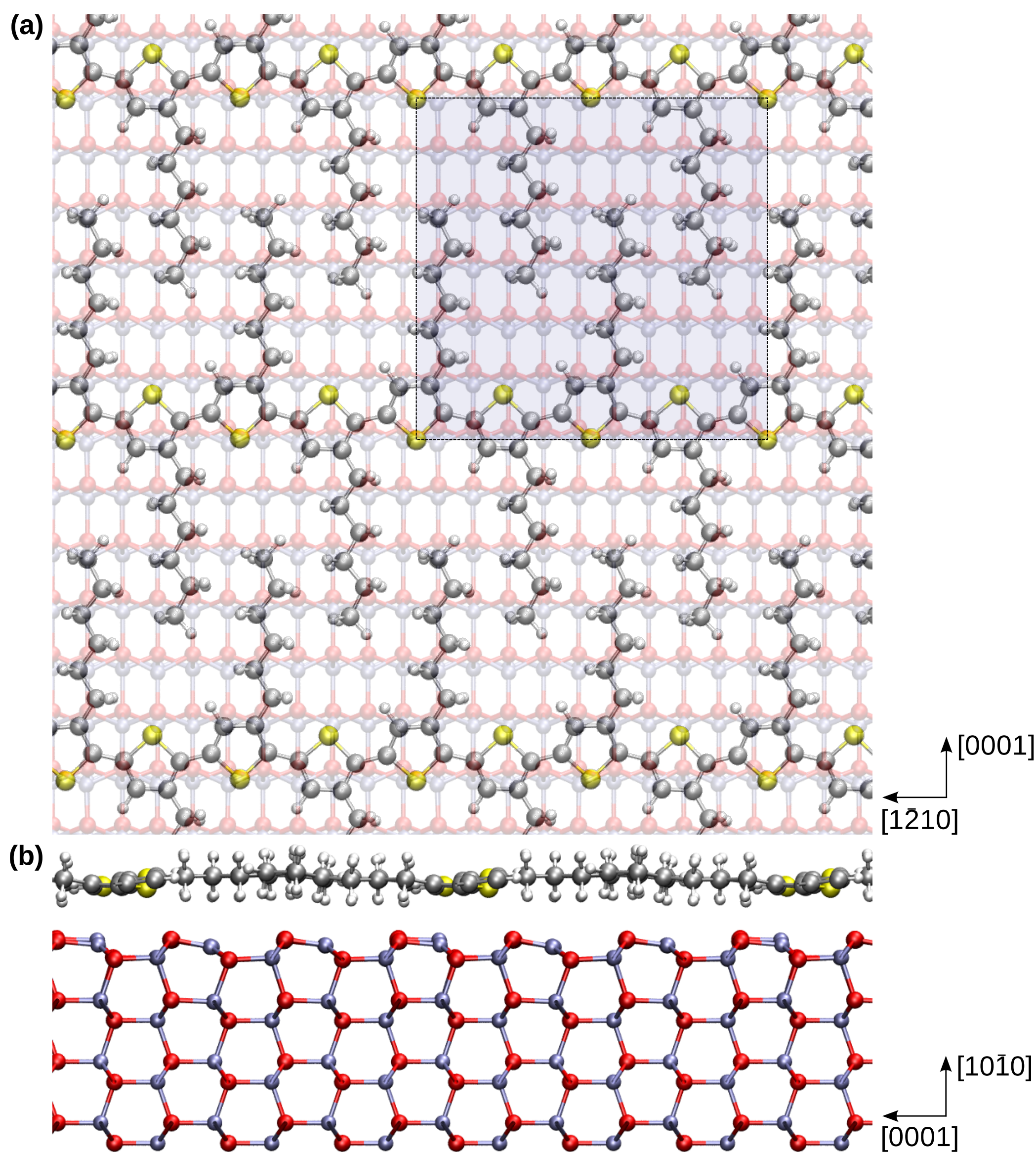

Figure 5.1: (a) Top and (b) side view of a single layer of P3HT adsorbed on ZnO. The two-dimensional periodic unit cell is shaded in blue in (a). Atomic colour code: O (red), Zn (blue), S (yellow), and H (white).

As shown in Ref. 44, real ZnO/P3HT PV devices have more than a monolayer of P3HT coverage, which suggests that a more realistic model interface should include at least several layers of P3HT. Using the most stable single-

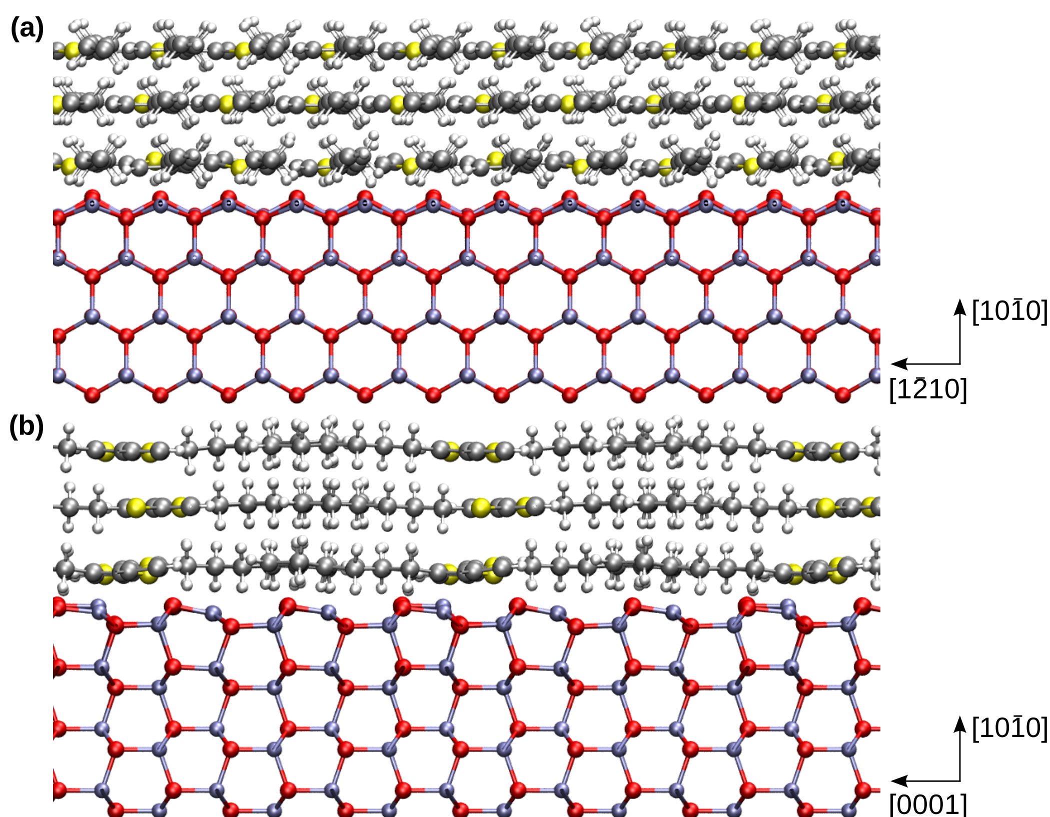

Figure 5.2: The ZnO/P3HT interface model. a) Side view of the optimised 3L ZnO/P3HT interface model, with the alkyl side chains perpendicular to the page. c) Side view of the optimised 3L ZnO/P3HT interface model, with the polythiophene backbone running perpendicular to the page.

layer interface as a starting point, we created a more realistic interface model by adding two additional layers of P3HT and re-relaxing the structure. The relaxed ZnO/triple-P3HT-layer (3L) interface is shown in Figure 5.2. As with the single-P3HT-layer model, the bottom P3HT layer of the 3L model sits 2.4 Å above the ZnO surface and shows the same rippling. The interlayer distance between the bottom and middle layer is 3.72 Å and between the middle and top layer is 3.36 Å. These values are measured as the distances between the S atoms of comparable thiophene rings for each layer. While

both of these distances are in good agreement with the *b*-values for bulk P3HT calculated in Chapter 4.4, they are notably shorter. This difference in *b*-values is most likely a result of the rippling of the P3HT layers due to the presence of the ZnO. The rippling causes uneven bending in the alkyl chains and thiophene rings, which causes each layer to adsorb in a unique manner. The S atoms of comparable thiophene rings are also shifted from each other by on average 1.4 Å in the [0001] direction, forming a A-B stacking pattern.

5.3 Interfacial Energy-Level Alignment

5.3.1 DFT Energy-Level Alignment

The DFT energy-level alignment was carried out, after performing electronic-structure calculations on the 3L interface, by examining the eigenvalues and wavefunctions of the heterojunction. By identifying the Kohn-Sham eigenvalue corresponding to the highest occupied molecular orbital (HOMO) of the system, we were able to identify the remaining band extrema of interest, namely the valence band maximum (VBM) and conduction band minimum (CBM) of the ZnO and the lowest unoccupied molecular orbital (LUMO) of the P3HT. The eigenvalues of these states are listed in Table 5.1. We corroborate our assignment of the band extrema by noting that the band gaps of ZnO (0.71 eV) and P3HT (0.82 eV) at the interface are in good agreement with the bulk values presented in Chapter 4. Furthermore, examination of the three-dimensional wavefunction plots, shown in Figure 5.3, reveals the correct character for the selected eigenstates; both VBM and CBM are lo-

calised on the ZnO (the latter displaying Zn 4s and O 2p character) and the HOMO and LUMO of the P3HT show the expected π and π^* character, respectively. We note that while the band offset of an interface can be determined by examining the local density of states [141], the physical separation of the ZnO and P3HT allows for clearly localised and identifiable orbitals. As a result, the method for assigning band extrema presented above is preferable.

The HOMO of the polymer is localised on the polythiophene backbones of the second and third P3HT layers, while the LUMO is confined to the backbone of the first P3HT layer and has significant overlap with the underlying ZnO slab (see Figure 5.3). As a result, the interface morphology examined here, wherein the P3HT alkyl chains lie parallel to the substrate, is expected to lead to efficient charge transfer upon dissociation of the exciton and provides *post-facto* justification for our choice of flat-lying P3HT lamellae. That the HOMO and LUMO of the polymer are both delocalised along the entirety of the polythiophene backbone suggests that the omission of phosponic ester functional groups is reasonable. These groups are present only at the anchor points of the polymer to the ZnO surface and, as such, should not greatly impact the electronic interactions along the rest of the chain or between P3HT layers.

5.3.2 Application of Hybrid Functionals

While the DFT band alignment presented in Section 5.3.1 produces the correct qualitative alignment, it is quantitatively inaccurate owing to the un-

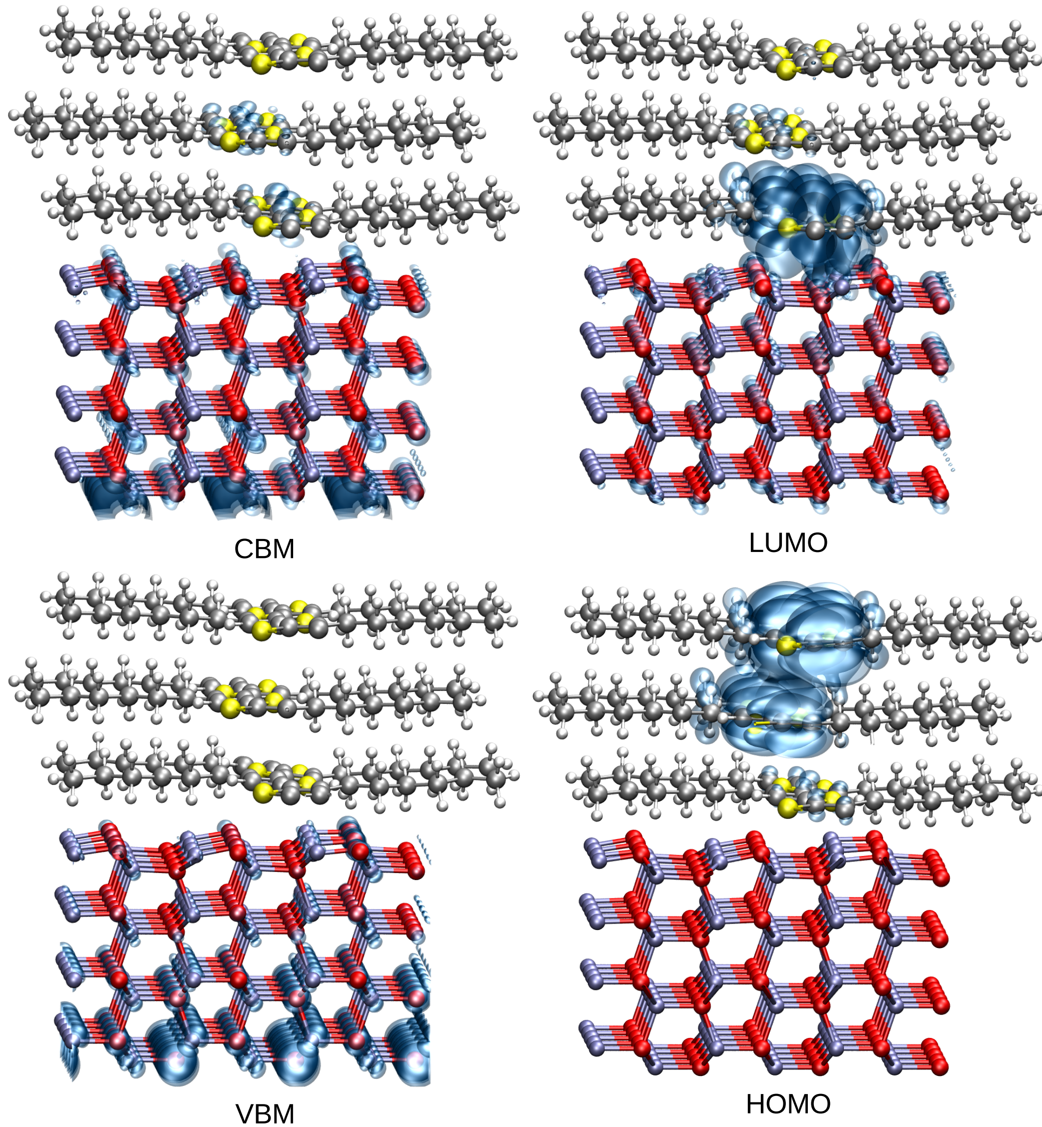

Figure 5.3: Frontier orbitals and band extrema at the ZnO/P3HT interface. Isosurface plots of the P3HT HOMO and LUMO wavefunctions (isovalue: 6.75×10^{-4} Å^{-3}), calculated for the interface model shown in Figure 5.2. As demonstrated by the top two pictures, the P3HT LUMO level spatially overlaps the ZnO conduction states, thereby favouring the efficient transfer of electrons upon exciton dissociation.

derestimation of band gaps at the DFT level. In order to establish a quantitatively accurate result, we turn to hybrid functionals, which were described

in Chapter 2.4 and can be used to increase the band gap by increasing the fraction α of Hartree-Fock exchange [102]. Given the number of electrons in the 3L model and the size of the corresponding computational cell (see Appendix A), however, performing a hybrid-functional calculation on the entire unit cell is infeasible. Instead, we used an alternative approach that is much less computationally demanding. It was shown in Ref. 102 that energy-band alignments for semiconductor-oxide interfaces could be reliably determined by matching hybrid-functional bulk band structures on top of an interfacial band offset calculated using DFT (see Chapter 3.6). We followed a similar approach to correct the DFT band alignment of the ZnO/P3HT interface. The hybrid-functional corrections were determined following the method described in Ref. 102. For each of bulk ZnO and P3HT we performed hybrid functional calculations and varied the fraction α of exact (Hartree-Fock) exchange until the experimental band gap is reproduced. In both cases the band gap increases linearly with increasing α. The optical band gap of ZnO is 3.4 eV [114] and can be reproduced computationally by using a fraction $\alpha_{\mathrm{ZnO}} = 0.375$. Following the discussion presented in Chapter 2.3.6, the appropriate band gap for comparison with DFT calculations is the quasiparticle gap and not the optical one. However, since the exciton binding energy of ZnO is only of the order of tens of meV [114], it can be neglected without significantly affecting the value of α. In the case of P3HT, the quasiparticle gap of 2.6 eV [142], obtained by photoelectron and inverse photoelectron spectroscopy, does not include excitonic effects and is markedly larger than the optical gap (1.9 eV [142]). The quasiparticle band gap of P3HT is matched using an exact exchange fraction of $\alpha_{\mathrm{P3HT}} = 0.367$. The

	KS [eV]	ΔH [eV]	Hybrid [eV]
CBM	0.07	0.98	2.07
VBM	-0.64	-1.66	-1.28
$E_{g,ZnO}$	0.71	2.64	3.35
LUMO	0.82	0.76	2.60
HOMO	0.00	-1.02	0.00
$E_{g,P3HT}$	0.82	1.78	2.60

Table 5.1: Energies of the ZnO VBM and CBM, and the P3HT HOMO and LUMO at the ZnO/P3HT interface. The energy levels under "KS" correspond to the DFT Kohn-Sham states at the interface. The values under "ΔH" are the hybrid-functional corrections to the DFT levels of bulk ZnO and P3HT (with $\alpha_{\mathrm{ZnO}} = 0.375$ and $\alpha_{\mathrm{P3HT}} = 0.367$, respectively). For completeness, the band gaps at the interface are also reported. The zero of the energy axis is set to the HOMO level of the P3HT in all cases.

hybrid-functional corrections to the bulk energy levels were determined by taking the difference between the hybrid-functional and DFT eigenvalues for a given state. For example, the correction to the P3HT HOMO is given by $\Delta\mathrm{HOMO} = \mathrm{HOMO}_{\mathrm{hyb}} - \mathrm{HOMO}_{\mathrm{DFT}}$, where $\mathrm{HOMO}_{\mathrm{hyb}}$ and $\mathrm{HOMO}_{\mathrm{DFT}}$ are the hybrid-functional and DFT eigenvalues, respectively, of the HOMO. Directly comparing the eigenvalues for two separate calculations is justified here since in both cases the eigenvalues are referenced to the cell-averaged total potential (i.e. the sum of the averages of the Hartree potential, local ionic pseudopotential and XC potential). In the present case this total potential is identical in both the DFT and hybrid-functional calculations since they both use the same computational cell and hence have the same average Hartree potential (which is set to zero in `Quantum ESPRESSO`), ionic positions placement and electron density. The hybrid-functional corrections to the bulk ZnO and P3HT levels are shown in Table 5.1.

Following the approach of Ref. 102, we could directly apply the bulk hybrid-functional band structures to a interfacial band offset determined from a DFT calculation, as illustrated in Chapter 3.6. The band offset corresponds to the difference in the local averages of the planar-averaged total potential normal to the interface, shown in Figure 5.4. (We note that while the band offset used in Chapter 3.6 is determined via the electrostatic potential, here the total potential is more appropriate since it is to this value to which `Quantum ESPRESSO` refers the eigenvalues.) This method, however, proves problematic for two reasons. First, the local average of the total potential for P3HT is not well defined and can vary substantially depending on how many layers are used to compute the average. Specifically, the averages over the first (bottom), second, and third layers P3HT (shown as p_1, p_2, and p_3, respectively, in Figure 5.4) vary by several tenths of an eV. This magnitude of error can potentially be significant in calculations where we wish to determine the open-circuit voltage. Second, the alignment method of Chapter 3.6 requires that the bulk band structure of a material be aligned to the average of the electrostatic (or total) potential of the bulk cell, presuming that this average is equivalent to the local average determined at the interface. For P3HT, however, this assumption is not necessarily a good one. The morphology of P3HT in bulk is not identical to its morphology at the interface and thus a direct comparison of their average electrostatic (or total) potentials can be troublesome.

Consequently, a better approach is to apply the hybrid-functional corrections of Table 5.1 directly onto the DFT interfacial band alignment. The procedure is shown schematically in Figure 5.5, while the final hybrid-corrected

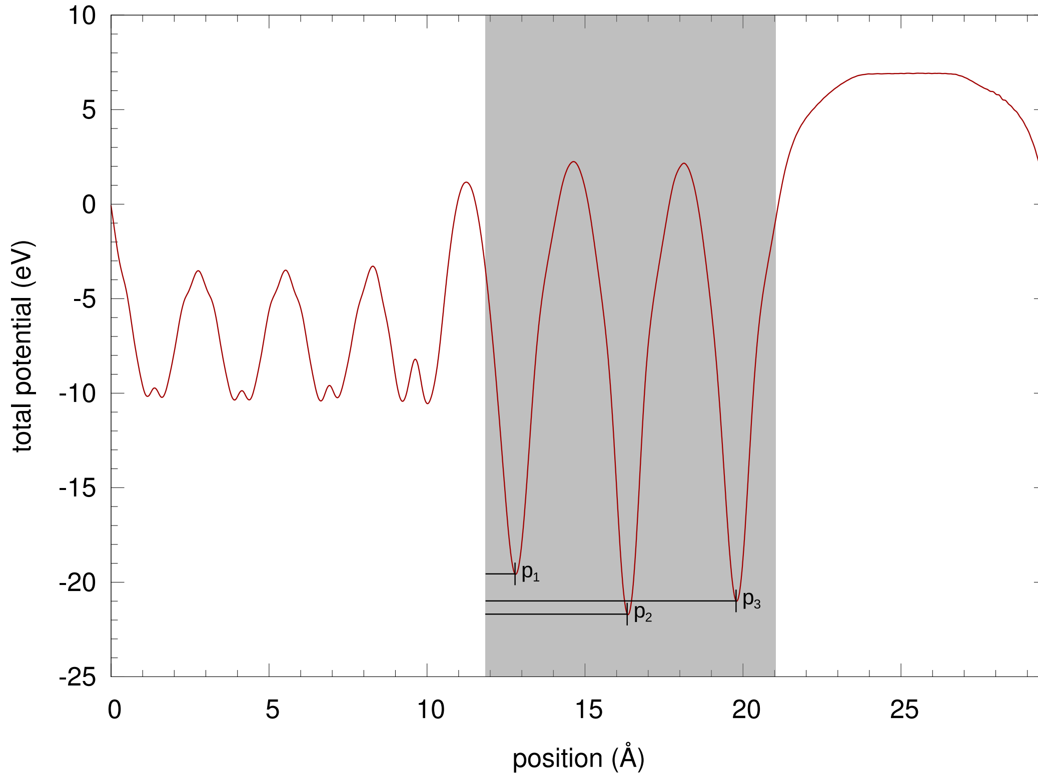

Figure 5.4: The planar-averaged total potential normal to the interface along the unit cell. The shaded region corresponds to the P3HT layers in the unit cell, with p_1, p_2, and p_3 denoting the distance from the beginning of the P3HT region to the first, second, and third P3HT layers, respectively.

eigenvalues are listed in 5.1. The final band gaps of the ZnO and P3HT at the interface are within 0.1 eV of the corresponding experimental bulk values.

Verification of the Hybrid-Functional Correction Scheme

The validity of applying bulk hybrid-functional eigenvalue corrections to the eigenvalues of a DFT interface calculation was independently verified by examining a small test system comprising a thiophene molecule adsorbed on a ZnO $(10\bar{1}0)$ slab (Figure 5.6). The transverse area of the slab measures

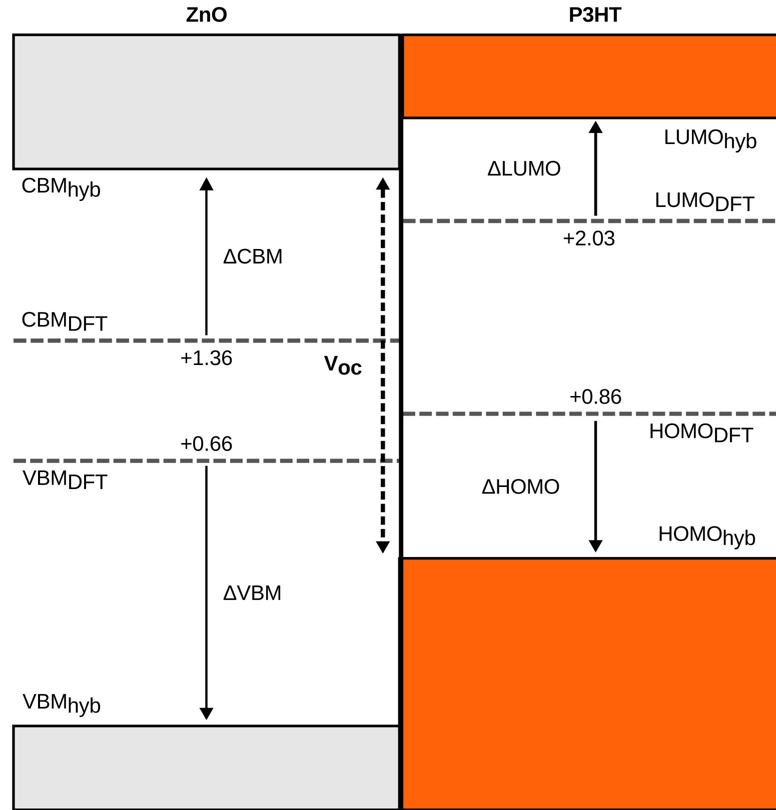

Figure 5.5: The application of hybrid-functional corrections to the DFT energy-level alignment. The dashed lines (labelled with subscript "DFT") show the DFT levels of the band extrema, whose values are also indicated. The solid lines (labelled with subscript "hyb") show the hybrid-functional-corrected levels. The relatively magnitudes and directions of the hybrid corrections are indicated with arrows and labelled as ΔVBM, ΔCBM, ΔHOMO, and ΔLUMO for the corresponding ZnO and P3HT levels. The open-circuit voltage, defined as the difference between the hybrid-corrected CBM and HOMO, is also indicated for completeness.

12.7×10.3 Å and in the optimised structure the C atoms at the 2,5 sites of the thiophene rings are located in the trenches between the Zn-O surface dimers, 2.61 Å above the ZnO surface. The energies of the VBM and CBM of the ZnO and the HOMO and LUMO of the thiophene molecule were examined using two methods: i) by applying hybrid-functional correc-

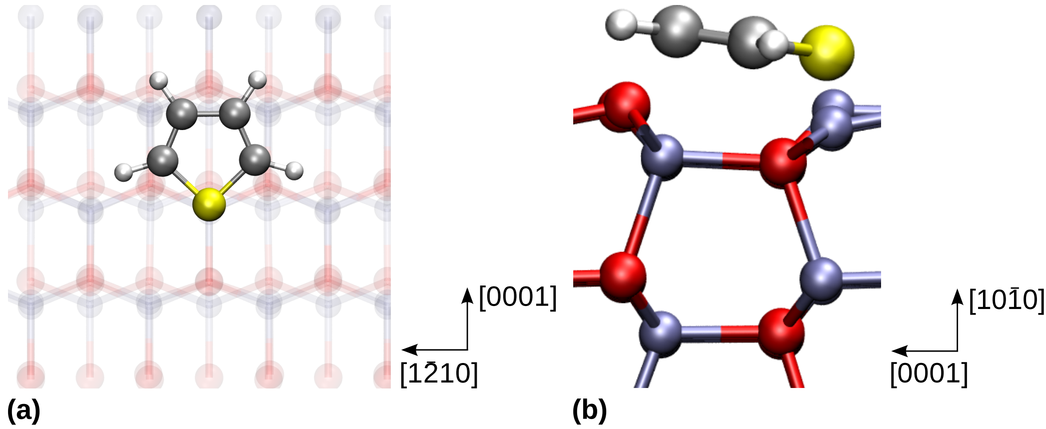

Figure 5.6: The model ZnO/thiophene interface used to validate the hybrid-functional scheme as seen from a) the top and b) the side.

	VBM [eV]	CBM [eV]	HOMO [eV]	LUMO [eV]
KS + ΔH Scheme	1.28	4.36	0.00	6.82
H Scheme	1.25	4.30	0.00	6.85

Table 5.2: The eigenvalues of the band extrema at the model ZnO/thiophene interface. The “KS + ΔH scheme corresponds to the application of bulk-derived hybrid functional correction to the DFT (Kohn-Sham) eigenvalues obtained from the full interface calculation. The H Scheme corresponds to a hybrid functional calculation (with $\alpha = \alpha_{\mathrm{ZnO}} = 0.375$ performed on the full interface.

tions, obtained from separate bulk calculations, onto the DFT energy-level alignment (as outlined in Section 5.3.2 and here referred to as the KS + ΔH scheme) and ii) by performing explicit hybrid-functional calculations on the entire interface (H scheme). For consistency between the two approaches, and because we were only interested in comparing the performance of the two schemes, the fraction of exact exchange was set to the value for ZnO used in Section 5.3.2, $\alpha_{\mathrm{ZnO}} = 0.375$. The eigenvalues of the band extrema for both of the schemes are shown in Table 5.2. Examination of the eigenvalues shows that the energy-level alignment calculated using the KS + ΔH

approach agrees with that determined using a direct hybrid-functional calculation on the full interface to within less than 0.1 eV. This agreement provides justification for using the KS + ΔH scheme on the full ZnO/P3HT interface, as described in Chapter 5.3.2.

Alternative Approach to Hybrid-Functional Energy-Level Alignment

As described above, determining the interfacial energy-level alignment by applying bulk hybrid-functional band structures to a DFT interfacial band offset is problematic due to the uncertainty involved in determining the local reference potential for P3HT at the interface and due to the inconsistency between the reference potential of P3HT in the bulk and at the interface. Nevertheless, this method can still be useful for establishing the sensitivity of our calculated alignment to the methodology used in its determination.

Here we refer the bulk band structures for ZnO and P3HT to the cell-averaged electrostatic potentials. In both cases the cell-averaged potential is identically zero since `Quantum ESPRESSO` sets the average of the Hartree potential to zero and we manually forced the average of the local ionic pseudopotential to zero by modifying the code. Referring the band structures to the cell-averaged electrostatic potential obviates the need to compute the average of the planar-averaged electrostatic potential for P3HT, which, as stated, is difficult to compare with the averaged P3HT local electrostatic potential at the interface. We then align the bulk band structures, via their electrostatic reference potentials, to the DFT band offset calculated at the

interface. This offset was calculated as the difference in the averages of the planar-averaged local electrostatic potentials for ZnO and P3HT, taken over all of their respective layers. Once aligned, we apply the appropriate bulk hybrid-functional corrections of Table 5.1 to the eigenvalues of ZnO and P3HT to establish the interfacial energy-level alignment. The energy-level alignment so determined agrees with that of Table 5.2 to within 0.15 eV, which we can take as an estimate of the error in our preferred alignment method.

5.4 Open-Circuit Voltage

5.4.1 Calculated V_{OC}

The hybrid-functional energy-level alignment presented in Table 5.1 is shown schematically in Figure 5.7. As described in Chapter 1.3.3 the maximum open-circuit voltage (V_{OC}) of a hybrid photovoltaic device is defined as the difference between the CBM of the semiconductor and the HOMO of the polymer. In our calculation, then, we find $V_{\mathrm{OC}} = 2.07$ V (see Table 5.1), which is in good agreement with the optical gap of P3HT (1.9 eV), within the 0.15 eV margin of error described in Section 5.3.2. This indicates that the ZnO/P3HT interface is intrinsically capable of operating with negligible "loss-in-potential" [145], defined as the difference in energy between the optical band gap of the light absorber (1.9 eV for P3HT) and the open-circuit voltage. The implication of this is that the ZnO/P3HT interface can, in principle, operate with an open-circuit voltage equal to the optical gap of

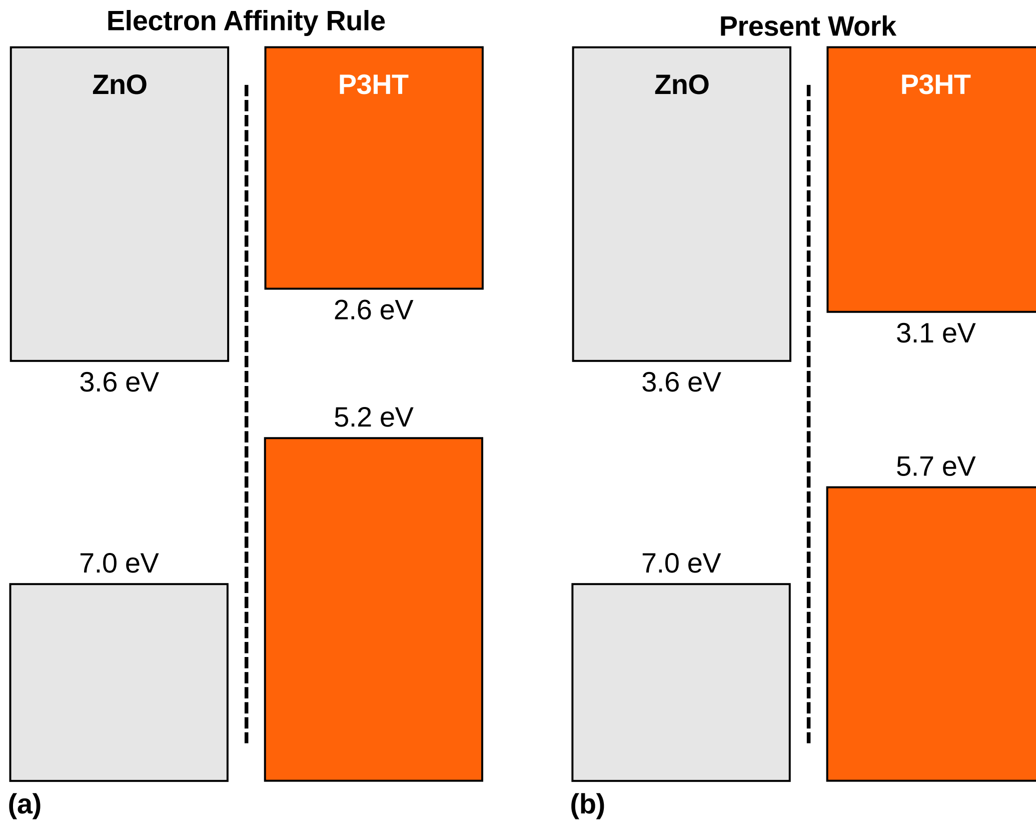

Figure 5.7: Schematic energy-level alignment at the ZnO/P3HT interface. (a) Empirical energy diagram obtained within the electron affinity rule, using the ZnO work function of Ref. 143, the P3HT ionisation potential of Ref. 144, and the P3HT (quasiparticle) band gap of Ref. 142. (b) Energy-level diagram obtained using our combined DFT and hybrid-functional calculations based on the interface model shown in Figure 5.2b,c. Our calculations include the effects of the interfacial charge transfer, which are neglected in a). For ease of comparison, the ZnO CBM is set to 3.6 eV below the vacuum level in both cases.

P3HT (i.e. the highest possible value after consideration of the exciton binding energy) and, as a consequence, the theoretical maximum device efficiency of ZnO/P3HT PV devices can be considerably higher than what has been achieved to date. Table 5.1 shows that the offset between the LUMO of the P3HT and the CBM of the ZnO is 0.53 eV, which falls in the range 0.4-0.7

eV of exciton binding energies reported for P3HT [10, 142]. The calculated energy-level alignment is therefore compatible with exciton dissociation at the interface and, in particular, with measurements of the external quantum efficiency that show a charge generation onset at around 1.9-2.0 eV (625-650 nm) [31].

5.4.2 Electrostatic Dipole

In the experimental literature the ideal V_{OC} is estimated using the electron affinity rule, in which the interfacial energy diagram is obtained by aligning the vacuum levels of the two materials forming the interface. The energy-level alignment so obtained is shown in Figure 5.7 and leads to an ideal V_{OC} of 1.6 eV [143, 144], over 0.5 V lower than our calculated value.

To explain this discrepancy we examined the effects of the electrostatic dipole at the interface. By its nature, the electron affinity rule ignores charge transfer between the two materials upon formation of the interface. In real interfaces, however, the charge transfer between the donor and acceptor creates an electrostatic dipole and a corresponding potential offset that acts to reduce the energy mismatch [146–148]. Given the physisorbed nature of P3HT on ZnO, it is not obvious that the electrostatic dipole potential generated at the interface is significant.

In order to quantify this effect we first determined the electronic charge redistribution upon formation of the interface, $\Delta n(\mathbf{r}) = n_{\mathrm{ZnO/P3HT}}(\mathbf{r}) - [n_{\mathrm{ZnO}}(\mathbf{r}) + n_{\mathrm{P3HT}}(\mathbf{r})]$. Here $n_{\mathrm{ZnO/P3HT}}$ is the ground-state DFT charge density of the ZnO/P3HT interface, n_{ZnO} is the charge density of the ZnO slab with-

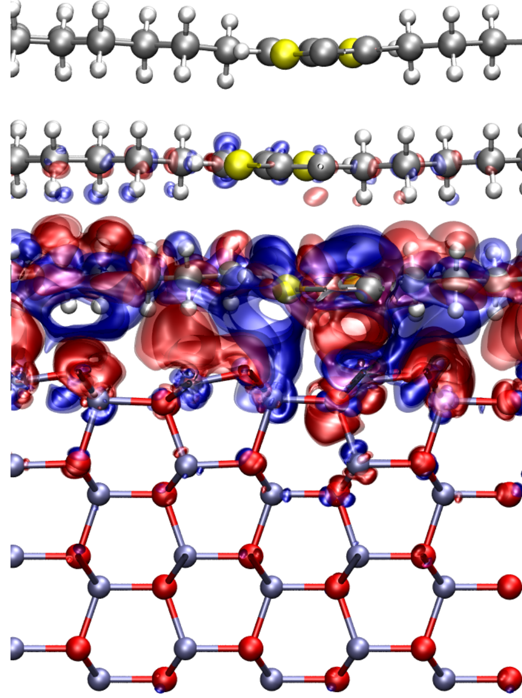

Figure 5.8: Charge redistribution at the ZnO/P3HT interface: isosurface of the charge redistribution upon formation of the interface (isovalue: $\pm 2.02 \times 10^{-3}$ electrons/Å^3 for red/blue), obtained as $n_{\mathrm{ZnO/P3HT}} - [n_{\mathrm{ZnO}} + n_{\mathrm{P3HT}}]$. $n_{\mathrm{ZnO/P3HT}}$, n_{ZnO}, and n_{P3HT} are the electronic charge densities of the interface and the isolated ZnO and P3HT, respectively.

out the P3HT layers in the same computational cell, and n_{P3HT} is the charge density of the P3HT layers without the ZnO slab. The charge redistribution $\Delta n(\mathbf{r})$ is shown graphically in Figure 5.8 and is clearly localised around the interface, between the top of the ZnO slab and the first P3HT layer. The corresponding potential offset was calculated by integrating the planar average of the charge redistribution along direction normal to the interface (dashed blue line in Figure 5.9) using Poisson's equation

$$\nabla^2 V_{\mathrm{dip}} = -4\pi \Delta n(z), \tag{5.1}$$

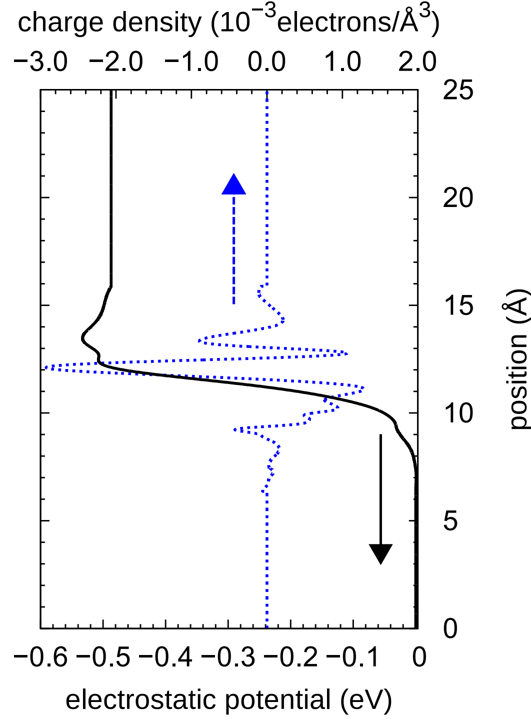

Figure 5.9: Charge transfer and corresponding dipole at the ZnO/P3HT interface. The planar average of the charge redistribution along the interface, $\Delta\bar{n}(z)$ is shown as the dashed blue line. This curve has been restricted to the reduced range of charge in between the middle of the ZnO slab and the middle P3HT layer (see text). The charge outside this range has been set to zero in order to avoid including spurious dipoles with the vacuum region of the cell. The corresponding electrostatic potential profile across the interface (solid black line) is obtained by integrating the limited region of $\Delta\bar{n}(z)$ using Poisson's equation.

where V_{dip} is the electrostatic potential offset and $\Delta\bar{n}(z)$ is the planar-averaged charge redistribution in the cell (of volume Ω) along the direction normal to the interface

$$\Delta\bar{n}(z) = \frac{1}{\Omega}\int \Delta n(\mathbf{r})dxdy. \tag{5.2}$$

In order to avoid including spurious dipoles at the interfaces with the vacuum

region of the computational cell, we limited the integration of $\Delta\bar{n}(z)$ to the range in between the middle of the ZnO slab and the middle P3HT layer. This approximation is justified as the vast majority of the averaged charge redistribution occurs within this range, as illustrated in Figure 5.8. The electrostatic dipole potential is shown as the solid black line in Figure 5.9. Examination of this figure reveals that there is significant charge transfer from the first P3HT layer to topmost ZnO layer underneath. The total charge transferred is 1.4×10^{13} electrons cm^{-2} (0.15 electrons per P3HT monomer), and the associated electrostatic dipole potential step is 0.5 eV. This dipole potential step acts to align the band edges of the two materials, in agreement with considerations based on the matching of the respective charge neutrality levels [104] described in Chapter 3.8. The calculated magnitude of the potential is significant with respect to the V_{OC} predicted by the electron affinity rule, therefore the standard approximation of neglecting this effect is not appropriate for the ZnO/P3HT interface. Adding this offset to the interfacial energy diagram obtained using the electron affinity rule gives a CBM-HOMO separation (i.e. an ideal V_{OC}) of 2.1 V, in good agreement with the 2.07 V calculated in Section 5.4.1.

Verification of the Electrostatic Dipole

As a check of the electrostatic potential calculated above, we also calculated this potential using an alternative method. In this approach we examined the DFT energy levels corresponding to the isolated ZnO and P3HT layers, which do not include the effect of charge transfer, by lifting the P3HT layers

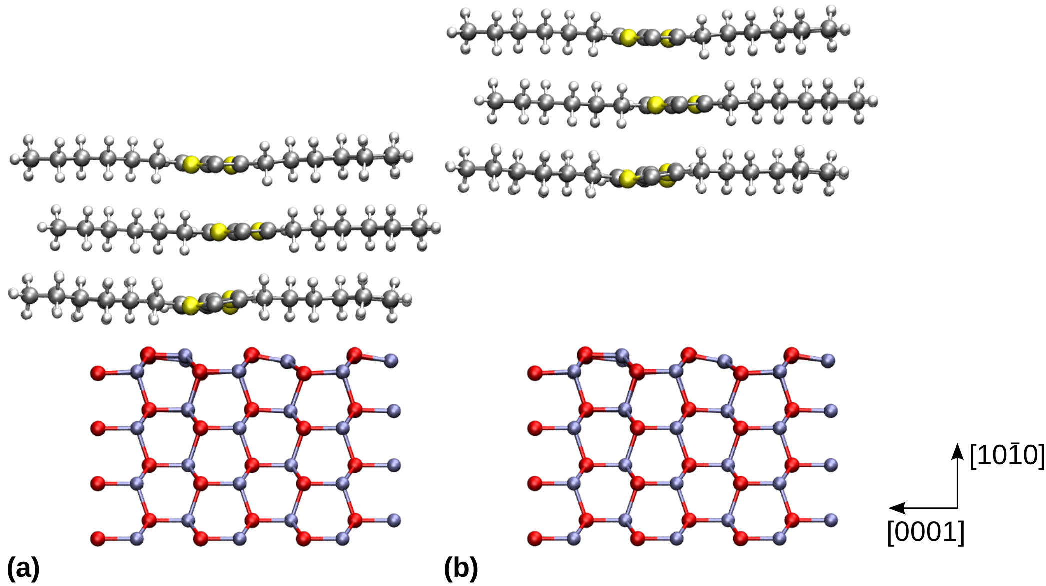

Figure 5.10: The two model interfaces used to verify the electrostatic dipole potential. In (a) the P3HT is adsorbed to the ZnO surface, while in (b) the polymer is lifted off the surface by 9 Å. The interface in (b) represents a desorption of the polymer from the semiconductor surface and the energy-level alignment can therefore be directly compared to the EA alignment.

9 Å from the surface and effectively desorbing the polymer from the ZnO. These DFT energy levels were referred to the total local potential in vacuum. The unit cells of the adsorbed (3L) and desorbed interfaces are shown in Figure 5.10. The energy-level alignment so obtained yields a CBM-HOMO offset 0.53 eV smaller than that of the full interface calculation, corresponding to an electrostatic dipole potential of 0.53 V. The excellent agreement between the two approaches indicates the method described above is appropriate for the present interface. Although both methods are expected to yield the same value for the dipole offset, the calculation via the charge density is preferred for two reasons. First, the charge density is the fundamental quantity in DFT and, second, the accurate determination of the vacuum level through

the total local potential is complicated by both the long-range Coulombic interactions between the periodic replicas of the interface and the necessity for dipole corrections [103] due to the inequivalent surfaces at the top and bottom of the interface model.

5.4.3 Experimental V_{OC}

In experimental ZnO/P3HT photovoltaic devices the open-circuit voltage falls in the range 0.4-0.8 V [45], substantially lower than the 2.07 V predicted in our calculations. One reason for the lower V_{OC} in experimental devices is charge carrier recombination. In our calculations, charge carrier dynamics are not considered and the open-circuit voltage can be calculated as in Equation 1.9. In actual devices, however, charge carriers formed upon exciton dissociation can recombine across the interface, thereby reducing the charge carrier density from the ideal value. In Ref. 149 it was shown that in organic PV devices, an increase in the rate k_{rec} of bimolecular recombination (i.e. recombination across the interface) reduces the open-circuit voltage. As mentioned in Chapter 1.3.1, the V_{OC} of a photovoltaic device is the voltage at which the photogenerated current is equal in magnitude to the reverse current flowing in the device, including dark current and recombination current. When the operating voltage of the device increases so to does the photocurrent. Assuming devices with negligible dark current, as in Ref. 149, increasing k_{rec} will increase the reverse current and, consequently, will lower the operating voltage at which open circuit is achieved. Phrased more simply, an increase in the rate of bimolecular recombination acts to

lower the open-circuit voltage of organic PV devices. The open-circuit voltage for the P3HT-based device in Ref. 149 shows a variation in the region of 0.2 eV depending on the value of k_{rec}. It is reasonable to expect a value of similar magnitude for the ZnO/P3HT devices considered here. The value of k_{rec}, among other factors, depends strongly on the interfacial morphology and the presence of defect-induced trap states [149]. As such, in experimental devices featuring disordered P3HT layers and including defects, we would expect a high rate of recombination and a resulting drop in V_{OC} as compared to the idealised model interface that we consider in this chapter. This observation leads naturally to the conclusion that fabricating devices with ordered, defect-free P3HT morphologies will enhance the open-circuit voltage with respect to the devices reported to date in the literature. Further, it has recently been suggested that the short depletion length of ZnO could also be responsible for the charge carrier recombination at the ZnO/P3HT interface [150], leading to band bending at the interface and a resulting reduction of V_{OC}. Increasing the depletion length of ZnO could therefore reduce the interfacial recombination and allow for a substantial increase in the open-circuit voltage.

Apart from recombination effects, it is possible that the presence of oxygen vacancies in ZnO close to the interface may pin the ZnO Fermi level near the vacancy defect levels, as observed in Schottky contacts to ZnO [151] (the process of Fermi-pinning was described in Chapter 1.3.3). In particular, the $V_O(+2, 0)$ defect level of ZnO lies 0.7 ± 0.2 eV below the CBM of ZnO [151], therefore a corresponding reduction in V_{OC} may be expected.

Taken together, the effects of recombination and ZnO defects could lower

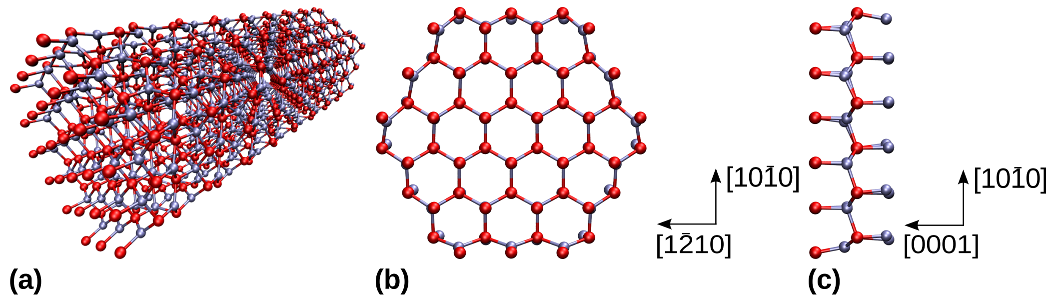

Figure 5.11: The optimised atomic structure of the ZnO nanowire. a) Perspective view of the nanowire. b) Cross-sectional view showing the variation in lattice parameter from the centre of the wire to its edges. c) Side view of wire along its growth axis.

V_{OC} in fabricated ZnO/P3HT PV devices by around 1 eV from its ideal maximum value, further indicating that the 2.07 V value calculated in our idealised model is reasonable.

5.5 Quantum Confinement

In hybrid organic-inorganic photovoltaics based on ZnO quantum dot/polymer blends [28, 34–38] or ZnO nanorod/polymer interfaces [28, 29, 32, 38–44], the charge carrier confinement in the ZnO could affect the energy-level alignment at the interface. We quantified this effect by examining the change in band gap between bulk ZnO and a model ZnO nanorod of diameter 1.5 nm, shown in Figure 5.11. The nanorod, which extends along the [0001] direction, was generated by cutting bulk ZnO through its six $10\bar{1}0$ facets and contains 108 atoms.

The effect of quantum confinement on the nanorod is to increase its band gap by 0.4 eV relative to the band gap of bulk ZnO (0.84 eV, see Chapter 4.1). This increase is in agreement with previous first-principles calculations [152].

This result can be extended to nanorods of larger diameter by using a simple scaling argument based on the energy levels of an electron confined in a cylindrical well: $\Delta E_{\mathrm{g}} = \Delta E_{\mathrm{g,ref}}(d/d_{\mathrm{ref}})^{-2}$, where d and ΔE_{g} represent the nanorod diameter and quantum confinement correction to the ZnO band gap, respectively. For ZnO nanorods with a diameter between 8 and 100 nm [38, 41, 44], $\Delta E_{\mathrm{g}} < 14$ meV, indicating that the effect of quantum confinement on the ZnO energy-level alignment is negligible for nanorods of practical diameter.

5.6 Conclusions

In this chapter we have explored the ZnO/P3HT hybrid organic-inorganic photovoltaic interface. Using first-principles DFT calculations we studied an ideal interface morphology from which we determined the DFT energy-level alignment. The electronic structure calculations revealed a significant overlap of the P3HT LUMO with the ZnO conduction states, suggesting an efficient charge transfer from P3HT to ZnO upon dissociation of the exciton at the heterojunction. While qualitatively correct, the interfacial DFT band structure is inaccurate due to the underestimation of band gaps at the DFT level. Modifying the method proposed in Ref. 102 to suit a semiconductor/polymer interface, hybrid functionals were used to obtain a quantitatively accurate interfacial energy-level diagram. This hybrid-functional alignment reveals a maximum open-circuit voltage of 2.07 V that, when our margin of error is considered, is at the level of the 1.9 eV optical band gap of the polymer. This result indicates that the ZnO/P3HT interface can theoretically operate at a

negligible "loss-in-potential" and that the efficiency of PV devices based on these materials could be markedly higher. For example, if it were possible to realise a ZnO/P3HT organic-inorganic hybrid photovoltaic device with same short-circuit current and fill factor as that of Ref. 37, but with the V_{OC} calculated in this chapter, a device efficiency as high as $\eta = 5.6\%$ could be expected.

The EA model predicts a maximum V_{OC} significantly lower than that of our calculations. Using a charge transfer approach, we determine the presence of an interfacial electrostatic dipole that results in a potential step of 0.5 eV across the interface. This dipole step acts to bring the band structures of the ZnO and P3HT together, in line with the discussion on the charge neutrality level presented in Chapter 3.8, and acts to reduce the open-circuit voltage of the interface by 0.5 V. Since the electron affinity model neglects the electrostatic dipole, our calculated maximum V_{OC} is entirely consistent with the estimations derived through the EA model.

Finally, we note that the low open-circuit voltages observed in experimental ZnO/P3HT devices can be attributed to high rates of bimolecular recombination and ZnO oxygen defects. Together, these non-idealities can reduce V_{OC} by upwards of 1 V vis-à-vis that of our ideal model, which again indicates that our calculated open-circuit voltage is consistent with the experimental literature. We can conclude from our analysis that, were it possible to fabricated devices with ideal, defect-free morphologies, the observed V_{OC} of experimental devices would be in line with the value presented in this chapter.

Chapter 6

GaAs Nanowires Coated with P3HT

6.1 Introduction

In Chapter 1.4 we noted that the charge transport in hybrid organic-inorganic PV devices using GaAs nanowires (NWs) suffers due to charge traps induced by defect-states. It was noted that one solution is to coat the NWs with conducting polymers that simultaneously form a PV heterostructure with and transfer charge to the NWs, thereby passivating the defects. In this chapter we examine a model GaAs/P3HT interface in order to examine the interfacial charge transfer characteristics of GaAs NWs coated with P3HT. The work in this chapter was performed in response to research later published in Ref. 59. In that study our experimental collaborators examined P3HT overcoats on both "as-grown" NWs, coated in an oxide layer (*o*-GaAs NWs), as well etched NWs (*e*-GaAs NWs) whose oxide layer was removed before

application of the polymer. All structural relaxations and electronic structure calculations in this chapter were performed at the LDA level. Further details of the computational calculations are presented in Appendix A. Part of the work presented in this chapter was previously published in Ref. 59.

6.2 Model Interfaces

We constructed our interface models starting from pristine (non-oxidised) and oxidised GaAs wurtzite $(10\bar{1}0)$ slabs presented in Chapter 4.2. The GaAs NWs used in Ref. 59 terminate at the zinc blende (110) surface and not, as in our models, the wurtzite $(10\bar{1}0)$. However, as mentioned in Chapter 4.2, the surface reconstruction for the GaAs zinc blende (110) and wurtzite $(10\bar{1}0)$ surfaces are similar and thus, for the purposed of determining the charge transferred from P3HT, the use of the wurtzite termination is acceptable. To complete our interface models, three layers of P3HT were added atop each of the pristine and oxidised GaAs slabs and each interface structurally relaxed. The polythiophene backbones of the P3HT layers in both interfaces were chosen to run along the $[1\bar{2}10]$ direction of the GaAs, mimicking the most stable orientation calculated for the ZnO/P3HT heterostructure in Chapter 5. The optimised pristine interfaces is shown in Figure 6.2. The structure of P3HT on the $(10\bar{1}0)$ surface is similar to that of P3HT on $(10\bar{1}0)$ ZnO. We note that the bottom P3HT layer is 2.79 Å from the surface - as measured from the closest S atom - and the polymer once again exhibits rippling on the order of 0.5 Å perpendicular to the surface. The interdigitation length, d, of the polymer at the interface is 13.16 Å. This is shorter than the

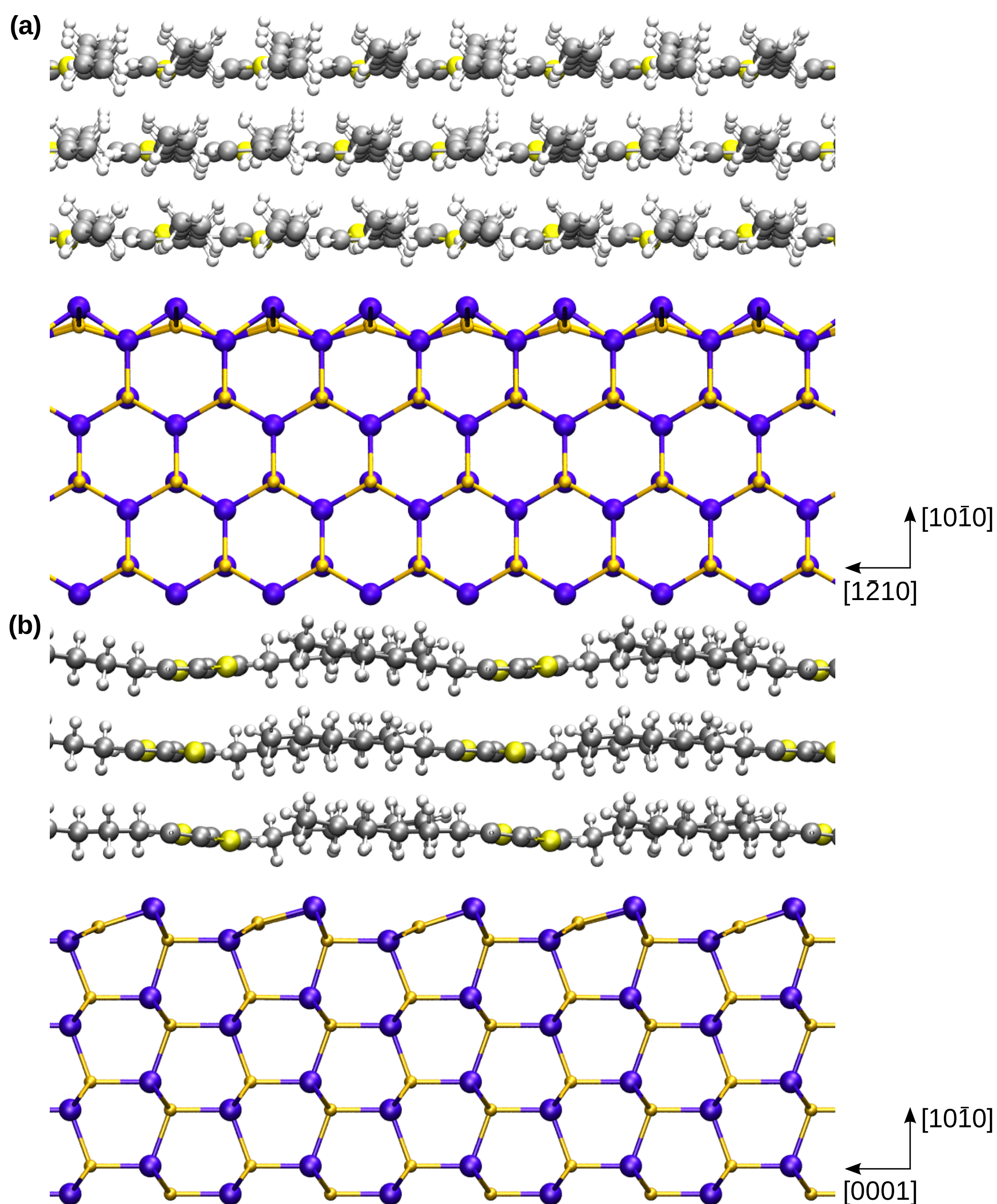

Figure 6.1: The pristine GaAs/P3HT interface model. (a) Side view of the interface with the alkyl side chains perpendicular to the page. (b) Side view of the interface with the alkyl side chains parallel to the page. Atomic colour code: Ga (violet), As (gold), S (yellow), C (gray), and H (white).

interdigitation length for the ZnO/P3HT interface but still reasonably in line with the experimental range of values listed in Table 4.4. This value is also consistent with the range of values we calculated for bulk P3HT in Chapter 4.4. The interlayer P3HT distances are 3.64 Å between the bottom and middle layers, and 3.51 Å between the middle and top layers. Both values are in line with the lattice parameters listed in Table 4.4.

Figure 6.2 illustrates the structurally optimised model of the oxidised interface. Here we notice a more extreme departure from the ZnO/P3HT adsorption conformation, with the trenches in the GaAs surface, induced by the oxide layer, causing the bottom layer of the polymer to tilt significantly toward the surface. At its closest the polymer is 1.84 Å from the surface, with the thiophene rings lying directly above the As-O surface dimers. The interdigitation length for the oxidised interface is, as with the pristine interface, 13.16 Å. The interlayer distance between the middle and top P3HT layers is 3.37 Å compatible with the distances of Table 4.4. The distance between the bottom and middle layers, however, is more difficult to quantify due to the severe tilting of the thiophene rings above the trenches in the GaAs surface. For consistency, we choose to measure the interlayer distance as the difference between the S atoms of equivalent thiophene rings, leading to an interlayer separation between bottom and middle layers of 4.03 Å which is larger than any of the experimental or calculated separations shown in Chapter 5.

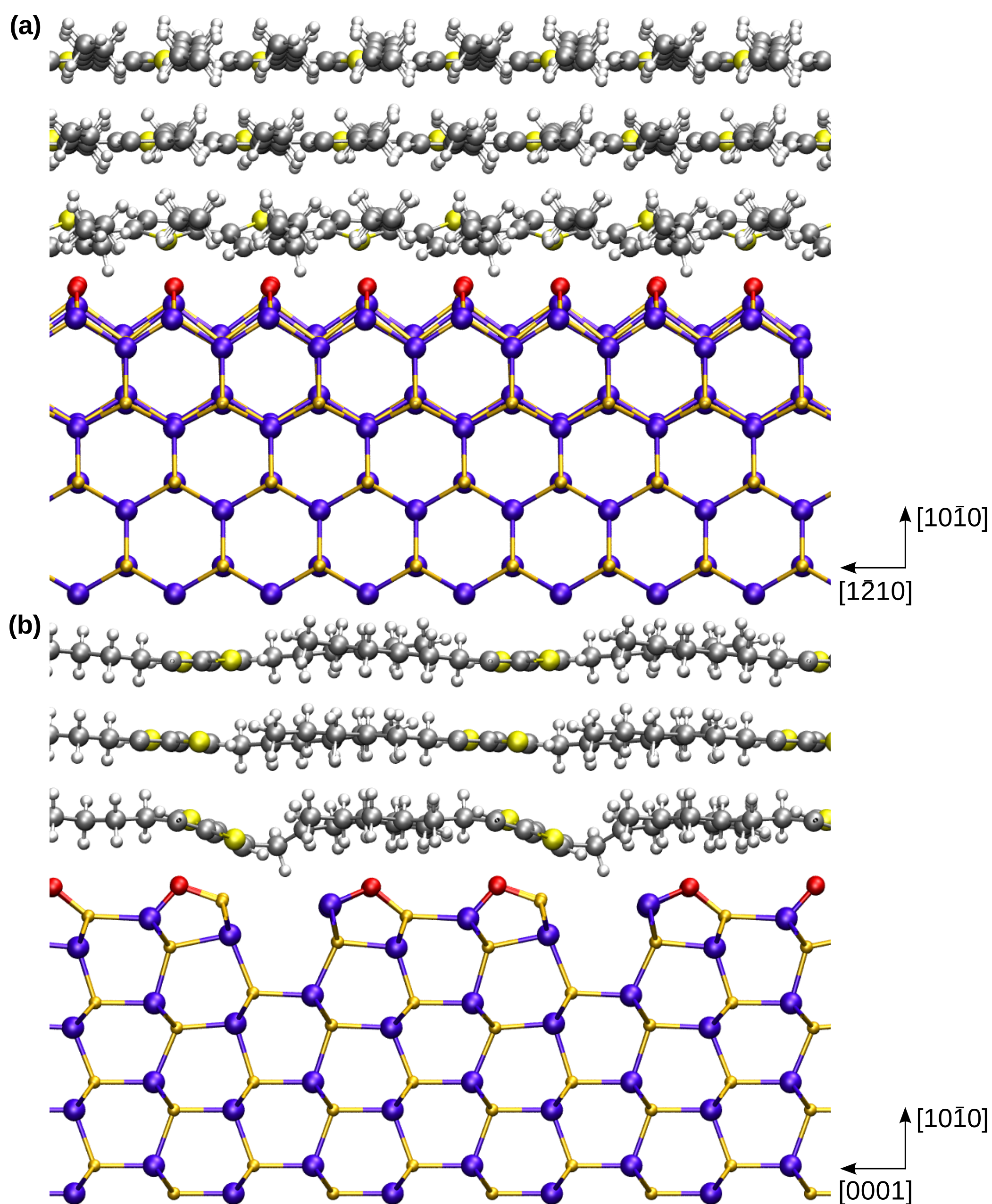

Figure 6.2: The oxidised GaAs/P3HT interface model. (a) Side view of the interface with the alkyl side chains perpendicular to the page. (b) Side view of the interface with the alkyl side chains parallel to the page.

6.3 Charge Transfer

To determine whether or not P3HT can passivate surface traps on the *o*-GaAs and *e*-GaAs NW surfaces, we must examine the ground state charge transfer characteristics from the polymer to the semiconductor surface. Employing the same method used in Chapter 5.4.2 we calculated the charge redistribution $\Delta\bar{n}(z)$ for both the pristine and oxidised interfaces, as shown in Figure 6.3. We note in both interfaces a clear charge transfer from the polymer to the GaAs, localised around the interface region, with the charge transferred from the P3HT to the semiconductor equal to 1.4×10^{13} electrons cm^{-2} and 4.0×10^{13} electrons cm^{-2} for the pristine and oxidised interfaces, respectively. These values correspond to 0.044 electrons per P3HT monomer (i.e., two thiophene rings) for the pristine interface and 0.13 electrons per P3HT monomer for the oxidised interface. The localisation of the redistribution is more clearly illustrated by examining the spatial charge redistribution, $\Delta n(\mathbf{r})$, shown in Figure 6.4. In this figure we note that the majority of the charge redistribution for both interfaces occurs between the middle layer of the polymer and the middle of the GaAs slab.

As in the case of the ZnO/P3HT heterojunction, the interfacial charge redistribution upon formation of the interfaces examined here will lead to an electrostatic dipole potential. This potential can be calculated in the same way as in Chapter 5.4.2. In order to avoid including the spurious dipoles with the vacuum, we integrate only the charge redistribution $\Delta\bar{n}(z)$ in the region between the middle of the GaAs slab and the middle layer of the polymer. This region for both interfaces is shown as the bold lines in Figure 6.3.

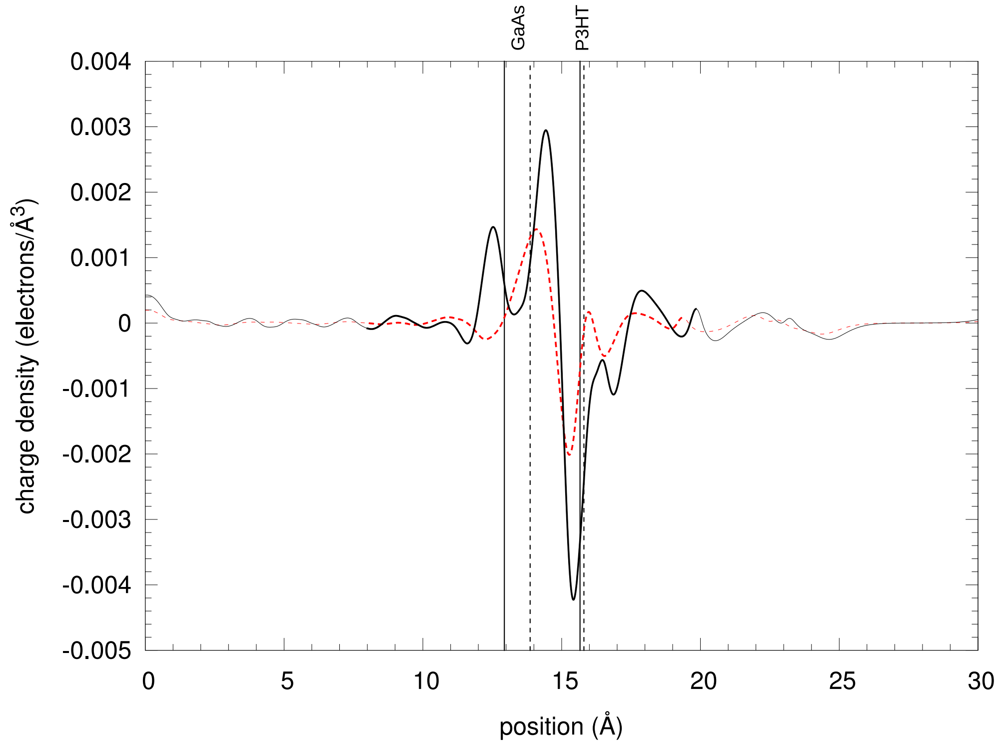

Figure 6.3: The planar averaged charge redistributions, perpendicular to the interface ([10$\bar{1}$0] direction), of the pristine (dashed red) and oxidised (solid black) interfaces. The bold segments of each curve represent the charge redistribution from the middle of the GaAs slab to the middle layer of the P3HT, which corresponds to region containing the majority of the charge transfer. The vertical solid and dashed lines indicate the averaged coordinates of the top of GaAs slab and the bottom P3HT layer for the pristine and oxidised interfaces, respectively.

Given that the vast majority of the charge is transferred in this region, the limiting of the integrated charge region in the calculation of the dipoles is not expected to significantly affect their values. The electrostatic dipole potentials corresponding to the limited charge regions of Figure 6.3 are shown in Figure 6.5. The dipole potential step for the pristine interface is ∼0.18 eV, while for the oxidised interface it is ∼0.51 eV. The larger dipole potential of the oxidised interface is assigned to the presence of the electronegative O

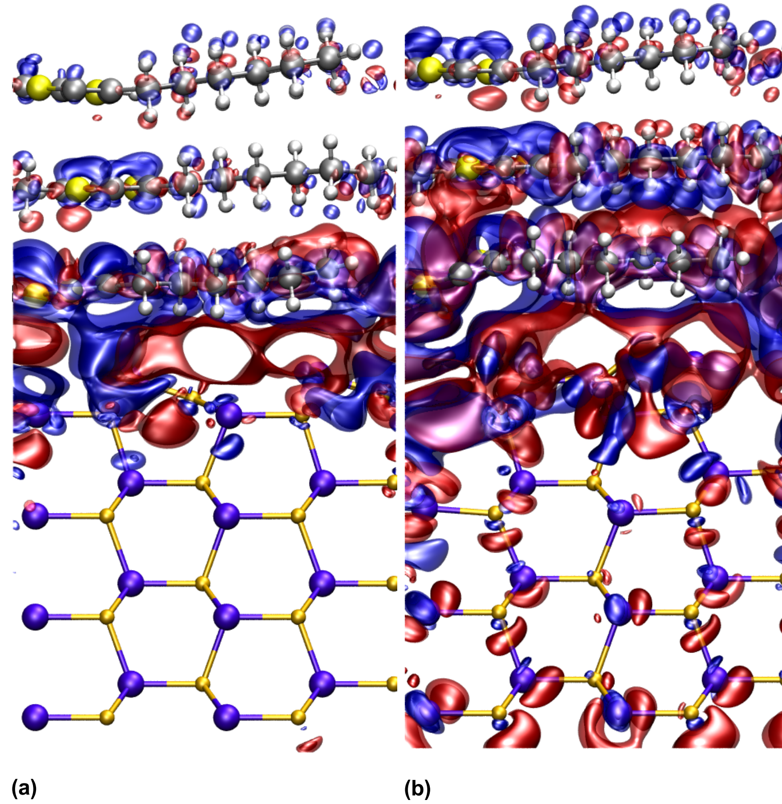

Figure 6.4: Isosurfaces of the charge redistribution at the (a) pristine GaAs/P3HT and (b) oxidised GaAs/O/P3HT interfaces (isovalue: $\pm 6.75 \times 10^3$ electrons/Å^3 for red/blue). The charge redistribution, $\Delta n(\mathbf{r})$, was introduced in Chapter 5.4.2.

atoms at the semiconductor surface. Examining Figure 6.4 reveals a large net accumulation of charge around these atoms.

In order to determine whether or not the pristine and oxidised interfaces are suitable to PV applications, the electrostatic dipole potentials for each heterojunction can be applied to the energy alignment of the GaAs and P3HT levels obtained from the electron affinity rule. Doing so provides a reasonably accurate representation of the energy-level alignment without the need to do a full hybrid-functional alignment, as demonstrated in Chapter 5.4.2.

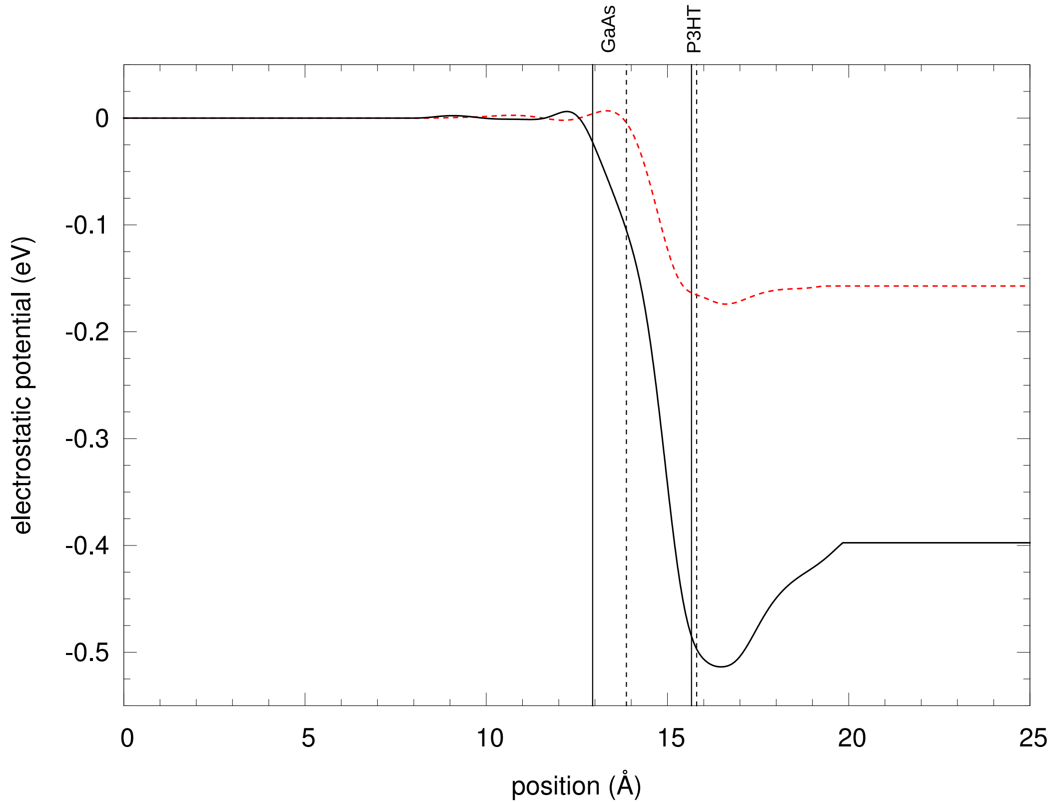

Figure 6.5: The electrostatic dipole potential profiles of the pristine (dashed red) and oxidised (solid black) interfaces, as obtained by integrating the bold segments of the respective curves in Figure 6.3 using Poisson's equation. The use of a limited segment of the charge transfer is intended to eliminate the contribution of spurious dipoles at the interfaces with the vacuum region of the computational cell, as described in Chapter 5.4.2. The vertical solid and dashed lines indicate the averaged coordinates of the top of GaAs slab and the bottom P3HT layer for the pristine and oxidised interfaces, respectively.

The dipole acts to bring the band structures of the two materials together by an amount equal to its potential step. Here we choose to use the levels of the GaAs from experiment and correct the eigenvalues of the P3HT levels. For consistency, we use the same vacuum levels for (bulk) GaAs [153] and P3HT [154] as used in Ref. 59. Figure 6.6 shows the EA energy-level alignment and the dipole-adjusted alignments for the pristine and oxidised

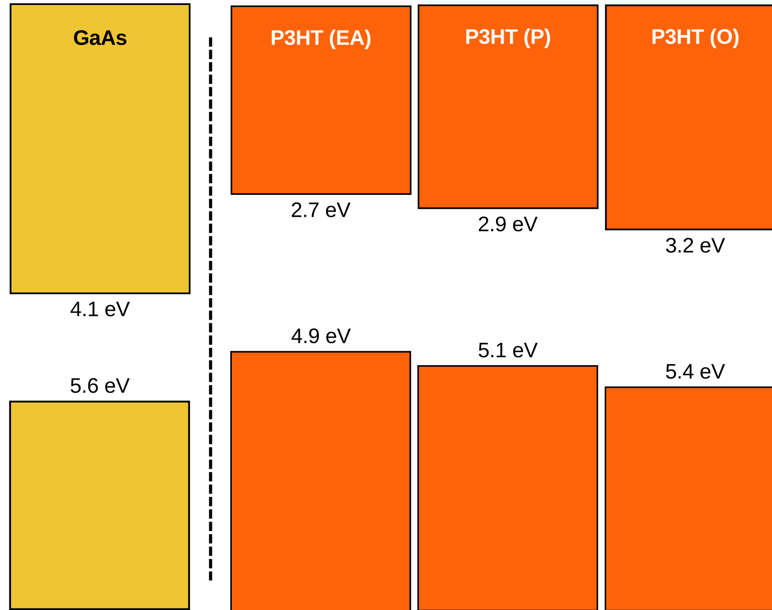

Figure 6.6: Energy-level alignment at the GaAs/P3HT interface. The presented vacuum-aligned (EA) levels for GaAs are bulk values obtained from Ref. 153 and those for P3HT (labelled as "EA") are from Ref. 154. To obtain the pristine and oxidised P3HT levels (labelled "P" and "O", respectively) the electrostatic dipole potentials of Figure 6.5 were applied. In each case the corresponding potential step was used to bring the P3HT levels towards the GaAs levels, in line with the discussion of the charge neutrality level presented in Chapter 3.8. Each of the pristine and oxidised interfaces forms a type II heterostructure with the bulk GaAs levels, consistent with the PL lifetimes extracted from the time-resolved PL spectra of Ref. 59.

interfaces. Even after the application of the dipole corrections to the EA levels, both the pristine and oxidised interfaces remain type II heterojunctions, indicating that both would be suitable to PV applications. We do note, however, that the GaAs levels are taken from its bulk form and do not account for the any changes due to the presence of the oxide layer. In the actual GaAs/P3HT devices used in Ref. 59, the Fermi level of the GaAs NWs does not change upon etching, leading us to assume that the use of bulk levels for GaAs is a reasonable approximation. Although the morphology of P3HT

changes significantly from the pristine to the oxidised interfaces, its band gap changes by only 0.06 eV. It is therefore reasonable to use the same (bulk) band gap for P3HT in both the pristine and oxidised interfaces, as shown in Figure 6.6.

6.4 Comparison with Experiment

In Ref. 59 time-resolved photoluminescence (PL) measurements were taken to measure the charge carrier dynamics of both the *o*-GaAs and *e*-GaAs NWs. The PL lifetime was measured for bare NWs (those without the polymer coating) as well as those embedded in a P3HT matrix. From the transient PL spectrum of bare *o*-GaAs NWs, a single-exponential fit PL lifetime of 46.5 ps was extracted. It has been previously demonstrated that the short PL lifetime of uncoated GaAs NWs is caused by a dominant nonradiative decay channel originating from charge trapping at surface-defect states [54, 57]. Upon etching with HCl, the carrier dynamics of the uncoated NWs show only a minimal variation, with the PL lifetime of the uncoated *e*-GaAs NWs only marginally higher at 52.1 ps. From these observations the conclusion can be drawn that the charge carrier dynamics for both native (oxidised) and etched NWs are dominated by the surface-defect states.

Previous studies [155–157] have demonstrated that charge transfer across the interface of a type II heterojunction reduces the PL lifetime of the donor. The observation from Ref. 59 that the PL lifetime of *o*-GaAs NWs decreases to 15 ps upon coating with P3HT suggests that a type II interface does indeed form between GaAs and the polymer. This view is consistent with the band

alignment presented in Figure 6.6. The short PL lifetime of the P3HT-coated *o*-GaAs NWs, however, indicates that the charge-carrier dynamics are still dominated by surface traps and that the polymer overcoat does not successfully passivate the defect states of the nanowire. This result appears at odds with our finding of significant charge transfer from the polymer to the GaAs at the oxidised interface. The apparent contradiction can be explained by noting that the oxide layer of the actual *o*-GaAs/P3HT devices has a thickness of $\sim$1 nm, whereas in our model is it only one atomic layer thick. The thick oxide layer of the prepared devices might prevent the GaAs surface-defect states from being effectively passivated and might contribute to the short PL lifetime observed experimentally.

The carrier dynamics for the *e*-GaAs NWs are somewhat more complicated. As noted above, surface-defect states still dominate the dynamics of bare *e*-GaAs NWs, with the PL lifetime essentially unchanged from that of bare *o*-GaAs NWs. Interestingly, in contrast with the *o*-GaAs NWs, upon coating of the etched NWs with P3HT the PL lifetime increases dramatically to 128 ps. The enhancement of the PL lifetime can be attributed to the passivation by the polymer of the surface-state defects in the GaAs NWs and a corresponding reduction in the charge trapping. Verification of this assumption is provided by the charge transfer calculated for our pristine interface. From Figure 6.3 it is clear that there is a net flow of charge from the P3HT to the GaAs surface, which, in the absence of a thick oxide layer, fills the defect states and reduces the trapping of charge. The formation of a type II heterojunction also plays a significant role in the charge carrier dynamics of the etched wires. In fact, in Ref. 59 it was observed that the PL lifetimes of

e-GaAs/polymer blends (including blends with polymers not analysed in this chapter) show a strong dependence on the ionisation potential (IP) of the polymer, with the polymer having the lowest IP (P3HT) having the highest lifetime.

6.5 Conclusions

In this chapter we have analysed the atomic structure of both the pristine and the oxidised GaAs/P3HT interfaces. While the pristine interface is structurally reminiscent of the ZnO/P3HT model explored in Chapter 5, the oxidised interface shows a dramatic difference. The deep trenches that open in the GaAs surface, due to the presence of the O atoms, cause the bottom P3HT layer to tilt substantially, and such a change in morphology could be expected to alter the interfacial energy-level alignment.

Ground state charge transfer from the polymer to the semiconductor is observed for both interfaces, with more charge per thiophene ring crossing the interface in the oxidised model. The increase in charge transfer with respect to the pristine interface is assigned to the presence of electronegative O atoms, which attract more electrons from the polymer (as seen in Figure 6.4). The calculated charge transfer at the pristine interface corroborates the observation of Ref. 59 that upon etching the PL lifetime of GaAs/P3HT blends increases dramatically, due largely to the filling of the surface-defect traps states and the resulting elimination of the dominant PL quenching channel. Our results for the oxidised interface model would suggest a similar increase in PL lifetime of *o*-GaAs/P3HT blends, however this is not observed ex-

perimentally. The discrepancy is due to the presence of a thick oxide layer ($\sim$1 nm) at the surface of the *o*-GaAs NWs. In contrast with the thin (atomic-layer) oxide of our model, the thick native oxide layer is expected to prevent charge from reaching the GaAs surface and passivating the surface trap states. Our model does suggest, however, that achieving a thin native oxide layer for *o*-GaAs NWs could result in effective surface-defect state passivation and could potentially eliminate the need for an additional etching step in order to realise significant PL quenching. Determining methods for reducing the thickness of the oxide layer could provide interesting avenues for future research.

Chapter 7

The Ideal Graphene/P3HT Photovoltaic Interface

7.1 Introduction

In Chapter 1.4 we described how graphene is seen as an ideal replacement for fullerene- and CNT-based acceptors in organic PV devices. In the present chapter we model ideal graphene/P3HT interfaces and determine the DFT energy-level alignment at the interface of the two materials. We note the failure of DFT to produce a qualitatively accurate alignment and apply hybrid-functional eigenvalue corrections to obtain an accurate description of the interfacial alignment. We calculate a V_{OC} consistent with experimental values and seek to explain the discrepancies of measured V_{OC} with the EA rule predictions. Finally, we examine the effect of oxidation and its role in the energy-level alignment and open-circuit voltage of the interface. All structural relaxations were performed at the LDA level, while all electronic

structure calculations were carried out using the GGA. Additional details of the computational calculations are presented in Appendix A.

7.2 Atomic Structure

The graphene/P3HT interface is studied using two ideal models, one with a single layer of both graphene and P3HT (1L interface) and the other with two layers of each material (2L interface). The final, optimised structures of both interface models are shown in Figures 7.1 and 7.2. The graphene layers in both the 1L and 2L models are composed of a 6×7 supercell along the zig-zag and armchair axes, respectively, with the layers in the 2L interface stacked in an A-B (Bernal) manner. The C-C bond length in both interface models is 1.41 Å in agreement with the results presented in Chapter 4.3. Each layer of P3HT consists of four monomers (i.e. two thiophene rings), aligned such that the alkyl chains run along one of the crystallographic axes of graphene. This type of alignment has been shown for P3HT on highly oriented pyrolytic graphene (HOPG) substrates [136]. The 1L interface contains a total of 368 atoms (168 graphene, 200 P3HT), while the 2L interface contains 736 atoms (336 graphene, 400 P3HT). In both interfaces the interdigitation length of the P3HT is 14.65 Å and the strain on the c-axis of the P3HT, compared with the bulk DFT values listed in Chapter 4.4, is less than 4%. This strain causes a change in the band gap of less than 0.01 eV compared to the bulk value and can be considered to have an insignificant impact on the energy-level alignment at the interface. The transverse area (parallel to the surface) of both the 1L and 2L computational unit cells is 14.65×29.66 Å^2. The

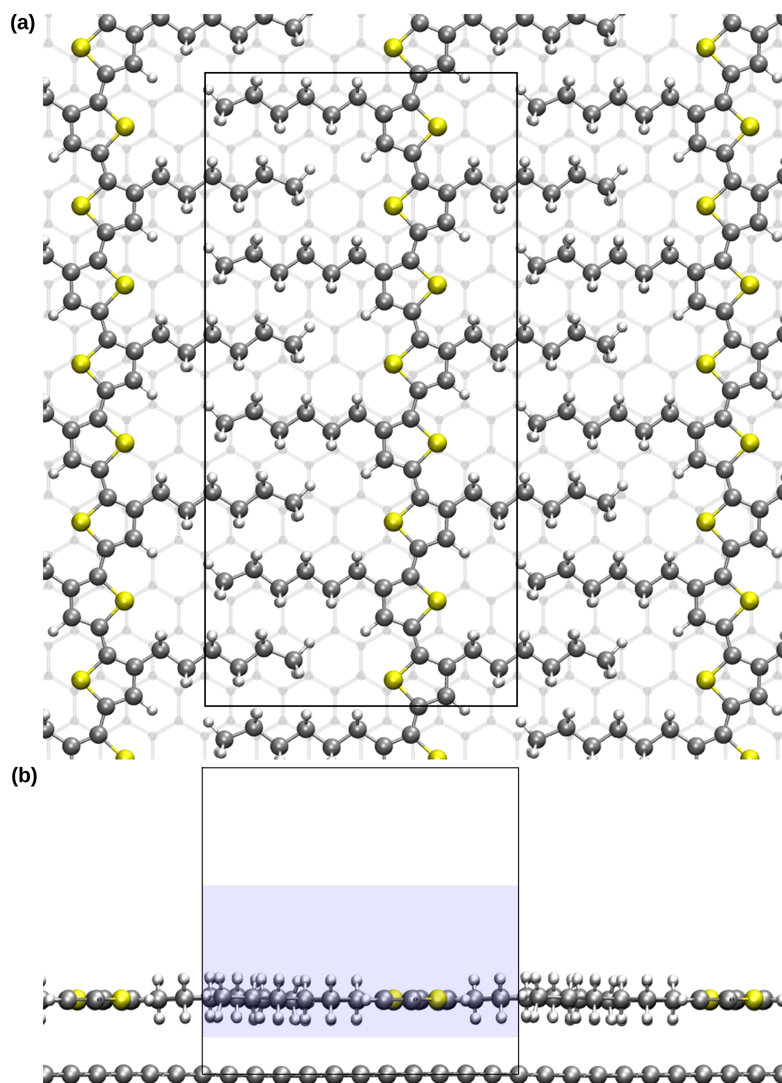

Figure 7.1: (a) Top and (b) side views of the ideal single-layer graphene/P3HT interface model. The shaded area in (b) represents the P3HT region of the computation cell, defined as the region extending from the midpoint between the graphene and P3HT layers to the midpoint of the vacuum region.

P3HT in the 1L interface is adsorbed 3.48 Å above the graphene surface, as measured by the difference in the z-averaged coordinates of both layers. Similarly, the first layer of P3HT in the 2L interface lies 3.30 Å above the graphene, and the two P3HT layers are 3.72 Å apart. Unlike the P3HT

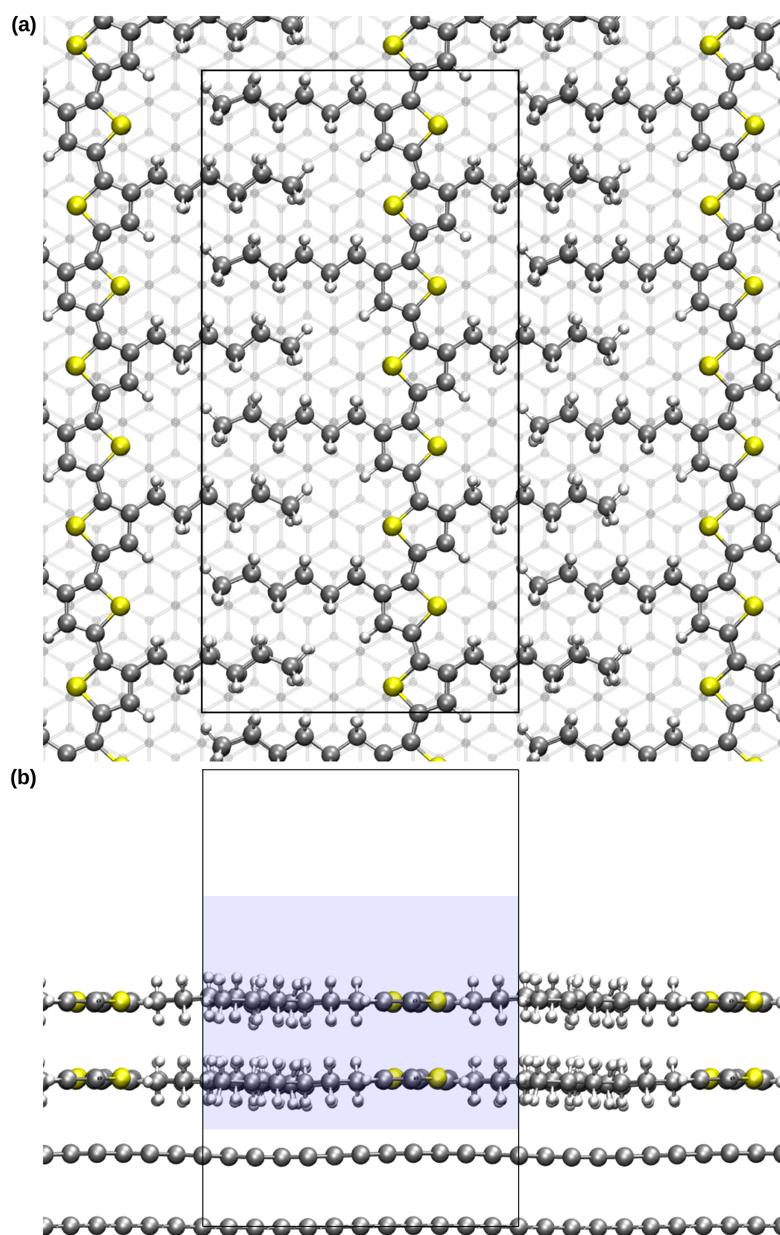

Figure 7.2: (a) Top and (b) side views of the ideal double-layer graphene/P3HT interface model. The shaded area in (b) represents the P3HT region of the computation cell, defined as the region extending from the midpoint between the top graphene and bottom P3HT layers to the midpoint of the vacuum region.

layers present at the ZnO/P3HT interface of Chapter 5, the polymer layers here do not display any significant rippling along the direction normal to the interface.

The use of parallel layers of planar graphene and P3HT in our models is justified by examining SEM images of films of solution-processable functionalised graphene (SPFGraphene) blended with P3HT [79], which reveal that the graphene sheets lie parallel to the P3HT in the blended matrix. The preparation of SPFGraphene is described in Ref. 79 and references therein. First, graphene sheets are oxidised with polar functional groups to generate graphene oxide (GO). Next, the GO is functionalised in order to make it hydrophilic and thus soluble in organic solvents. This functionalisation damages the π-conjugation of the graphene and inhibits charge mobility and charge transfer [158], leading to a degradation in device performance [79]. To counter this loss of performance, an annealing treatment can be applied in order to remove the functional groups and restore the π-conjugated structure of the SPFGraphene sheets [79] and thus greatly improving charge mobility [158]. The annealing process has also been shown to enhance the crystallinity and mobility of P3AT-based conjugated polymers [159], of which P3HT is one. Our models, which consist of pristine graphene layers and highly crystalline P3HT, should therefore be viewed as a SPFGraphene/P3HT interface post-annealing, with the functional groups removed, the conjugated structure of the graphene restored and the P3HT highly crystallised.

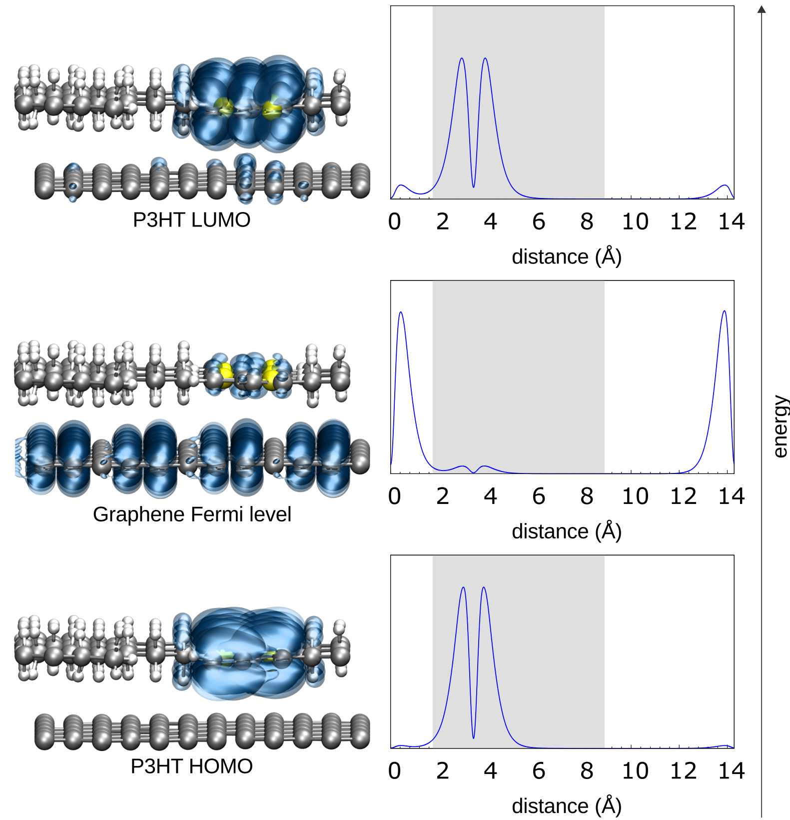

Figure 7.3: The wavefunctions for the 1L interface model, shown in increasing energy from bottom to top. The bottom panel shows the HOMO of the P3HT, the middle panel the Fermi level of the graphene, and the top panel the LUMO of the P3HT. The shaded areas represents the P3HT region of the computation cells, defined as the region extending from the midpoint between the graphene and P3HT layers to the midpoint of the vacuum region.

7.3 Interfacial Energy-Level Alignment

7.3.1 DFT Energy-Level Alignment

We identified the eigenvalues of the band extrema at the 1L and 2L interfaces by examining the planar-averaged wavefunctions, along the direction normal to the graphene surface, of their DFT eigenstates (see Figures 7.3 and 7.4). Those states with more than 75% of the $|\psi|^2$ density in the P3HT

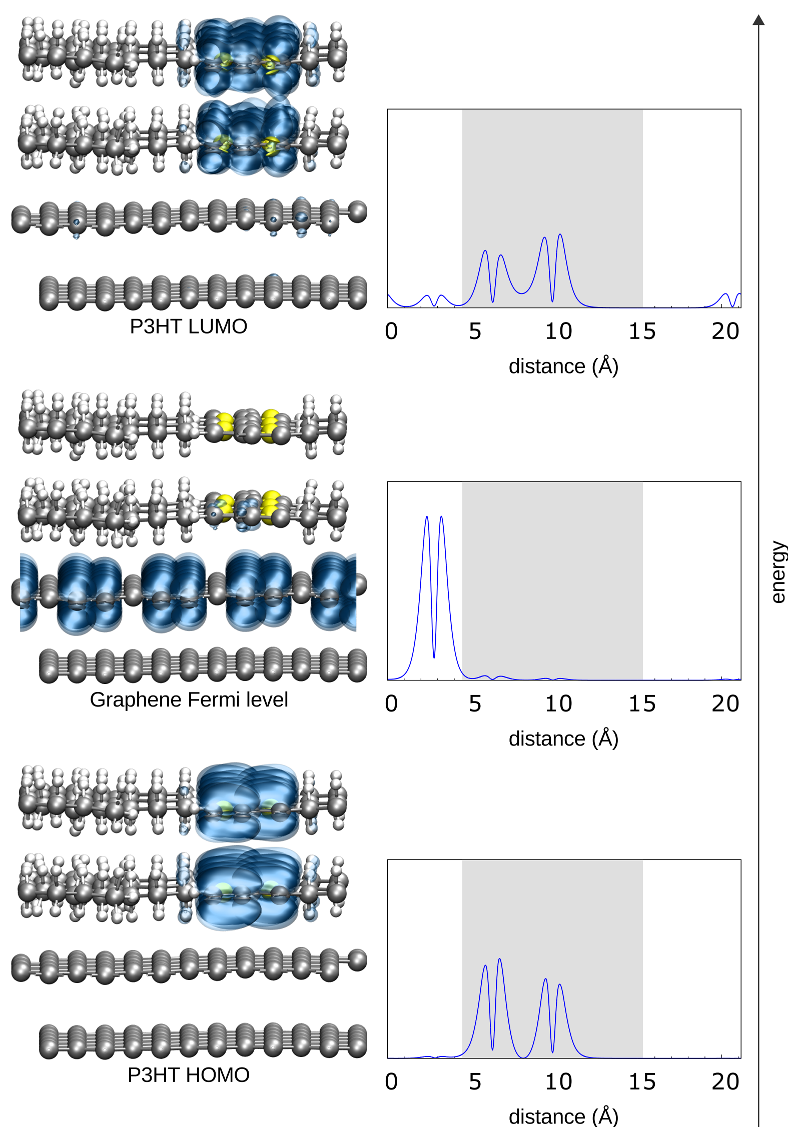

Figure 7.4: The wavefunctions for the 2L interface model, shown in increasing energy from bottom to top. The bottom panel shows the HOMO of the P3HT, the middle panel the Fermi level of the graphene, and the top panel the LUMO of the P3HT. The shaded areas represent the P3HT region of the computation cells, defined as the region extending from the midpoint between the top graphene and bottom P3HT layers to the midpoint of the vacuum region.

region of the unit cell were assigned to the polymer, while those with greater than 75% of the wavefunction in the graphene region were assigned to the

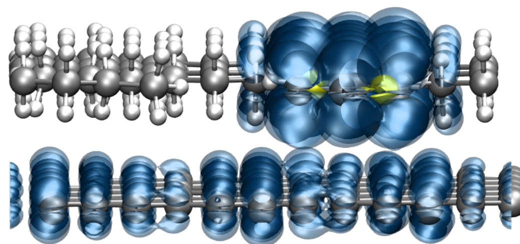

Figure 7.5: The $|\psi|^2$ density of a mixed state of the 1L interface. We note that the wavefunction is delocalised over both the graphene and the P3HT.

graphene. While these criteria are somewhat arbitrary, we note that, in practice, all states assigned exclusively to the P3HT or graphene demonstrate a $|\psi|^2$ density localisation of greater than 90%. All other states were deemed to be mixed states and were not assigned exclusively to either material. An example of suche a mixed state is shown in Figure 7.5, from which it can be seen that such states are delocalised over both materials. By identifying the character (i.e. P3HT or graphene) of the eigenstates and combining this knowledge with their corresponding eigenvalues, we were able to isolate the Fermi level of the graphene, and the HOMO and LUMO of the P3HT for both the 1L and 2L interface. We note that the DFT band gap of the P3HT at both the 1L and 2L interfaces is within less than 0.1 eV of the DFT bulk value. We further corroborated our assignments by examining the spatial wavefunctions of the identified band extrema, shown in Figures 7.3 and 7.4. From these plots we see that for both interfaces the state corresponding to the graphene Fermi level is localised on the graphene, while those corresponding to the HOMO and LUMO of the P3HT are localised on the polymer and demonstrate the expected π and π^* character, respectively.

The DFT eigenvalues of the graphene Fermi level and P3HT HOMO and

	KS [eV]	ΔH [eV]	Hybrid [eV]
$E_{\mathrm{f,1L}}$	-0.12	-	0.90
$\mathrm{LUMO_{1L}}$	0.84	0.76	2.61
$\mathrm{HOMO_{1L}}$	0.00	-1.02	0.00
$E_{\mathrm{g,P3HT,1L}}$	0.84	1.77	2.61
$E_{\mathrm{f,2L}}$	-0.33	-	0.71
$\mathrm{LUMO_{2L}}$	0.86	0.76	2.67
$\mathrm{HOMO_{2L}}$	0.00	-1.02	0.00
$E_{\mathrm{g,P3HT,2L}}$	0.86	1.81	2.67

Table 7.1: Energies of the graphene Fermi level and the P3HT HOMO and LUMO at the graphene/P3HT 1L and 2L interfaces. The energy levels under "KS" correspond to the DFT Kohn-Sham states at the interface. The values under "ΔH" are the hybrid-functional corrections to the DFT levels of bulk P3HT (with $\alpha_{\mathrm{P3HT}} = 0.367$). No hybrid functional correction for the Fermi level of graphene is reported since it varies negligibly with α (see text). The band gaps of P3HT at both interfaces are also reported. The zero of the energy axis is set to the HOMO level of the P3HT in all cases.

LUMO for both the 1L and 2L models are presented in Table 7.1. For both interfaces the DFT alignment is qualitatively incorrect and the Schottky-type heterojunction expected from the EA alignment is not reproduced (see Figure 7.6). Instead, both interfaces exhibit an alignment in which the Dirac point of the graphene is below the HOMO of the P3HT.

7.3.2 Application of Hybrid Functionals

We correct the DFT energy-level alignment shown in Figure 7.6 by applying the hybrid-functional corrections for P3HT derived in Chapter 5.3.2 to the eigenvalues of the polymer at the interface. We tested the effects of hybrid functionals on the Fermi level of graphene and found them to be minimal. Varying the fraction α of exact exchange from 0 to 0.5 changed the Fermi level

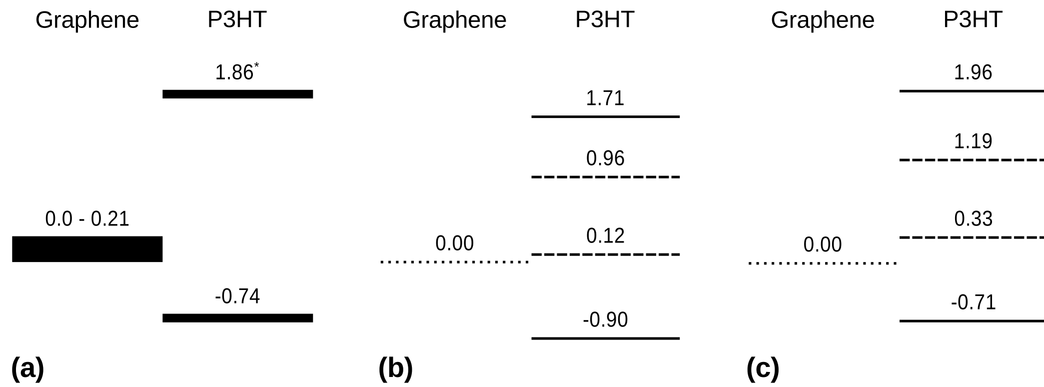

Figure 7.6: Energy-level alignment of the graphene/P3HT interfaces. The EA alignment is shown in (a) using the graphene Fermi levels for single- and double-layer graphene given in Ref. 160. The P3HT HOMO level is taken from Ref. 144, with the LUMO energy obtained using the quasiparticle gap of 2.6 eV from Ref. 142. The calculated energy-level alignments are also shown for the (b) 1L and (c) 2L interfaces. All energy levels in (a), (b) and (c) are in eV and have been referenced to their respective graphene Fermi levels for ease of comparison. In (b) and (c) the dotted lines represent the DFT/hybrid functional graphene Fermi level, the dashed lines indicate the DFT P3HT levels, and the solid lines are the hybrid functional P3HT levels.

(relative to the vacuum potential) by only 0.1 eV, as seen in Figure 7.7. We thus take 0.1 eV to be the upper bound on the uncertainty in the graphene Fermi level introduced by neglecting to apply hybrid-functional corrections to graphene in the 1L and 2L models. The hybrid-functional energy-level alignments of both the 1L and 2L interfaces are shown in Figure 7.6(b),(c). From this figure we see that the application of hybrid-functional eigenvalue corrections to the interfacial P3HT energy levels results in a Schottky-type band structure for both the 1L and 2L interfaces. The hybrid-functional corrections to P3HT, along with the final hybrid-functional energy levels, are shown in Table 7.1.

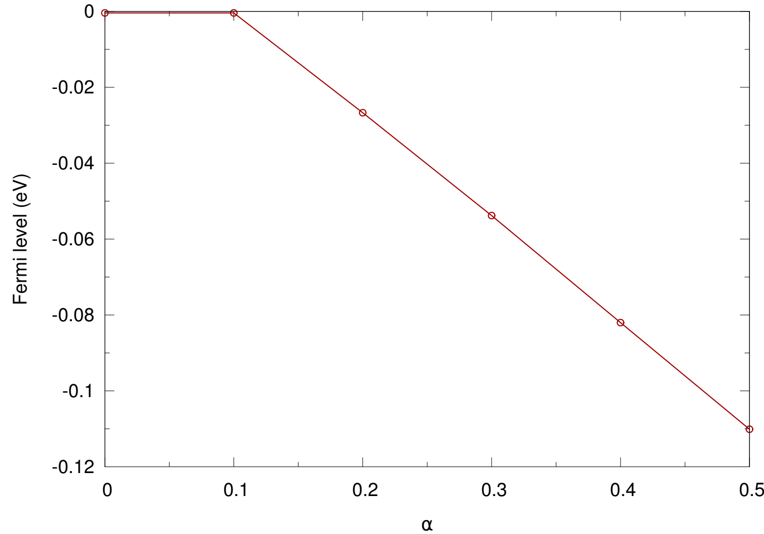

Figure 7.7: The variation of the Fermi level of graphene with the fraction α of exact exchange. The Fermi level of the standard DFT calculation corresponds to $\alpha = 0$.

7.4 Comparison with Experiment

7.4.1 Open-Circuit Voltage

The maximum V_{OC} of a graphene/P3HT interface corresponds to the difference between the work function of graphene and the HOMO of P3HT, as explained in Chapter 1.3.3. From Figure 7.6 we see that V_{OC} is 0.90 V and 0.71 V for the 1L and 2L interfaces, respectively. The values are in excellent agreement with the ~0.7-0.9 V range reported for annealed devices [79], for which many functional groups have been removed and whose

morphology more closely resembles our models. That the V_{OC} of the 2L interface is slightly higher than that of the 1L suggests that using a single layer of graphene could reduce the maximum achievable open-circuit voltage of the PV device. It is also interesting to compare our calculated open-circuit voltage with that predicted using the EA rule alignment. Using the P3HT ionisation potential (HOMO) level of Ref. 144 (5.2 eV) and the work functions of single- and double-layer graphene of Ref. 160 (4.25-4.46 eV), the EA rule energy-level alignment would predict a maximum V_{OC} of 0.74-0.95 eV (as shown in Figure 7.6). Alternatively, if we use the work function of SPF-Graphene [161] (4.5 eV), the predicted EA alignment V_{OC} is 0.7 eV. Both of these predictions are in very good agreement with our calculated range of 0.7-0.9 eV. Given the qualitatively incorrect DFT band alignments it is not possible to perform an electrostatic dipole analysis, as in the ZnO/P3HT and GaAs/P3HT models, without resorting to hybrid-functional calculations on the full interfaces. However, given the very close value of our calculated V_{OC} to the EA value predicted using pristine 1L and 2L graphene, we can reasonably assume that there is no significant interfacial electrostatic dipole and, accordingly, no appreciable ground state charge transfer upon formation of the graphene/P3HT interface. This assumption is in line with calculations performed on graphene/poly(para-phenylene) (PPP) interfaces, which show no net charge transfer between the polymer and the graphene [162]. Important to note is the significant "loss-in-potential" for this interface as compared with the ZnO/P3HT heterojunction, which operates at a negligible loss-in-potential.

7.4.2 Functionalised Graphene

Discrepancy between EA-predicted and Measured V_{OC} of SPFGraphene/P3HT Interfaces

As mentioned in the previous section, the V_{OC} predicted by the EA rule for interfaces using SPFGraphene is 0.7 eV, which is lower than the measured range of V_{OC} for fabricated non-annealed devices (0.7-1.1 eV) [79], which retain the functional groups of the SPFGraphene. In order to gain more insight into the discrepancy between the measured values and those predicted using the EA rule, we constructed a functionalised graphene/P3HT interface based on our 1L model. This model, shown in Figure 7.8 includes carbonyl (-C=0), epoxide (-C-O-C-) and hydroxyl (-C-OH) groups, as they feature heavily in the graphene oxide (GO) that is used to produce SPFGraphene [79, 163]. The concentration of functional groups in our model is in line with experimentally produced SPFGraphene [163]. Examining the optimised structure of the interface shown in Figure 7.8 we clearly observe a much stronger distortion of both the graphene and the P3HT as compared to the non-functionalised 1L interface illustrated in Figure 7.1. Distortion of the P3HT layers, as observed in Figure 7.1, can destroy the regioregularity of the polymer, which in turn can lower its HOMO level by 0.3 eV [164]. The EA-predicted energy-level alignment neglects any structural distortions caused by the formation of the interface and, as such, will not include a lowering of the HOMO level (and concomitant increase of the V_{OC}). It is therefore to be expected that the open-circuit voltage predicted using the EA rule would be lower than the measured value.

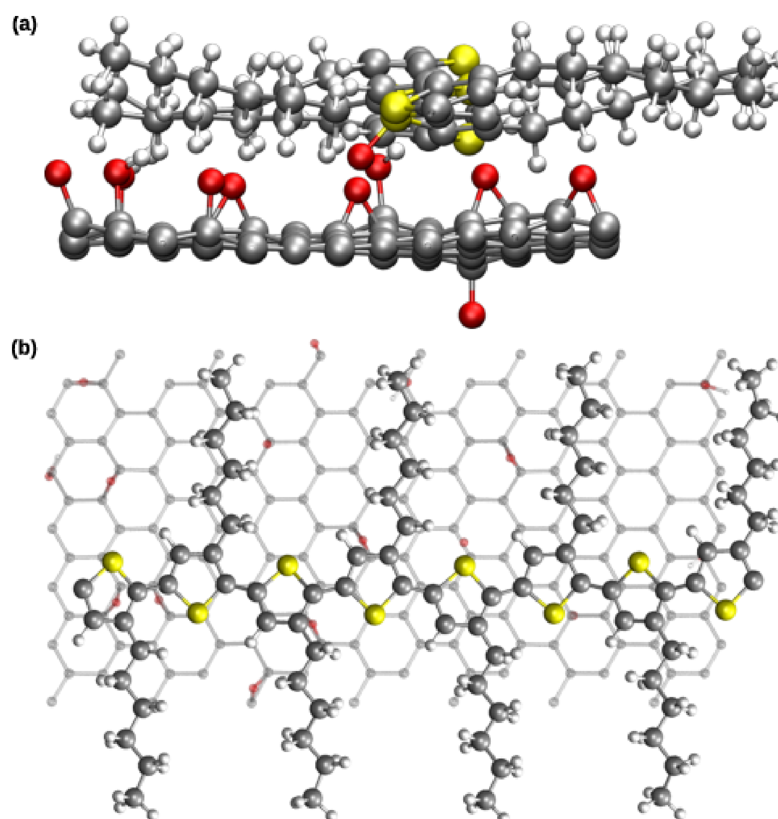

Figure 7.8: A possible interface between functionalised graphene and P3HT as viewed from (a) the side and (b) the top. The functionalised graphene includes epoxide and carbonyl groups in a concentration consistent with Ref. 163.

The calculated electronic structure of the functionalised 1L interface reveals that the Fermi level of the functionalised graphene at the interface is ∼0.2 eV higher with respect to the HOMO of P3HT when compared to the values at the 1L interface. Such an observation suggests that the presence of the functional groups could create a small electrostatic dipole (with correspondingly small dipole potential step) that would act to modify the open-circuit voltage, as described in Chapter 5.4.2, consistent with experiments conducted on SWNTs/P3HT interfaces [70]. We stress that the model

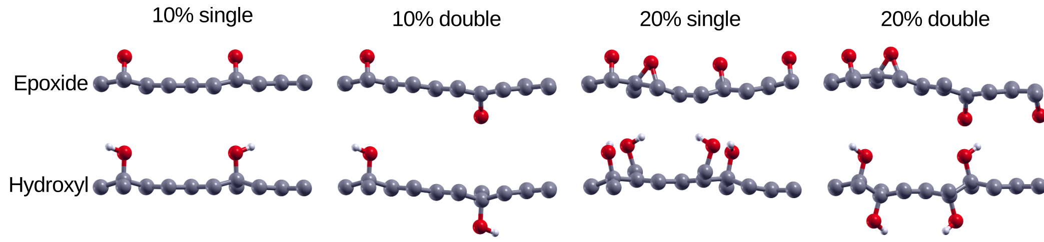

Figure 7.9: Unit cells of various functionalised graphene models. The top row shows the unit cell of pristine graphene. Models of graphene functionalised with epoxide groups are shown in the middle row. Models of graphene functionalised with hydroxyl groups are shown in the bottom row.

shown in Figure 7.8 is only one of many possible configurations for the interface between SPFGraphene and P3HT, and that a different model might provide a dipole of different sign. However, this model should provide an estimate of the change in V_{OC} expected from the introduction of functional groups.

Discrepancy Between Measure V_{OC} of Annealed and Non-Annealed Devices

The open-circuit voltages of annealed and non-annealed devices from Ref. 79 are 0.7-0.9 eV and 0.7-1.1 eV, respectively. We have shown that the non-annealed devices may exhibit a small electrostatic dipole and feature a heavily distorted P3HT layer. As noted above, both of these effects tend to modify V_{OC}.

We explored this discrepancy further by examining models of graphene functionalised using epoxide and hydroxly groups, shown in Figure 7.9. We modelled configurations of graphene oxide with epoxide and hydroxyl concentrations of 10% and 20%. For each concentration the functional groups were

configuration	ΔE_{f} [eV]
Pristine	0.00
Epoxide 10% single	0.53
Epoxide 10% double	0.61
Epoxide 20% single	0.77
Epoxide 20% double	0.98
Hydroxyl 10% single	0.43
Hydroxyl 10% double	0.41
Hydroxyl 20% single	0.28
Hydroxyl 20% double	-0.06

Table 7.2: The offset of the highest occupied levels of the functionalised graphene configurations with respect to the Dirac point of pristine graphene. Because a dipole correction was used in determining the vacuum levels, in each case there are two vacuum levels, as explained in Chapter 3.7. The values shown in this table are the averaged quantities. The complete data are presented in Appendix A. The vacuum levels have an error of ±0.05 Ry (∼0.07 eV).

added in both a single-sided and double-sided manner. A pristine graphene sheet was also considered for comparison.

After structural optimisation of the configurations, we examined the highest occupied levels of each of the models. In order to compare the highest occupied levels of the various configurations, we referenced each of them to the vacuum levels of their respective total potentials, as described in Chapter 3.5. The vacuum-referenced highest occupied levels for all nine configurations are are shown in Table 7.2. In all but one case, the Fermi level of the functionalised graphene configurations is raised with respect to pristine graphene. It must be noted, however, that there is a large variation the change of the Fermi level (-0.06–0.98 eV) and in fabricated SPFGraphene, which includes many such groups in various concentrations, the effect is likely to be averaged. In any case, based on the data shown in Table 7.2, it seems

plausible that SPFGraphene will generally have a higher Fermi level than pristine graphene. Correspondingly, non-annealed devices, with the SPF-Graphene sheet left largely intact, are likely to have a higher graphene Fermi level, and therefore a higher open-circuit voltage, than annealed devices, in accord with the measured V_{OC} of Ref. 79.

7.5 Conclusions

In this chapter we have explored the graphene/P3HT interface using both single- (1L) and double-layered (2L) models. In both cases we note a less disorted polymer at the interface with respect to both the ZnO/P3HT and GaAs/P3HT interfaces.

The DFT energy-level alignment is qualitatively incorrect and does not reproduce the expected Schottky-type heterojunction. Applying the hybrid-functional corrections derived in Chapter 5.3.2 to the P3HT levels at the interfaces produces a qualitatively correct alignment and a P3HT band gap matching the quasiparticle gap of 2.6 eV [142]. Hybrid functionals have minimal effect on the Fermi level of graphene and create a maximum uncertainty in its energy of 0.1 eV. We observe no significant electrostatic dipole at either the 1L or 2L interfaces, as evidenced by the agreement between our calculated V_{OC} (0.71-0.90 eV) with that of the electron affinity rule prediction of 0.74-0.95 eV for single- and double-layered pristine graphene interfaces. Future work should focus on confirming, in a quantitative manner, the absence of a dipole at these interfaces.

Since fabricated devices are made with SPFGraphene, it is important to

examine the effect of the functional groups at the interface. The discrepancy between the EA rule prediction of the $V_{\rm OC}$ at the SPFGraphene/P3HT interface (0.7 eV) and the values measured experimentally (0.7-1.1 eV). Our functionalised graphene 1L model shows a very strong distortion of the polymer that could lead to a lowering of its HOMO level by several tenths of an eV. Furthermore, an energy-level alignment analysis shows the Fermi level of the graphene at $\sim$0.2 eV different from the corresponding level at the pristine graphene (1L) interface, suggesting the presence of a small interfacial dipole potential step brought about by the functional groups. Taken together, these two factors might explain why the EA rule underestimates the $V_{\rm OC}$ at the SPFGraphene/P3HT heterojunction. The observations noted in this chapter are potentially important for device optimisation since they suggest that the presence of functional groups could raise the $V_{\rm OC}$ of the PV device. This, of course, must be balanced with the corresponding lowering of charge mobility in the graphene [158], which can reduce the short-circuit current and increase charge carrier recombination across the interface.

We stress that the SPFGraphene/P3HT interface modelled in this chapter is only one of many possible configurations. Accordingly, the conclusions drawn here must be verified by future study, for example studying in more detail the effect of P3HT distortion on its HOMO and LUMO levels. Similarly, the functionalised graphene models studied here do not represent a statistically significant set of configurations. Further work must be undertaken to confirm both the general trend and magnitude of the shift of the highest occupied level of graphene upon functionalisation.

Chapter 8

Conclusions

8.1 Summary

The goal of this project was to examine the energy-level alignment at the interfaces of organic and hybrid organic-inorganic photovoltaic devices. As we saw in Chapter 1, organic and hybrid organic-inorganic PV devices offer the possibility of low-cost, large-area renewable energy. To date, however, the open-circuit voltages and short-circuit currents remain low and, as a consequence, device efficiencies are not sufficiently high to drive widespread commercial adoption. By exploring the energy-level alignment at PV interfaces from first principles, we hope to gain a better understanding of how the atomic-scale properties of the interface affect V_{OC}, while simultaneously creating a framework for future investigations.

Density functional theory provides an ideal avenue for the exploration of atomic-scale interfaces and allows us to determine realistic atomic structure configurations and electronic structure properties of the systems of interest.

In Chapter 2 we presented the theoretical framework necessary for modelling the electronic structure of materials from first principles. We introduced DFT in the planewave and pseudopotential formulation that was used for the calculations presented in this thesis. We also examined the band gap problem of DFT, along with the hybrid functional approach that allows us to practically overcome the limitations associated with the underestimation of the gaps. In Chapter 3 considerations for practical DFT and hybrid functional calculations were introduced. Methods for comparing the eigenvalues of different calculations, determining the energy-level alignment of an interface, and assessing the impact of interfacial dipoles were explored, providing a strong basis on which to conduct the research presented in the later chapters. We also discussed the charge neutrality level and its relationship to the electrostatic dipole and energy-level alignment.

In Chapter 4 we calculated the bulk atomic and electronic structure properties of ZnO, GaAs, graphene and P3HT. While the DFT electronic structures of these materials predictably differ from the experimental literature, there is in general a very good agreement with other DFT studies. The structural properties of ZnO, GaAs, and graphene were all faithfully reproduced, while the range of bulk parameters calculated for P3HT are in good agreement with both the experimental and theoretical literature.

The ZnO/P3HT hybrid organic-inorganic PV interface was examined in detail in Chapter 5 and represents the largest first-principles model of this system to date. Using DFT we were able to determine a likely binding configuration for the polymer on top of the ZnO surface and to generate a qualitatively correct energy-level alignment between the two materials. We

then turned to hybrid functionals and applied a variation of the scheme of Ref. 102 in order to correct the underestimation of the band gaps and to arrive at a quantitatively realistic alignment for the ideal interface. The V_{OC} of $\sim$2 V that we calculated is significantly larger than that predicted by the electron affinity rule or measured in experimental devices. The discrepancy between our V_{OC} and the EA prediction is assigned to the presence of a significant and heretofore unquantified interfacial electrostatic dipole. The low experimental voltages are likely due to a combination of ZnO defects and recombination effects.

We have also demonstrated how DFT can be used to interpret experimental data. In Chapter 6 we examined the hybrid organic-inorganic GaAs/P3HT photovoltaic interface. Using the methods established in Chapter 5 we calculated a significant charge transfer, and hence electrostatic dipole, at both the pristine and oxidised GaAs/P3HT interfaces. These observations were used in Ref. 59 in order to corroborate experimental evidence that the reduced PL lifetimes observed in GaAs/P3HT photovoltaic devices is due to charge transfer from the polymer to the semiconductor.

As the study of graphene has intensified in recent years, so too has its application to photovoltaic devices. Organic PV devices using graphene as an acceptor have been demonstrated, however the measured efficiencies remain low. In Chapter 7 we calculated V_{OC} for both a single- and double-layer ideal graphene/P3HT interface using a combination of DFT and hybrid functionals. The range of V_{OC} so determined is 0.7-0.9 V, in agreement with the voltage predicted for the same interface using the EA rule. The agreement between the first-principles and EA open-circuit voltage suggests that, unlike

the ZnO/P3HT and GaAs/P3HT interfaces, there is possibly no significant electrostatic dipole present at the graphene/P3HT interface. Given the inability of DFT to properly describe the qualitative energy-level alignment, however, further work must be done in order to confirm this supposition.

We also explored the discrepancy between the measured open-circuit voltage of functionalised SPFGraphene/P3HT PV devices with that predicted by the EA rule. It has been noted in the literature that the EA value is lower than that measured in fabricated devices. Our functionalised graphene/P3HT model interface demonstrates a strong distortion of the polymer layer due to the presence of the functional groups. While we have only examined one of many possible such configurations, our finding suggests that polymer distortion, not considered in the EA rule, could contribute to the higher voltage observed in experiment. Furthermore, vis-à-vis the unfunctionalised interface, the highest occupied level of graphene at the functionalised interface is raised with respect to the P3HT HOMO, indicating the possible presence of an interfacial dipole.

Functionalised graphene was explored in isolation and was found to have, in general, a higher highest occupied level than pristine graphene. From this we can infer that annealed SPFGraphene/P3HT devices, whose functional groups have largely been removed, should generate a lower V_{OC} than their non-annealed counterparts. This observation is in agreement with experiment.

8.2 Outlook

We have demonstrated throughout this thesis that first-principles materials modelling can not only be used to interpret experimental data but that it can also provide insights into the physics of interfaces that would be difficult, if not impossible, to gain via experiment alone. The ability to create ideal, defect-free interfaces and to construct a detailed picture of the electronic structure of them is an invaluable technique for advancing the understanding and improving the design of organic and organic-inorganic PV devices. These benefits, however, can also prove to be limitations. Periodic boundary conditions and limited computing power prevent the first-principles study of truly representative systems, complete with defects, grain boundaries, impurities and other non-idealities. In the short term, therefore, progress depends largely on the experiments involving pristine interfaces to which our current models could be directly compared. Additionally, the models we have studied here serve as a platform on which to build more sophisticated systems that can be used to explore PV devices in more detail. It is hoped that the insights gained in modelling the complex interactions between polymers and semiconductors at their interfaces can be applied to new systems in an effort to predict their behaviour and guide experimental progress.

Further afield, as computational power grows and as ever more sophisticated software algorithms appear, the scale of the systems we are able to study will certainly increase. Using first-principles methods to study the systems presented in this thesis would not have been possible even a decade ago. We can only imagine, then, what the next decade has in store and hope

for the advent of truly predictive first-principles modelling techniques.

Appendix A

Computational Details

A.1 General Notes on the Computational Details

All DFT calculations were performed using the `Quantum ESPRESSO` software package [165]. `Quantum ESPRESSO` is an open-source planewaves, pseudopotential package that comprises many DFT codes and post-processing tools. With these codes we can perform structural relaxations and SCF calculations, and output band structure and DOS plots. The post-processing tools are able to generate three-dimensional and planar-averaged wavefunction, charge density and potential plots. `Quantum ESPRESSO` also features a hybrid functional implementation that permits the variation of the exact exchange mixing fraction α.

In structural relaxation calculations the forces on atoms were converged to less than 10 meV/Å. All relaxations performed for this thesis use ultrasoft

pseudopotentials within Perdew-Zunger (PZ) [85] parameterisation of the LDA. These pseudopotentials were downloaded from the `Quantum ESPRESSO` website and were tested to ensure their compatibility with the systems of interest in this thesis (see Chapter 4). Unless stated otherwise, electronic structure calculations use norm-conserving GGA pseudopotentials. We choose to use the parameterisation of Perdew, Burke, and Ernzerhof (PBE) [86]. These PBE pseudopotentials were generated using the `FHI98pp` program [98] and were tested for transferability (see Chapter 3.3) and to ensure good reproduction of the lattice parameters discussed in Chapter 4.

In order to maintain consistency with the DFT electronic structure, we use hybrid functionals based on PBE, referred to as PBE0 [166]. PBE0 hybrid functionals use a fixed mixing fraction $\alpha = 0.25$. Following the method of Ref. 102, however, we vary α in order to match experimental band gaps.

A.2 ZnO

Bulk wurtzite ZnO was relaxed using a $8 \times 8 \times 8$ **k**-point sampling of the Brillouin zone. The sampling for electronic structure calculations was identical. The unit cell consists of two Zn and two O atoms. The kinetic energy cutoff of the PZ pseudopotentials was set to 35 Ry, while the cutoff for PBE pseudopotentials was set to 100 Ry.

The $(10\bar{1}0)$-terminated slab of ZnO features 240 atoms and 1080 electrons. Brillouin zone sampling was restricted to the Γ point for both structural relaxation and electronic structure calculations. The transverse area of the slab is 15.93×15.46 Å^2. The slab is periodic in the plane parallel to the

surface, and periodic replicas in the direction normal to the interface are separated by 10 Å.

A.3 GaAs

Because hybrid functional corrections were not used for the GaAs/P3HT interfaces in Chapter 6, electronic structure calculations were performed at the LDA level. Bulk GaAs was relaxed using a $8 \times 8 \times 8$ **k**-point sampling. The electronic structure used the same sampling. The kinetic energy cutoff for the ultrasoft PZ pseudopotentials was set to 35 Ry.

The pristine wurtzite $(10\bar{1}0)$ slab has 128 atoms and 1152 electrons. The oxidised slab has 1200 electrons and 136 atoms. Both interfaces were described using Γ-point sampling for structural relaxations and electronic structure calculations. Period replicas normal to the interface were separated by 10 Å.

A.4 Graphene

The graphene unit cell analysed in Chapter 4.3 features 2 C atoms. The Brillouin zone was sampled via $300 \times 300 \times 1$ **k**-points and a PBE pseudopotential with 60 Ry kinetic energy cutoff was used. The cell is periodic along the sheet and 13 Å of vacuum separate each sheet from its periodic image. The **k**-point sampling for the DOS calculation was also set to $300 \times 300 \times 1$.

A.5 P3HT

Three P3HT configurations were studied in Chapter 4.4, each with 50 atoms. These three configurations vary in terms of their initial alkyl side chain interdigitation. In Configuration I, the alkyl chains were not interdigitated. The interdigitation in Configuration III was set to be as high as possible. Configuration II was constructed to have an initial interdigitation halfway between Configurations I and III. All three configurations were relaxed using ultrasoft PZ pseudopotentials with a 35 Ry kinetic energy cutoff. The Brillouin zone was sampled via $8 \times 2 \times 2$ **k**-points. The electronic structure calculations used the same **k**-point sampling and PBE pseudopotentials with a 60 Ry cutoff.

A.6 ZnO/P3HT

Though the LDA does not explicitly include dispersion forces it has been shown to produce crystalline structures of P3HT in agreement with experiment [129], as well as physisorption geometries for bithiophene on ZnO consistent with second-order Møller-Plesset (MP2) perturbation methods [112]. The use of LDA pseudopotentials for the relaxation of the ZnO/P3HT interface is therefore reasonable. Valence electron kinetic energy cutoffs for wavefunctions and charge density were set to 35 Ry and 320 Ry, respectively. The Brillouin Zone of the computational unit cell was restricted to sampling at the Γ point, and periodic replicas were separated by 9.5 Å of vacuum along the direction normal to the interface. The unit cell contains 540

atoms and 2880 electrons. The transverse area of the cell is 15.93×15.46 Å^2.

For the electronic structure, valence electron kinetic energy cutoffs for wavefunctions and charge density were set to 100 Ry and 400 Ry, respectively. Hybrid functional calculations on bulk ZnO and P3HT were carried out using variations of the PBE0 hybrid density functional [166] and were sampled, respectively, at $8 \times 8 \times 8$ ($4 \times 4 \times 4$) and $4 \times 4 \times 4$ ($2 \times 2 \times 2$) **k**-point grids (auxiliary **q**-point grids) of the Brillouin Zone. The band offsets were calculated at the PBE and PBE0 level. In addition to validating this approach on the thiophene/P3HT test system (Chapter 5.3.2) we note that the electron density undergoes only a minor redistribution from PBE to PBE0 [102]. As a result, the offsets calculated at both levels are expected to be very close.

In the optimised model of the nanowire, the Zn-O bond length decreased from 1.96 Å at the centre of the nanorod to 1.91 Å at the surface. For both atomic- and electronic-structure calculations, the one-dimensional Brillouin Zone along the nanorod axis was sampled by means of 8 inequivalent points. The lateral separation between the rod and its periodic replicas was set to 10 Å.

A.7 GaAs/P3HT

All structural relaxations and electronic structure calculations were carried out with sampling of the Brillouin Zone at Γ. A mixture of ultrasoft PZ (H, C, S) and norm-conserving PZ (Ga, As) pseudopotentials were used to describe core-valence electron interactions. Valence electronic wavefunctions

and charge density were described using a plane wave basis with kinetic energy cutoffs of 70 Ry and 350 Ry, respectively.

The computational unit cell of the pristine interface contains 428 atoms and 1872 electrons, while that of the oxidised interface has 436 atoms and 1920 electrons. The transverse area of both interfaces is identical to that of the ZnO/P3HT interface. Periodic images normal to the surface were separated by 10 Å.

A.8 Graphene/P3HT

In atomic relaxation calculations, the kinetic energy cutoffs were set to 35 Ry and 350 Ry, respectively, for wavefunctions and charge density. The Brillouin-Zone of the computational cell of the 1L interface was sampled with a $2 \times 2 \times 1$ grid of $\mathbf{k}$-points, while that of the 2L interface was sampled exclusively at the Γ-point.

Our test calculations have shown that the LDA reproduces experimental inter-layer graphite distances [127, 167]. Furthermore, as in P3HT on ZnO, P3HT on graphene displays strong $\pi - \pi$ interactions, and we therefore use the same justification here for neglecting Van der Waals corrections.

For electronic structure calculations wave functions were cut off at a kinetic energy of 60 Ry while the charge density cutoff was set to 240 Ry. The electronic charge density of both interfaces was determined via Brillouin Zone sampling of $2 \times 2 \times 1$ k-points, while the eigenvalues used a sampling of $4 \times 4 \times 1$ k-points. The appropriateness of these Brillouin Zone samplings was verified by examining the DOS of both interfaces; in each case the corrected

linear dispersion of graphene states around the Fermi level was observed.

The 1L interface contains 368 atoms and 1152 electrons, while the 2L interface consists of 736 atoms and 2304 electrons. Periodic replicas along the direction normal to the interface were separated by 10 Å.

A.8.1 Functionalised Graphene

In order to compare the Dirac-point offsets of the various configurations we aligned their respective vacuum levels, as described in Chapter 3.5. However, to obtain a definite vacuum level we applied the dipole correction of Chapter 3.7, resulting in two vacuum levels through which we can align the offsets (see Figure 3.2). These two alignments are shown in Table A.1 along with their average, which is the quantity presented in Table 7.2.

configuration	$\Delta E_{\mathrm{f},1}$ [eV]	$\Delta E_{\mathrm{f},2}$ [eV]	$\Delta E_{\mathrm{f,avg}}$ [eV]
Pristine	0.00	0.00	0.00
Epoxide 10% single	1.02	0.04	0.53
Epoxide 10% double	0.61	0.61	0.61
Epoxide 20% single	1.63	-0.10	0.77
Epoxide 20% double	0.95	1.00	0.98
Hydroxyl 10% single	0.54	0.31	0.43
Hydroxyl 10% double	0.41	0.41	0.41
Hydroxyl 20% single	0.25	0.31	0.28
Hydroxyl 20% double	-0.06	-0.06	-0.06

Table A.1: The offset of the highest occupied levels of the functionalised graphene configurations with respect to the Dirac point of pristine graphene. Because a dipole correction was used, as described in Chapter 3.7, we align the various configurations to two vacuum levels, shown in the second and third columns. The last column is the average of these two values and is the data presented in Table 7.2. The vacuum levels have an error of ± 0.05 Ry ($\sim$0.07 eV).

References

[1] International Energy Agency, Four energy policies can keep the 2 °C climate goal alive. 2013; article published online at http://www.iea.org/newsroomandevents/pressreleases/2013/june/name,38773,en.html.

[2] International Energy Agency, *Redrawing the Energy-Climate Map: World Energy Outlook Special Report*; 2013.

[3] Greenpeace, *Solar Generation 6*; 2010.

[4] UK Department of Energy and Climate Change, *UK Energy in Brief 2012*; 2013.

[5] Kippelen, B.; Brédas, J.-L. *Energy Environ. Sci.* **2009**, *2*, 251.

[6] Shockley, W.; Queisser, H. J. *J. Appl. Phys.* **1961**, *32*, 510.

[7] The Economist, Sunny uplands. 2012; article published online at http://www.economist.com/news/21566414-alternative-energy-will-no-longer-be-alternative-sunny-uplands.

[8] Xue, J. *Polym.Rev.* **2010**, *50*, 411.

[9] Brabec, C. J. *Sol. Energ. Mat. Sol. Cells* **2004**, *83*, 273.

[10] van der Horst, J.-W.; Bobbert, P. A.; Michels, M. A. J.; Bassler, H. *J. Chem. Phys.* **2001**, *114*, 6950.

[11] Brabec, C. J., Dyakonov, V., Parisi, J., Sariciftci, N. S., Eds. *Organic Photovoltaics: Concepts and Realization*; Springer, 2003.

[12] Huynh, W. U.; Dittmer, J. J.; Alivisatos, A. P. *Science* **2002**, *295*, 2425.

[13] Milliron, D. J.; Gur, I.; Alivisatos, A. P. *MRS Bull.* **2005**, *30*, 41.

[14] Günes, S.; Sariciftci, N. S. *Inorg. Chim. Acta* **2008**, *361*, 581.

[15] McGehee, M. D. *MRS Bull.* **2009**, *34*, 95.

[16] Nelson, J. *The Physics of Solar Cells*; Imperial College Press, 2003.

[17] Schilinsky, P.; Waldauf, C.; Brabec, C. J. *Appl. Phys. Lett.* **2002**, *81*, 3885.

[18] Yu, G.; Gao, J.; Hummelen, J. C.; Wudl, F.; Heeger, A. J. *Science* **1995**, *270*, 1789.

[19] Brabec, C. J.; Gowrisanker, S.; Halls, J. J. M.; Laird, D.; Jia, S.; Williams, S. P. *Adv. Mat.* **2010**, *22*, 3839.

[20] Parker, I. D. *J. Appl. Phys.* **1994**, *75*, 1656.

[21] Brabec, C. J.; Cravino, A.; Meissner, D.; Sariciftci, N. S.; Fromherz, T.; Rispens, M. T.; Sanchez, L.; Hummelen, J. C. *Adv. Funct. Mater.* **2001**, *11*, 374.

[22] Brillson, L. *Surf. Sci. Rep.* **1982**, *2*, 123.

[23] Scharber, M. C.; Mühlbacher, D.; Koppe, M.; Denk, P.; Waldauf, C.; Heeger, A.; Brabec, C. *Adv. Mater.* **2006**, *18*, 789.

[24] Anderson, R. L. *IBM J. Res.Dev.* **1960**, *4*, 283.

[25] Hsu, J. W. P.; Lloyd, M. T. *MRS Bull.* **2010**, *35*, 422.

[26] Vayssieres, L. *Adv. Mater.* **2003**, *15*, 464.

[27] Sirringhaus, H.; Brown, P. J.; Friend, R. H.; Nielsen, M. M.; Bechgaard, K.; Langeveld-Voss, B. M. W.; Spiering, A. J. H.; Janssen, R. A. J.; Meijer, E. W.; Herwig, P.; de Leeuw, D. M. *Nature* **1999**, *401*, 685.

[28] Ravirajan, P.; Peiró, A. M.; Nazeeruddin, M. K.; Graetzel, M.; Bradley, D. D. C.; Durrant, J. R.; Nelson, J. *J. Phys. Chem. B* **2006**, *110*, 7635.

[29] Olson, D. C.; Shaheen, S. E.; Collins, R. T.; Ginley, D. S. *J. Phys. Chem. C* **2007**, *111*, 16670.

[30] Olson, D. C.; Shaheen, S. E.; White, M. S.; Mitchell, W. J.; van Hest, M. F. A. M.; Collins, R. T.; Ginley, D. S. *Adv. Funct. Mater.* **2007**, *17*, 264.

[31] Monson, T. C.; Lloyd, M. T.; Olson, D. C.; Lee, Y.; Hsu, J. W. P. *Adv. Mater.* **2008**, *20*, 4755.

[32] Olson, D. C.; Lee, Y.; White, M. S.; Kopidakis, N.; Shaheen, S. E.; Ginley, D. S.; Voigt, J. A.; Hsu, J. W. P. *J. Phys. Chem. C* **2008**, *112*, 9544.

[33] Spoerke, E. D.; Lloyd, M. T.; McCready, E. M.; Olson, D. C.; Lee, Y.; Hsu, J. W. P. *Appl. Phys. Lett.* **2009**, *95*, 213506.

[34] Beek, W. J. E.; Wienk, M. M.; Janssen, R. A. J. *Adv. Funct. Mater.* **2006**, *16*, 1112.

[35] Moet, D. J. D.; Koster, L. J. A.; de Boer, B.; Blom, P. W. M. *Chem. Mater.* **2007**, *19*, 5856.

[36] Wang, M.; Wang, X. *Sol. Energ. Mat. Sol. Cells* **2008**, *92*, 766.

[37] Oosterhout, S. D.; Wienk, M. M.; van Bavel, S. S.; Thiedmann, R.; Koster, L. J. A.; Gilot, J.; Loos, J.; Schmidt, V.; Janssen, R. A. J. *Nat. Mater.* **2009**, *8*, 818.

[38] Bouclé, J.; Snaith, H. J.; Greenham, N. C. *J. Phys. Chem. C* **2010**, *114*, 3664.

[39] Olson, D. C.; Piris, J.; Collins, R. T.; Shaheen, S. E.; Ginley, D. S. *Thin Solid Films* **2006**, *496*, 26.

[40] Peiró, A. M.; Ravirajan, P.; Govender, K.; Boyle, D. S.; O'Brien, P.; Bradley, D. D. C.; Nelson, J.; Durrant, J. R. *J. Mater. Chem.* **2006**, *16*, 2088.

[41] Greene, L.; Law, M.; Yuhas, B.; Yang, P. *J. Phys. Chem. C* **2007**, *111*, 18451.

[42] Olson, D. C.; Lee, Y.; White, M. S.; Kopidakis, N.; Shaheen, S. E.; Ginley, D. S.; Voigt, J. A.; Hsu, J. W. P. *J. Phys. Chem. C* **2007**, *111*, 16640.

[43] Lee, Y.; Lloyd, M. T.; Olson, D. C.; Grubbs, R. K.; Lu, P.; Davis, R. J.; Voigt, J. A.; Hsu, J. W. P. *J. Phys. Chem. C* **2009**, *113*, 15778.

[44] Briseno, A. L.; Holcombe, T. W.; Boukai, A. I.; Garnett, E. C.; Shelton, S. W.; Fréchet, J. J. M.; Yang, P. *Nano Lett.* **2010**, *10*, 334.

[45] Adikaari, A. A. D. T.; Dissanayake, D. M. N. M.; Silva, S. R. P. *IEEE J. Sel. Top. Quantum Electron.* **2010**, *16*, 1595.

[46] Ren, S. Q.; Zhao, N.; Crawford, S. C.; Tambe, M.; Bulovic, V.; Gradečak, S. *Nano Lett.* **2011**, *11*, 408.

[47] Ginger, D. S.; Greenham, N. C. *Phys. Rev. B* **1999**, *59*, 10622.

[48] Dayal, S.; Reese, M. O.; Ferguson, A. J.; Ginley, D. S.; Rumbles, G.; Kopidakis, N. *Adv. Funct. Mater.* **2010**, *20*, 2629.

[49] Novotny, C. J.; Yu, E. T.; Yu, P. K. L. *Nano Lett.* **2008**, *8*, 775.

[50] Cui, D. H.; Xu, J.; Zhu, T.; Paradee, G.; Ashok, S.; Gerhold, M. *Appl. Phys. Lett.* **2006**, *88*, 183111.

[51] Law, M.; Greene, L. E.; Johnson, J. C.; Saykally, R.; Yang, P. D. *Nat. Mater.* **2005**, *4*, 455.

[52] Schierhorn, M.; Boettcher, S. W.; Peet, J. H.; Matioli, G. C., E.and Bazan; Stucky, G. D.; Moskovits, M. *ACS Nano* **2010**, *4*, 6132.

[53] Lin, Y. Y.; Chu, T. H.; Li, S. S.; Chuang, C. H.; Chang, C. H.; Su, W. F.; Chang, C. P.; Chu, M. W.; Chen, C.-W. *J. Am. Chem. Soc.* **2009**, *131*, 3644.

[54] Parkinson, P.; Joyce, H. J.; Gao, Q.; Tan, H. H.; Zhang, X.; Zou, J.; Jagadish, C.; Herz, L. M.; Johnston, M. B. *Nano Lett.* **2009**, *9*, 3349.

[55] Haight, R.; Sekaric, L.; Afzali, A.; Newns, D. *Nano Lett.* **2009**, *9*, 3165.

[56] Demichel, O.; Calvo, V.; Besson, A.; Noe, P.; Salem, B.; Pauc, N.; Oehler, F.; Gentile, P.; Magnea, N. *Nano Lett.* **2010**, *10*, 2323.

[57] Yong, C. K.; Joyce, H. J.; Lloyd-Hughes, J.; Gao, Q.; Tan, H. H.; Jagadish, C.; Johnston, M. B.; Herz, L. M. *Small* **2012**, *8*, 1725.

[58] Lunt, S. R.; Ryba, G. N.; Santangelo, P. G.; Lewis, N. S. *J. Appl. Phys.* **1991**, *70*, 7449.

[59] Yong, C. K.; Noori, K.; Gao, Q.; Joyce, H. J.; Tan, H. H.; Jagadish, C.; Giustino, F.; Johnston, M. B.; Herz, L. M. *Nano Letters* **2012**, *12*, 6293.

[60] Chen, H.-Y.; Hou, J.; Zhang, S.; Liang, Y.; Yang, G.; Yang, Y.; Yu, L.; Wu, Y.; Li, G. *Nature Photon.* **2009**, *3*, 649.

[61] Liang, Y.; Xu, Z.; Xia, J.; Tsai, S.-T.; Wu, Y.; Li, G.; Ray, C.; Yu, L. *Adv. Mater.* **2010**, *22*, E135.

[62] He, Z.; Zhong, C.; Huang, X.; Wong, W.-Y.; Wu, H.; Chen, L.; Su, S.; Cao, Y. *Adv. Mater.* **2011**, *23*, 4636.

[63] Thompson, B.; Fréchet, J. *Angew. Chem. Int. Edit.* **2008**, *47*, 58.

[64] Dennler, G.; Scharber, M. C.; Brabec, C. J. *Adv. Mater.* **2009**, *21*, 1323.

[65] Cheng, Y.-J.; Yang, S.-H.; Hsu, C.-S. *Chem. Rev.* **2009**, *109*, 5868.

[66] Kanai, Y.; Grossman, J. C. *Nano Lett.* **2007**, *7*, 1967.

[67] He, Y.; Chen, H.-Y.; Hou, J.; Li, Y. *J. Am. Chem. Soc.* **2010**, *132*, 1377.

[68] Zhao, G.; He, Y.; Li, Y. *Adv. Mater.* **2010**, *22*, 4355.

[69] Dittmer, J. J.; Marseglia, E. A.; Friend, R. H. *Adv. Mater.* **2000**, *12*, 1270.

[70] Geng, J.; Zeng, T. *J. Am. Chem. Soc.* **2006**, *128*, 16827.

[71] Kymakis, E.; Koudoumas, E.; Franghiadakis, I.; Amaratunga, G. A. J. *J. Phys. D: Appl. Phys.* **2006**, *39*, 1058.

[72] Palacios-Lidón, E.; Perez-García, B.; Abellán, J.; Miguel, C.; Urbina, A.; Colchero, J. *Adv. Funct. Mater.* **2006**, *16*, 1975.

[73] Kanai, Y.; Grossman, J. C. *Nano Lett.* **2008**, *8*, 908.

[74] Wan, X.; Long, G.; Huang, L.; Chen, Y. *Adv. Mater.* **2011**, *23*, 5342.

[75] Bonaccorso, F.; Sun, Z.; Hasan, T.; Ferrari, A. C. *Nature Photon.* **2010**, *4*, 611.

[76] Bao, Q.; Loh, K. P. *ACS Nano* **2012**,

[77] Liu, Q.; Liu, Z.; Zhang, X.; Zhang, N.; Yang, L.; Yin, S.; Chen, Y. *Appl. Phys. Lett.* **2008**, *92*, 223303.

[78] Liu, Z.; Liu, Q.; Huang, Y.; Ma, Y.; Yin, S.; Zhang, X.; Sun, W.; Chen, Y. *Adv. Mater.* **2008**, *20*, 3924.

[79] Liu, Q.; Liu, Z.; Zhang, X.; Yang, L.; Zhang, N.; Pan, G.; Yin, S.; Chen, Y.; Wei, J. *Adv. Funct. Mater.* **2009**, *19*, 894.

[80] Wang, J.; Wang, Y.; He, D.; Liu, Z.; Wu, H.; Wang, H.; Zhao, Y.; Zhang, H.; Yang, B. *Synth. Met.* **2010**, *160*, 2494.

[81] Li, Y.; Hu, Y.; Zhao, Y.; Shi, G.; Deng, L.; Hou, Y.; Qu, L. *Adv. Mater.* **2011**, *23*, 776.

[82] Hohenberg, P.; Kohn, W. *Phys. Rev.* **1964**, *136*, B864.

[83] Kohn, W.; Sham, L. J. *Phys. Rev.* **1965**, *140*, A1133.

[84] Ceperley, D. M.; Alder, B. J. *Phys. Rev. Lett.* **1980**, *45*, 566.

[85] Perdew, J. P.; Zunger, A. *Phys. Rev. B* **1981**, *23*, 5048.

[86] Perdew, J. P.; Burke, K.; Ernzerhof, M. *Phys. Rev. Lett.* **1996**, *77*, 3865.

[87] Hamann, D. R. *Phys. Rev. B* **1989**, *40*, 2980.

[88] Troullier, N.; Martins, J. L. *Phys. Rev. B* **1991**, *43*, 1993.

[89] Vanderbilt, D. *Phys. Rev. B* **1990**, *41*, 7892.

[90] Koopmans, T. *Physica* **1934**, *1*, 104.

[91] Almbladh, C.-O.; von Barth, U. *Phys. Rev. B* **1985**, *31*, 3231.

[92] Godby, R.; García-González, P. In *A Primer in Density Functional Theory*; Fiolhais, C., Nogueira, F., Marques, M., Eds.; Lecture Notes in Physics; Springer Berlin / Heidelberg, 2003; Vol. 620; p 185.

[93] Aryasetiawan, F.; Gunnarsson, O. *Rep. Prog. Phys.* **1998**, *61*, 237.

[94] Becke, A. D. *J. Chem. Phys.* **1993**, *98*, 1372.

[95] Becke, A. D. *J. Chem. Phys.* **1996**, *104*, 1040.

[96] Broyden, C. G. *Math. Comput.* **1965**, *19*, 577.

[97] Bonnans, J. F.; Gilbert, J. C.; Lemaréchal, C.; Sagastizábal, C. A. *Numerical Optimization: Theoretical and Practical Aspects*, 2nd ed.; Springer: Berlin, 2006.

[98] Fuchs, M.; Scheffler, M. *Comput. Phys. Comm.* **1999**, *119*, 119.

[99] Kleinman, L.; Bylander, D. M. *Phys. Rev. Lett.* **1982**, *48*, 1425.

[100] Van de Walle, C. G.; Martin, R. M. *Phys. Rev. B* **1987**, *35*, 8154.

[101] Shaltaf, R.; Rignanese, G.-M.; Gonze, X.; Giustino, F.; Pasquarello, A. *Phys. Rev. Lett.* **2008**, *100*, 186401.

[102] Alkauskas, A.; Broqvist, P.; Devynck, F.; Pasquarello, A. *Phys. Rev. Lett.* **2008**, *101*, 106802.

[103] Bengtsson, L. *Phys. Rev. B* **1999**, *59*, 12301.

[104] Tersoff, J. *Phys. Rev. B* **1984**, *30*, 4874.

[105] Heine, V. *Phys. Rev.* **1965**, *138*, A1689.

[106] Tersoff, J. *Phys. Rev. Lett.* **1984**, *52*, 465.

[107] Goldstein, J.; Newbury, D. E.; Joy, D. C.; Lyman, C. E.; Echlin, P.; Lifshin, E.; Sawyer, L.; Michael, J. *Scanning Electron Microscopy and X-ray Microanalysis*, 3rd ed.; Kluwer Academic/Plenum Publishers: New York, 2003.

[108] Williams, D. B.; Carter, C. B. *Transmission Electron Microscopy: A Textbook for Materials Science*; Plenum Press: New York [u.a.], 2009.

[109] Gilliland, G. *Mater. Sci.Eng. R-Rep.* **1997**, *18*, 99.

[110] Meyer, B.; Marx, D. *Phys. Rev. B* **2003**, *67*, 035403.

[111] Goano, M.; Bertazzi, F.; Penna, M.; Bellotti, E. *J. Appl. Phys.* **2007**, *102*, 083709.

[112] Dag, S.; Wang, L. *Nano Lett.* **2008**, *8*, 4185.

[113] Cooke, D. J.; Marmier, A.; Parker, S. C. *J. Phys. Chem. B* **2006**, *110*, 7985.

[114] Mang, A.; Reimann, K.; Ruebenacke, S. *Solid State Comm.* **1995**, *94*, 251.

[115] Shih, B.-C.; Xue, Y.; Zhang, P.; Cohen, M. L.; Louie, S. G. *Phys. Rev. Lett.* **2010**, *105*, 146401.

[116] Stankovski, M.; Antonius, G.; Waroquiers, D.; Miglio, A.; Dixit, H.; Sankaran, K.; Giantomassi, M.; Gonze, X.; Côté, M.; Rignanese, G.-M. *Phys. Rev. B* **2011**, *84*, 241201.

[117] Woell, C. *Prog. Surf. Sci.* **2007**, *82*, 55.

[118] Duke, C. B.; Meyer, R. J.; Paton, A.; Mark, P. *Phys. Rev. B* **1978**, *18*, 4225.

[119] Hoang, T. B.; Moses, A. F.; Zhou, H. L.; Dheeraj, D. L.; Fimland, B. O.; Weman, H. *Appl. Phys. Lett.* **2009**, *94*, 133105.

[120] McMahon, M. I.; Nelmes, R. J. *Phys. Rev. Lett. 95*, 215505.

[121] Kusch, P.; Breuer, S.; Ramsteiner, M.; Geelhaar, L.; Riechert, H.; Reich, S. *Phys. Rev. B* **2012**, *86*, 075317.

[122] Zanolli, Z.; Fuchs, F.; Furthmller, J.; von Barth, U.; Bechstedt, F. *Phys. Rev. B* **2007**, *75*, 245121.

[123] Barton, J. J.; III, W. A. G.; McGill, T. C. *J. Vac. Sci. Technol.* **1979**, *16*, 1178.

[124] Stroscio, J. A.; Feenstra, R. M.; Fein, A. P. *Phys. Rev. B* **1987**, *36*, 7718.

[125] Geim, A. K.; Novoselov, K. S. *Nature Mater.* **2007**, *6*, 183.

[126] Geim, A. K. *Science* **2009**, *324*, 1530.

[127] Zhao, Y. X.; Spain, I. L. *Phys. Rev. B* **1989**, *40*, 993.

[128] Maillard, A.; Rochefort, A. *Phys. Rev. B* **2009**, *79*, 115207.

[129] Northrup, J. *Phys. Rev. B* **2007**, *76*, 245202.

[130] Prosa, T. J.; Winokur, M. J.; Moulton, J.; Smith, P.; Heeger, A. J. *Macromolecules* **1992**, *25*, 4364.

[131] Prosa, T. J.; Winokur, M. J.; McCullough, R. D. *Macromolecules* **1996**, *29*, 3654.

[132] Brinkmann, M.; Rannou, P. *Adv. Funct. Mater.* **2007**, *17*, 101.

[133] Brinkmann, M.; Wittmann, J. *Adv. Mater.* **2006**, *18*, 860.

[134] Tashiro, K.; Kobayashi, M.; Kawai, T.; Yoshino, K. *Polymer* **1997**, *38*, 2867.

[135] McCullough, R. D.; Tristram-Nagle, S.; Williams, S. P.; Lowe, R. D.; Jayaraman, M. *J. Am. Chem. Soc.* **1993**, *115*, 4910.

[136] Mena-Osteritz, E.; Meyer, A.; Langeveld-Voss, B. M. W.; Janssen, R. A. J.; Meijer, E. W.; Bäuerle, P. *Angew. Chem. Int. Edit.* **2000**, *39*, 2679.

[137] El-Azhary, A. A.; Suter, H. U. *J. Phys. Chem.* **1996**, *100*, 15056.

[138] Brocks, G. *J. Phys. Chem.* **1996**, *100*, 17327.

[139] Noori, K.; Giustino, F. *Advanced Functional Materials* **2012**, *22*, 5089.

[140] Yu, H.; Zhang, Z.; Han, M.; Hao, X.; Zhu, F. *J. Am. Chem. Soc* **2005**, *127*, 2378.

[141] Giustino, F.; Pasquarello, A. *Surf. Sci.* **2005**, *586*, 183.

[142] Deibel, C.; Mack, D.; Gorenflot, J.; Schöll, A.; Krause, S.; Reinert, F.; Rauh, D.; Dyakonov, V. *Phys. Rev. B* **2010**, *81*, 085202.

[143] Gwinner, M. C.; Vaynzof, Y.; Banger, K. K.; Ho, P. K. H.; Friend, R. H.; Sirringhaus, H. *Adv. Funct. Mater.* **2010**, *20*, 3457.

[144] Onoda, M.; Tada, K.; Zakhidov, A. A.; Yoshino, K. *Thin Solid Films* **1998**, *331*, 76.

[145] Snaith, H. J. *Adv. Funct. Mater.* **2010**, *20*, 13.

[146] Ishii, H.; Sugiyama, K.; Ito, E.; Seki, K. *Adv. Mater.* **1999**, *11*, 605.

[147] Crispin, X.; Geskin, V.; Crispin, A.; Cornil, J.; Lazzaroni, R.; Salaneck, W. R.; Brédas, J. *J. Am. Chem. Soc.* **2002**, *124*, 8131.

[148] Kahn, A.; Koch, N.; Gao, W. *J. Polym. Sci., Part B: Polym. Phys.* **2003**, *41*, 2529.

[149] Maurano, A.; Hamilton, R.; Shuttle, C. G.; Ballantyne, A. M.; Nelson, J.; O'Regan, B.; Zhang, W.; McCulloch, I.; Azimi, H.; Morana, M.; Brabec, C. J.; Durrant, J. R. *Adv. Mater.* **2010**, *22*, 4987.

[150] Nagata, T.; Oh, S.; Yamashita, Y.; Yoshikawa, H.; Ikeno, N.; Kobayashi, K.; Chikyow, T.; Wakayama, Y. *Appl. Phys. Lett.* **2013**, *102*, 043302.

[151] Allen, M. W.; Durbin, S. M. *Appl. Phys. Lett.* **2008**, *92*, 122110.

[152] Xiang, H. J.; Yang, J.; Hou, J. G.; Zhu, Q. *Appl. Phys. Lett.* **2006**, *89*, 223111.

[153] Blakemore, J. S. *J. Appl. Phys.* **1982**, *53*, R123.

[154] Chua, L.-L.; Zaumseil, J.; Chang, J.-F.; Ou, E. C.-W.; Ho, P. K.-H.; Sirringhaus, H.; Friend, R. H. *Nature* **2005**, *434*, 194.

[155] Greenham, N. C.; Peng, X. G.; Alivisatos, A. P. *Phys. Rev. B* **1996**, *54*, 17628.

[156] Wang, P.; Abrusci, A.; Wong, H. M. P.; Svensson, M.; Andersson, M. R.; Greenham, N. C. *Nano Lett.* **2006**, *6*, 1789.

[157] Stranks, S. D.; Weisspfennig, C.; Parkinson, P.; Johnston, M. B.; Herz, L. M.; Nicholas, R. J. *Nano Lett.* **2011**, *11*, 66.

[158] Wang, X.; Zhi, L.; Müllen, K. *Nano Lett.* **2008**, *8*, 323.

[159] Nguyen, L.; Hoppe, H.; Erb, T.; Günes, S.; Gobsch, G.; Sariciftci, N. *Adv. Funct. Mater.* **2007**, *17*, 1071.

[160] Hibino, H.; Kageshima, H.; Kotsugi, M.; Maeda, F.; Guo, F.-Z.; Watanabe, Y. *Phys. Rev. B* **2009**, *79*, 125437.

[161] Wilder, J. W. G.; Venema, L. C.; Rinzler, A. G.; Smalley, R. E.; Dekker, C. *Nature* **1998**, *391*, 59.

[162] Puschnig, P.; Amiri, P.; Draxl, C. *Phys. Rev. B* **2012**, *86*.

[163] Stankovich, S.; Piner, R. D.; Nguyen, S. T.; Ruoff, R. S. *Carbon* **2006**, *44*, 3342.

[164] Tsoi, W. C.; Spencer, S. J.; Yang, L.; Ballantyne, A. M.; Nicholson, P. G.; Turnbull, A.; Shard, A. G.; Murphy, C. E.; Bradley, D. D. C.; Nelson, J.; Kim, J.-S. *Macromolecules* **2011**, *44*, 2944.

[165] Giannozzi, P. et al. *J. Phys.:Condens. Matter* **2009**, *21*, 395502, http://www.quantum-espresso.org.

[166] Perdew, J. P.; Ernzerhof, M.; Burke, K. *J. Chem. Phys.* **1996**, *105*, 9982.

[167] Hanfland, M.; Beister, H.; Syassen, K. *Phys. Rev. B* **1989**, *39*, 12598.

Acknowledgements

I would like to extend my sincere thanks to my supervisor, Feliciano Giustino. His patience, guidance, and wisdom have helped me immeasurably over the past four years and I am incredibly lucky to have had such an attentive and thoughtful mentor. The successful completion of this thesis is in no small part due to him.

To my current and erstwhile officemates I would also like to show my appreciation. Chris, Harry, Henry, Tim, and Hannes: you have made coming into the office something to look forward to instead of something to dread. Your humour and intelligence have made our office a constant source of entertainment and learning...not always in equal parts. I will always remember our games of "Only Connect", Guardian crosswords, pasta lunches and Nespresso coffees (What Else?). I am also indebted to everyone in the MML for their kindness, laughter, support, and advice. I have been extremely fortunate to have had the opportunity to work with all of you.

My four years in Oxford have provided me with many amazing experiences and memories. I have met a number of truly remarkable people at St Anne's College, all of whom have enriched my time in Oxford to no end. A special mention goes to 3 Juxon and its official and unofficial members. My thanks

go out to all of my friends in Oxford, London and elsewhere. You have made living in the UK a pleasure.

Finally, I must extend my deepest appreciation to my family. There is no doubt that I would not be where I am today without their unending and unconditional support and love. Annie, Hamid and Arshia, you have been the best family I could have hoped for and you have made me everything that I am. Thank you!